



HAL
open science

2D and 3D ultrafast nanoscale imaging by coherent diffraction

Fan Wang

► **To cite this version:**

Fan Wang. 2D and 3D ultrafast nanoscale imaging by coherent diffraction. Optics [physics.optics]. Université Paris Sud - Paris XI, 2014. English. NNT : 2014PA112226 . tel-01164577

HAL Id: tel-01164577

<https://theses.hal.science/tel-01164577>

Submitted on 17 Jun 2015

HAL is a multi-disciplinary open access archive for the deposit and dissemination of scientific research documents, whether they are published or not. The documents may come from teaching and research institutions in France or abroad, or from public or private research centers.

L'archive ouverte pluridisciplinaire **HAL**, est destinée au dépôt et à la diffusion de documents scientifiques de niveau recherche, publiés ou non, émanant des établissements d'enseignement et de recherche français ou étrangers, des laboratoires publics ou privés.

UNIVERSITÉ PARIS-SUD

ÉCOLE DOCTORALE 288 :

ONDES ET MATIÈRE

Laboratoire : LIDYL, IRAMIS, DSM, Commissariat à l'Énergie
Atomique, Saclay, France

THÈSE DE DOCTORAT

PHYSIQUE

par

Fan WANG

Imagerie nanométrique 2D et 3D
ultrarapide par diffraction cohérente

Date de soutenance : 25/09/2014

Composition du jury :

Rapporteurs :	M. Philippe ZEITOUN	LOA-ENSTA
	M. Milutin KOVACEV	Universität Hannover
Directeur de thèse :	M. Hamed MERDJI	CEA-Saclay
Examineurs :	M. Gilles MAYNARD	LPGP
	M. Eric CORMIER	Université Bordeaux 1
	M. Nelson DE OLIVEIRA	Synchrotron-soleil
	M. Guillaume DOVILLAIRE	Imagine Optics

Acknowledgement

Firstly, I'd like to express my gratitude to my Ph.D supervisor, Dr. Hamed MERDJI. Without his reception and help for my thesis work, I couldn't have chance to enter in fundamental research field and finish my work and thesis manuscripts at last. During the period of thesis, he offered me the greatest advice both on the research direction and moral support. He played well as a guide for my research carrier. At the same time, he helped me also to collaborate and communicate with other worldwide famous research group for deeper scientific comprehension and progress in the corresponding Ph.D subject research domain.

Then, I am also thankful to my dear colleagues in the same team: Willem Boutu, David Gauthier, Xunyou Ge, Aura Ines Gonzalez and so on, for their fruitful discussion and help on the scientific and technical comprehension in both physical theory and experience. Especially, they give me much support about the research idea, installing the experience set-up and establishing research plan and method. In this context, some experimental results during my thesis are issue from our collective diligent work. And I have learned and acquired a lot from them in both the precious scientific knowledge and attitude.

Thirdly, I never forget my family, my dear parents, and my little brother. They give me warm and love in my heart, which assurances my peaceful and concentrated long time research work. They are my heart bay, my source of fighting. Another future member, my boyfriend, who is a mathematic Ph.D candidate, gives me also important support that helps me go across the life darkness and difficulty period in writing thesis.

Last, I give also my thanks to Bertrand Carré, our group leader. He permitted me to develop research in the Attophysique group. And sometimes he supported our experience work very late at night for the laser beam. He occupied as a permanent staff on turning off the laser beam. I shall also thank my colleagues in the group but with research in other topics: Pascal Salière, Thierry Ruchon, Nan Lin et Antoine Camper, Sebastian, Elisabeth English and so on for their generous introduction and share about knowledge food. We have participated in so many seminars, summer schools for further understanding in the research for atto- or femto- laser development.

Anyway, there are still so many staffs when I met during my thesis work: our technical support colleague, Marc Billon and other staff from laser beam lime operation team: Olivier Gobert, Benoît Mahieu and so on. I honor them with a thankful heart.

Contents

Introduction	4
Motivation and outline.....	7
Chapter I - Principle of lens-less imaging	11
I.1 Few basics in lens-less imaging techniques	11
I.2 Image formation in lens-less imaging	14
I.3 Reconstruction: Phase retrieval algorithms	21
I.4 Reconstruction: FTH and HERALDO	24
I.5 Beam requirements for lens-less imaging	27
I.6 Conclusion	28
Chapter II - High harmonic generation	29
II.1 Introduction	29
II.2 Experimental set-up.....	31
II.3 HHG optimization and beamline standardization	34
II.4 Laser Modal Filtering for HHG optimization	44
II.5 Conclusion	48
Chapter III -Coherent Diffractive Imaging and Holographic imaging	51
III.1 Introduction.....	51
III.2 Sample preparation.....	51
III.3 Detection of the diffraction pattern	53
III.4 Implication of the spatial coherence in the CDI reconstructions.....	54
III.5 Experimental results of CDI	57
III.6 Experimental results of Fourier Transform Holography.....	60
III.7 Experimental results of holography with extended reference.....	64
III.8 Signal-to-noise ratio (SNR) analysis	66
III.9 HERALDO reconstruction and noise	69
III.10 CDI reconstructions of HERALDO objects.....	88
III.11 Conclusion.....	91
Chapter IV - Towards single shot 3D Coherent Imaging	93
IV.1 Introduction.....	93
IV.2 Basics in three dimensional coherent imaging	94
IV.3 CDI reconstruction algorithm in 2D and 3D	98
IV.4 The ankylography : a 3D single view imaging technique.....	101
IV.5 First experimental data at the CEA HHG beamline	106
IV.6 Conclusion	119
Chapter V -General Conclusion and Perspectives	120
References	129
Articles List	134

Introduction

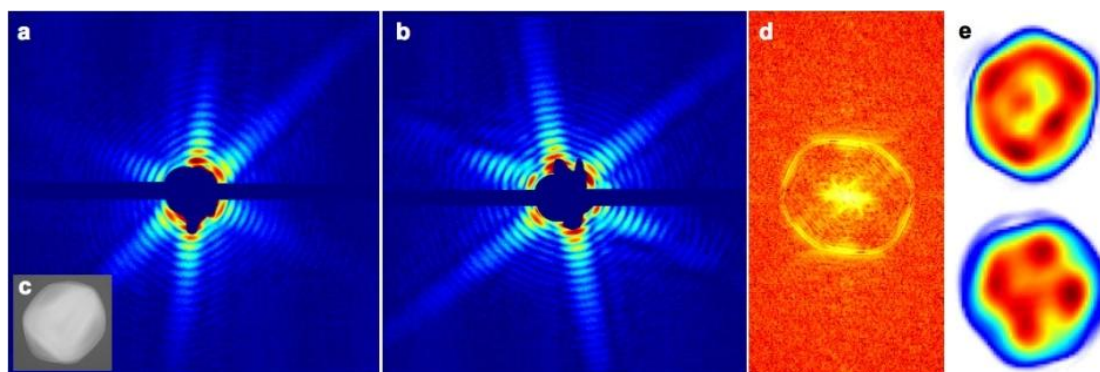
How is an image formed? Do we really need lenses to generate an image? Obviously, this is not necessary. The philosopher Mo Jing in ancient China, during the 5th century BC, mentioned the effect of an inverted image forming through a pinhole. Nowadays, it is still a well-applied technique but limited by the shape and size of the pinhole. What technique would overcome any manufacturing limitation? Modern optics brought the answer with diffraction and Fourier optics. Since the advances made in the last decades with the introduction of lensless imaging techniques with X-rays and particles, imaging science has witnessed extraordinary advancements. We are concerned about elucidating structural changes over broad time scales (attoseconds to many seconds) and length scales (nanoscale to macroscale). This is of interest not only in biology, but also in physics, medicine and in order to create the revolutionary materials required for future communication and energy technologies. Scientific and industrial innovations depend on our capacity to design, observe, control matter at these various space and time scales. Improved or entirely new characterization tools increase our understanding of the “real” world, from complex organized systems to a single particle. While various forms of microscopy (TEM, SEM, AFM, STM, etc.) can furnish detailed information about morphology, size, and on occasion the composition of nanoparticles, none are capable of providing real-time, on-line information.

To bridge the gap between conventional diffraction and microscopy, and to image single non-periodic objects with atomic/nanometric spatial resolution, *coherent diffractive imaging (CDI)* has demonstrated very high potential. Since its demonstration [1-2], many researchers have taken a large step in this direction using synchrotron radiation, free electron laser or high harmonic generation [3-8]. The idea of CDI came from the successful crystallography diffraction methods. David Sayre first raised this question that whether a similar diffraction method could be applied to non-periodic objects in 1952 [9]. J.R. Fienup proposed a phase-retrieval algorithm to solve the phase problem in 1978 [10]. His algorithm is a modified version of Gerchberg-Saxton algorithm that is originally inspired from ideas used in electron microscopy [11]. For more details of the historical development of the phase-retrieval algorithm, please refer to the review of Henry Chapman and Keith Nugent [12].

Exploiting coherence in diffraction, scientists have now in hand a revolutionary imaging system, an ultimate microscope that can see inside our “ultrasmall” world

with incredible clarity. *No lens is needed*, it is only necessary to record the intensity of the diffraction pattern that emerges after its interaction with the object on a high-resolution high dynamic range pixelated detector. The diffraction patterns in no way resembles the object itself, but a computer can convert this digitized diffraction pattern using a calculation known as a "phase-retrieval" to extract the information. In this way, it is possible to make much better images than with conventional lens-based systems. The spatial resolution can be pushed down to the theoretical diffraction-limit given by the source wavelength so that potentially atomic vision could be available using coherent hard X-rays.

In-situ images of individual sub-micrometer particles and molecules at atomic/nanometre resolution in their native environment can be applied to resolve both static and dynamic structures. The dream experiment would consist in producing the best-ever pictures of individual atoms, molecules or cells in any structure even if it is not crystalline. A first example is given by images of viruses recently obtained at the LCLS free electron laser (see fig. below) [13]. This is of strong interest as a big gap exists in the knowledge of viruses structures in the range from about 30nm to 500nm (see figure below). In fact, these length scales remain uncharted territory for many other biological systems.



First results from the LCLS where single mimivirus particles were injected into the FEL beam. Recorded diffraction patterns (left) and image reconstruction of the virus (right).

Third generation synchrotrons has also given extraordinary pictures, like the 3D structural image of a single nanocrystal [14] or a bone [15], ultrafast coherent X-ray flashes provided by free electron lasers (FEL) and high laser harmonic (HHG) sources allow dynamical studies. We are dealing with X-ray flashes few femtoseconds (10^{-15} s) down to 100 attoseconds (10^{-18} s) short. Spectacular advances in the attainment of ultrafast imaging represent a real breakthrough in science in particular when the dynamics come into play. Have you ever imagined a camera capable of following in space and time an electronic cloud moving as fast as an electromagnetic wave or watching the dance of atoms inside a stressed nanocrystal? Atomic/nanometric spatial changes on ultrafast time scales will add new dimensions

to understanding primary biological or chemical reactions. Ultrafast lensless imaging can be applied to follow in real time nanoscale processes; nano-crystal stress, nano-magnetism or nanoscale phase transitions are few examples. In magnetism, this will offer new tools to create and optimize next generation ultrafast storage and calculator devices.

Those illustrations are non-exhaustive and new horizons are opened. *Indeed, new concepts in imaging have always fascinated mankind while creating significant economic impact.* We can cite for example the extraordinary adventure of Stanford researchers transforming light field and Fourier technology from a scientific theory into a reality for everyone (<https://www.lytro.com/>). Lensless imaging has a similar potential. Why not a digital lensless camera?

CDI is a powerful tool in many scientific areas ranging from biology to solid-state physics. The key words for CDI are “coherence” and “diffraction”. Indeed, the technique uses the measurement of a far field *diffraction* pattern to retrieve the spatial *amplitude and phase* of a real space object. The large-scale facilities – synchrotron light sources and FELs provide a large amount of photons promising a good signal-to-noise ratio in CDI. The high coherence of FELs and synchrotrons (using a pinhole in this case) ensures that the important phase information can be well “written” in the detected diffraction pattern. Moreover, the femtosecond pulse duration of FEL sources promises a bright future for ultrafast dynamic imaging at a nanometer or sub-nanometer scale.



FLASH in Hamburg (VUV FEL) LCLS in Stanford (X-ray FEL)

However, these large-scale facilities cost expensive resources and have limited access beam time. These constraints limit the wide spread of ultrafast coherent diffractive imaging. The applications are then restricted. This limits the impact of this research for example in the optimization of ultrafast nanoscale devices in communication, medicine or even in more industrial environments. Therefore, an inexpensive source

would provide a very interesting alternative: high-order harmonic generation (HHG) sources can provide intense highly coherent soft X-ray photons with ultrafast pulse duration. The relatively small size and low cost of such light source makes the HHG source an ideal alternative to synchrotrons and FELs. Up to recently, the limited brightness of HHG source was a key limitation for a table-top application of CDI. However in 2007, Richard Sandberg and colleagues have succeeded in demonstrating CDI using a kHz table-top laser driven HHG source with a spatial resolution of 214nm [7]. The brightness of the harmonic beam was still limited, and the exposure time of this experiment was on the scale of an hour (up to 10^6 laser shots!) that is far from reaching single shot ultrafast nanoscale imaging, required in many dynamical studies. In 2009, our research group at CEA (Commissariat à l’Energie Atomique et aux Energies alternatives) has demonstrated the first single-shot CDI using a table-top femtosecond soft X-ray laser harmonic source [8]. An isolated test nano-object was reconstructed with 119nm spatial resolution in a single 20fs-long shot. A spatial resolution of 62 nm was obtained from multiple laser shots (40 shots). In this context, I have joined the AttoPhysique group of CEA as a PhD student of Dr. Hamed Merdji in 2010.

Motivation and outline

The principle objective of this work is to perform extended developments and applications of ultrafast coherent imaging techniques using table-top harmonic source. I present all the efforts, either on the source, and the imaging techniques to build a reliable and powerful ultrafast microscope with nanometer spatial resolution and femtosecond temporal resolution. I present then a characterization of magnetic nano-domains at a sub-100nmscale in a single femtosecond shot. This illustrates the potential of our table-top harmonic beamline for various scientific research areas such as material science, biology and chemistry.

This work is presented in five chapters.

Chapter 1 is dedicated to the description of the theoretical background of the lens-less imaging (also called coherent imaging). It starts with a presentation of the principle of the lens-less imaging. The first part is the mathematical description of diffraction and Fourier Transform that are the basics of diffraction pattern formation of the coherent imaging. The second part is the description of basic phase-retrieval algorithms and holographic techniques that are used in this work. The third part is a discussion of the beam requirements for lens-less imaging, followed by a brief description of the HHG process used as light source in this thesis work. This chapter

should give a clear description of CDI and help to understand the ideas and methods used in the following chapters.

The main work and experimental results are presented respectively in Chapter 2, 3 and 4.

Chapter 2 starts with the description of the experimental setup – the table-top high flux harmonic beamline at CEA Saclay. The first step of this thesis work has been a complete optimization of the harmonic beam line from the very beginning of the infrared pump laser to the focusing optics at the end of the imaging setup. The optimization processes and results are presented in *Paper I* and *Paper II* attached to this chapter. The first one discusses the optimization of infrared pump laser using a modal filtering hollow core fiber, which leads to improvement of the HHG efficiency and stability. After the beam line optimization, spectrum and far field studies of HHG in two different gas mediums (argon and neon) are presented. The first one shows the optimization of the HHG and the diffraction stages. The objective has been to increase the photon flux, the coherence and the wave front quality of the harmonic beam. Statistic studies using a Hartmann wave front sensor and Young double slits to characterize the wave front and the coherence show the improvement of the harmonic beam and the influence of these beam properties in the image reconstruction quality. This chapter concludes with the summary of the optimized high flux harmonic beamline and a short discussion of a comparison between large-scale facilities sources (synchrotron and FELs) and table-top harmonic sources for coherent imaging.

Chapter 3 presents the second step of the thesis work: the validation of different coherent imaging techniques at the table-top harmonic beam line. It starts with experimental results of classic CDI and discussion of the spatial coherence implementation in the reconstructions. The second part is the experimental results of Fourier Transform Holography (FTH), which is a complementary imaging technique to CDI. The limitation in spatial resolution in FTH inspired several new imaging techniques such as Holography with Extended Reference by Autocorrelation Linear Differential Operation (HERALDO). HERALDO offers an alternative way for ultrafast nanometric imaging, which is easy to implement on all kinds of beam line performing coherent imaging. The step-by-step analysis of the HERALDO reconstruction process leads to a discussion of the influence of reference design and the signal-to-noise ratio issue, which is reported in *Paper III*. Indeed, the signal-to-noise ratio gives restrictions in both CDI and holographic techniques for our experiments. A comparison between CDI, FTH and HERALDO techniques concludes this chapter.

Chapter 4 is the last achievement of this thesis work: the extension of 2D coherent diffractive to 3D. I present the theoretical study of three-dimensional coherent diffractive imaging. Generally, to accomplish a full 3D display, multiple views of objects are required. It is worthwhile to discuss the relationship between two dimensional and three dimensional diffraction imaging. Recently, a new 3D imaging technique, named ankylography, proposed to exploit high angle, single view, 2D diffraction to recover 3D amplitude and phase information. Before investigating the 3D image reconstruction process of an object from its diffraction pattern, some basic points in the 2D case are reviewed. We recall the numerical algorithm image reconstruction from a coherent diffraction pattern. In addition, we explain the numerical developments that play an important role as a bridge from 2D to 3D perception. Then we present our first experimental data and image reconstructions. Those data allow identifying restrictions in the 3D ankylographic image reconstruction.

Chapter 5 draws the perspectives and gives the general conclusion of this thesis. I summarize the main conclusions of the harmonic beamline investigations, the 2D coherent imaging techniques (CDI, FTH, HERALDO) and the first 3D imaging results. Furthermore, we open a new perspective towards 3D coherent imaging using a technique based on the stereo vision. In this configuration, 2D stereo images can be either reconstructed using coherent diffractive or holographic techniques.

Chapter I - Principle of lens-less imaging

I.1 Few basics in lens-less imaging techniques

In conventional imaging systems, such as optical microscope and photo camera, a simple lens or a group of convex and/or concave lenses are used to form the image of the target object that is illuminated by a proper light source (Fig. 1.1). In complicated imaging systems, the lens system can also contain other optical elements, such as mirrors, windows, etc. The image quality is generally limited by the lens system: the ensemble of each optic's aberration determines the possible alterations of the object image. This imposes strong constraints on manufacturing of optical elements and design of lens system. In X-ray microscopy, the highest spatial resolution to date has been obtained using zone plate Fresnel optics. The constraints on optical elements become more critical. First, the resolution of such image-forming optics is limited by the smallest outer feature of the zone plate, which raises a real challenge on the optics manufacturing if one would like to reach nanometric resolution. Secondly and more fundamentally, the material of such optics has strong photon absorption, which limits its efficiency to typically less than 10% and often as low a percent [1]. The latter one is critical for high resolution imaging of certain specimens that are sensitive to radiation damage [2,3]. In this context, the lens-less imaging provides an alternative solution for high resolution imaging for various applications from biology to solid-state physics.

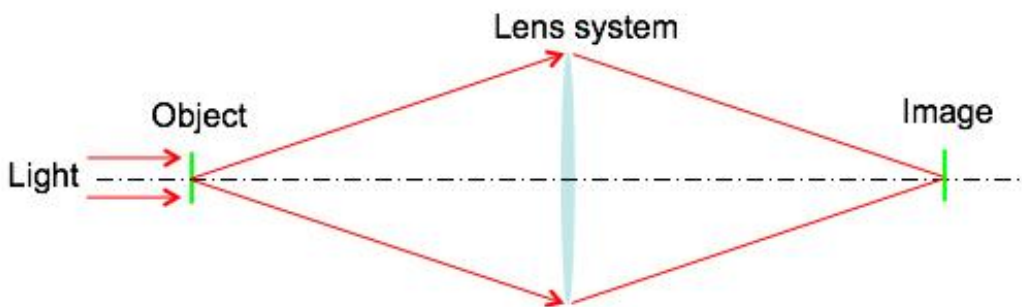


Fig. 1.1. Scheme of conventional imaging systems. Object image is formed by a lens system.

In lens-less imaging, no optics is required after the illumination of the object. Computation algorithms are used to retrieve the object's image instead of a lens imaging system. The isolated object is illuminated by a coherent wave, which ideally has to be monochromatic. The object diffracts and induces modifications in magnitude and/or in phase of the incident wave. The diffraction pattern is then measured in the far field by a pixel-array detector, which is usually a Charge-Coupled Device (CCD) camera (Fig. 1.2).

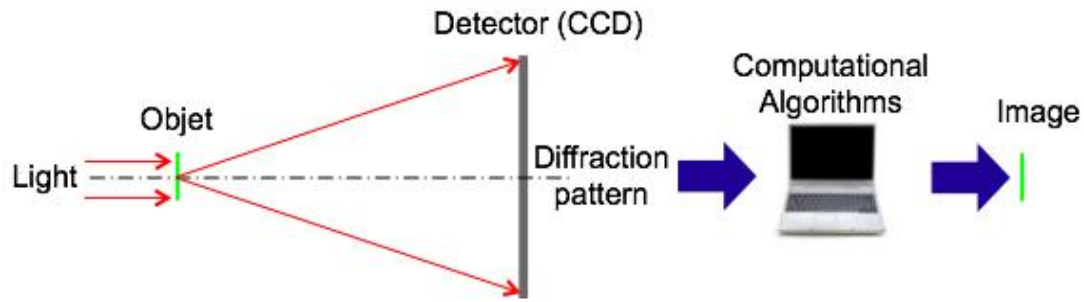


Fig 1.2. Scheme of a lens-less coherent imaging set-up. The computation algorithms replace the lens system conventionally used to image the object.

In the Fraunhofer diffraction regime, the diffraction pattern is proportional to the Fourier transform of the exit wave in the image plane. Theoretically, a simple inversion of the diffraction pattern should give the image of the object. But the pixel-array detector is only sensitive to the intensities of the electromagnetic wave field. Therefore, the phase information of the wave field is not directly measured by the detector. Infinity of possible solutions of the simple inversion can be obtained by applying possible phases to the measured diffraction pattern [4]. Here comes the famous “*phase problem*”, which is the main obstacle to extract object information from the measured diffraction pattern. Two main techniques have been proposed to overcome the “*phase problem*”: one uses Phase Retrieval Algorithms [6,7,8] and is called Coherent Diffractive Imaging (CDI); the other is Fourier Transform Holography (FTH) [5].

In CDI, iterative algorithms converge to the spatial phase in the diffraction plane using constraints both in real and reciprocal space (the diffraction plane). A scheme of the CDI technique is shown in Fig. 1.3. In the reciprocal space, the diffraction pattern recorded by the detector is equal to the absolute squared value of the Fourier transform of the exit wave. In the real space, the object is contained in a finite dimension (called “*support*”). The autocorrelation defined as the Fourier transform of the measured diffraction pattern will give a first constraint to the support (other constraint can be found). The relation of Fourier transform links these two constraints between real and reciprocal spaces. In general, most phase retrieval algorithms use these two kinds of constraints to reconstruct the “*lost phase*” in the reciprocal space and the object image in the real space. During the detection of the diffraction patterns, the coherence of the incident wave plays an important role. It creates a characteristic “*speckle pattern*” in the diffraction plane. The “*speckle*” is the “*phase signature*” of the diffraction pattern that ensures the convergence of iterative algorithms. The phase retrieval algorithms reconstruct simultaneously the phase in

reciprocal space and the object image in real space. The solution is nearly unique for problems that have more than one dimension [9,10].

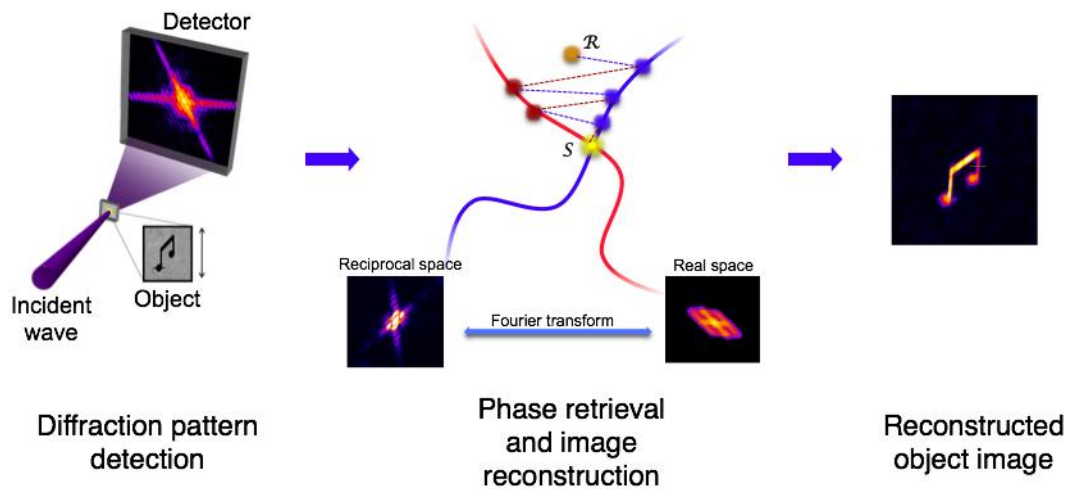


Fig. 1.3. The scheme of CDI can be separated into two steps: the first one is the detection of the object's diffraction pattern. The second step is to use phase retrieval algorithms to reconstruct the "lost phase" of the diffraction pattern and the object image.

Fourier Transform Holography (FTH) is another lens-less imaging technique, which has almost the same experiment setup as the CDI except that the sample geometry holds a holographic reference. The principle of FTH is similar to holography proposed by Dennis Gabor in 1948 [11]. The FTH is inspired by this idea of "full recording": the incident wave is simultaneously diffracted by the object and the reference. The detector located in the far field records the interference between these two diffracted waves, which is called "hologram". The spatial amplitude and phase of the object are encoded in this hologram and a simple Fourier transform is required to reconstruct the object image [12] (Fig. 1.4). The Fourier transform of the hologram is the autocorrelation of the sample (object + pinhole). The reconstructed object image is the correlation between the object and the pinhole.

In my thesis work, I have been focused on an extended reference holographic technique initially proposed by S.G. Podorov in 2007 [13], generalized by M. Guizar-Sicairos [14] and entitled "Holography with Extended Reference by Autocorrelation Linear Differential Operator (HERALDO)". In HERALDO, the pinhole reference is replaced by extended references, such as a slit (1 dimension), a square or a rectangle (2 dimensions), a triangle (2D), etc. (Fig. 1.4). The extended references should contain sharp features, such as the two extremities of a slit, the corners of a square, a rectangle or a triangle. When applying a differential operator to the registered hologram (the autocorrelation of the sample), the extended references turn into Dirac

delta functions (which correspond to the sharp features at the edges of the extended references). Note that the Fourier transform properties of delta function ensure a high-resolution reconstruction (Fig. 1.4). By this way, the resolution is no longer limited by the reference size, so one can increase the diffraction signal without affecting the resolution. Theoretically, the reconstruction resolution is limited by the quality of the manufactured references. In particular the sharpness of the edges is crucial.

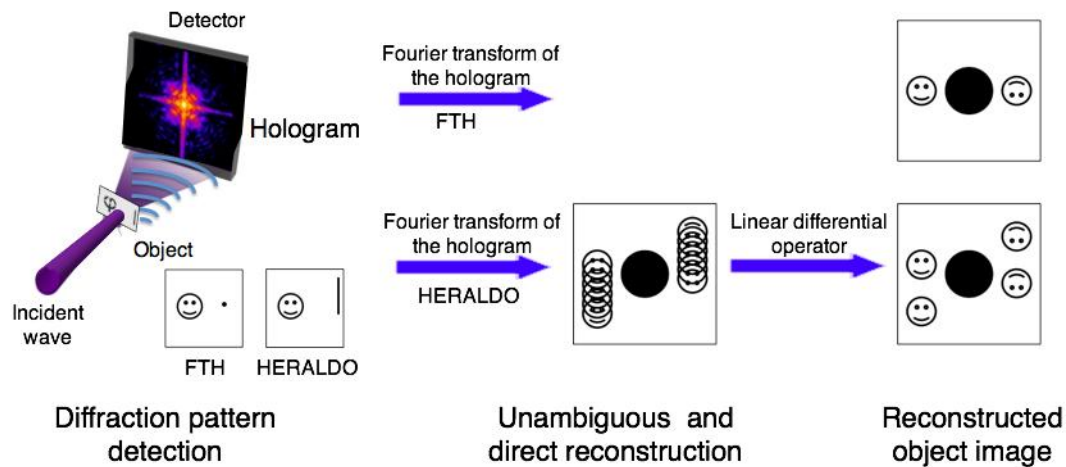


Fig. 1.4. Scheme of FTH and HERALDO: We have used the same experimental setup as in CDI except the sample geometry. In FTH, the sample consists in the object and a pinhole reference in the nearby at a distance that respects the holographic separation given by the size of the object. In HERALDO, the arrangement is similar but the reference is large while keeping the holographic separation. The reconstruction step is simple and direct: in FTH, the Fourier transform of the hologram gives the object image; in HERALDO, a linear differential operation is applied as a post process of the Fourier transform to finally get the object image reconstruction.

I.2 Image formation in lens-less imaging

The image formation is the fundamental of lens-less imaging and all ideas of reconstruction techniques are based on it and inspired by its properties. As mentioned before, CDI, FTH and HERALDO have the same experimental setup. The image formation is thus the same for these techniques from the incident wave propagation to the Fraunhofer diffraction process, except that different sample preparation for CDI and FTH/HERALDO leads to different diffraction patterns. Since the wave propagation and Fraunhofer diffraction are well known, I present here the relevant equations, formulas and properties in the case of the lens-less imaging to give a clear description of theoretical background with non-exhaustive mathematics. One can refer to the books of J.W. Goodman and to the Born and

Wolf[12,13] for detailed mathematical and physical deduction of wave propagation and Fraunhofer diffraction in general case. More practically, one can also look at some excellent thesis work such as P. Thibault [14], M. Guizar-Sicairos[15] or D. Gauthier at Saclay [16] that have well-detailed mathematical presentations of the image formation in the case of lens-less imaging.

1.2a Image formation in lens-less imaging: Diffraction

We usually consider in lens-less imaging an isolated object illuminated by a plane wave (Fig. 1.5). The exit wave is the wave field transmitted by the object and detected in the far field (by a CCD camera in our case). The propagation of the exit wave behaves according to the Helmholtz wave equation:

$$\nabla^2 \psi + k^2 n^2 \psi = 0 \quad (\text{Eq. 1-1})$$

where $\mathbf{k} = \frac{\omega}{c}$ and $n^2 = \epsilon \mu$. ω is the frequency of the wave ψ ; ϵ and μ are respectively the electric permittivity and the magnetic permeability of the medium.

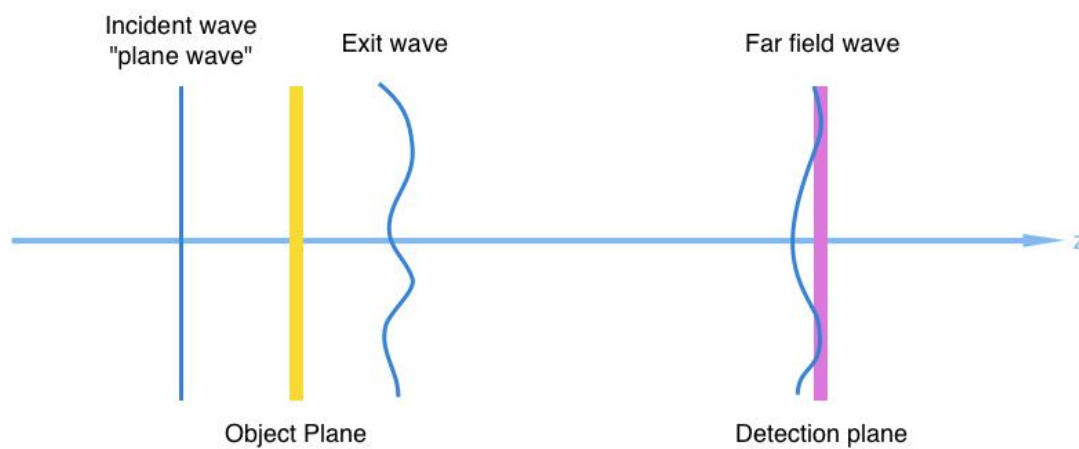


Fig. 1.5. The wave propagation in lens-less imaging.

Commonly in the X-ray community [17], the refractive index n is expressed by its purely refractive (real) and absorptive (imaginary) components, δ and β :

$$n = 1 + \Delta n = 1 - \delta - i\beta \quad (\text{Eq. 1-2})$$

Δn is non-zero only in a finite region of the space occupied by the object, and when $\Delta n = 0$, the wave ψ is the solution of the Eq. 1-1 in free-space propagation condition. The Eq. 1-1 has a simple form in the Fourier space:

$$(k^2 - q^2)\tilde{\psi}(q) = 0 \quad (\text{Eq. 1-3})$$

Obviously, $\tilde{\psi}(q) = 0$ unless $|q| = k$, which is called the “Ewald sphere” [18]. In our lens-less imaging experiments, the detection plane is a plane transverse to the wave propagation direction. Thus we can separate the free-space propagating wave field into transverse and parallel components, respectively $r_{\perp} = (x, y)$ and z . The general solution of Eq. 1-1 is then obtained in Fourier space as follow:

$$\tilde{\psi}(q_{\perp}, z) = \tilde{\psi}^{-}(q_{\perp})e^{-i\kappa z} + \tilde{\psi}^{+}(q_{\perp})e^{i\kappa z} \quad (\text{Eq. 1-4})$$

where $\kappa = \sqrt{k^2 - q_{\perp}^2}$ (Fig. 1.9) and $\tilde{\psi}^{\pm}(q_{\perp})$ are two independent functions representing forward (+) and backward (-) scattering. In our experiments, back-propagating terms can be neglected, therefore the solution is:

$$\psi(r_{\perp}, z) = \mathcal{F}^{-1}[\tilde{\psi}^{-}(q_{\perp})e^{i\kappa z}] \quad (\text{Eq. 1-5})$$

From Eq. 1-5, we can deduce the wave function in far field diffraction (Fraunhofer diffraction) [19]:

$$\psi_{\text{farfield}}(r_{\perp}, z) \propto \int d^2q \tilde{\psi}(q) e^{ikz \left(\sqrt{1 - \left(\frac{q}{k}\right)^2} + \frac{q}{k} \frac{r_{\perp}}{z} \right)} \quad (\text{Eq. 1-6})$$

Since $z \rightarrow \infty$ (far field), the integrand will not disappear unless the phase term is stationary, which means:

$$\frac{r_{\perp}}{z} = \frac{q_{\perp}}{\sqrt{k^2 - q_{\perp}^2}} = \frac{q_{\perp}}{\kappa} \quad (\text{Eq. 1-7})$$

Therefore, we can get the measured intensity by the detector in the far field:

$$I = |\psi_{\text{farfield}}(r_{\perp})|^2 \propto \frac{1}{1 + \left(\frac{r_{\perp}}{z}\right)^2} \left| \tilde{\psi} \left(q_{\perp} = \kappa \frac{r_{\perp}}{z} \right) \right|^2 \quad (\text{Eq. 1-8})$$

In our experiments, Eq. 1-6 can be simplified in the case of small-angle scattering (Fig. 1.6), which is valid when:

$$\frac{q_{\perp}}{k} < 1 \Rightarrow \frac{r_{\perp}}{z} = \tan \theta < 1 \quad (\text{Eq. 1-9})$$

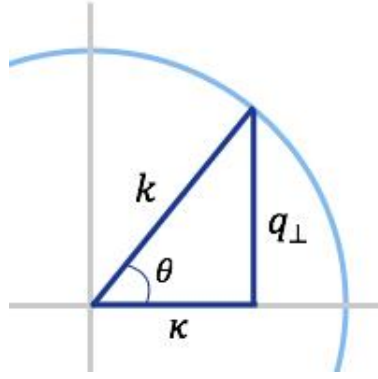


Fig. 1.6. Representation of the wave vector and the diffraction angle relationship in the Ewald sphere.

Applying the paraxial approximation, one can expand κ to the first non-zero order in q_{\perp} , and Eq. 1-5 becomes

$$\psi(r_{\perp}, z) = \mathcal{F}^{-1} \left[\tilde{\psi}(q_{\perp}) e^{ikz \left(1 - \frac{q_{\perp}^2}{2k^2}\right)} \right] \quad (\text{Eq. 1-10})$$

One gets the small angle scattering version of Eq. 1-8:

$$I \propto \left| \tilde{\psi} \left(q_{\perp} = k \frac{r_{\perp}}{z} \right) \right|^2 \quad (\text{Eq. 1-11})$$

Note here that the Fraunhofer diffraction approximation is valid when the Fresnel number $FN \ll 1$, which is defined as

$$FN = \frac{a^2}{\lambda z} \quad (\text{Eq. 1-12})$$

where a is the characteristic dimension of the object. Small and large Fresnel numbers correspond to respectively the far field regime and the near field regime. In the Fraunhofer diffraction regime (far field), one should have

$$\frac{a^2}{\lambda} \ll z \quad (\text{Eq. 1-13})$$

1.2b Image formation in lens-less imaging: Object transmittance

As shown in Eq. 1-11, the measured diffraction pattern is proportional to the absolute value of the Fourier transform of the exit wave in the transverse plane. The question now is: what is the relation between the object image and the exit wave that we can reconstruct by computational algorithms? For our experiments, we use the projection approximation: the exit wave is the product of the incident wave and the object transmittance:

$$\psi_{exit} = \psi_{incident} t_{object} \quad (Eq. 1-14)$$

In this approximation, the object can be treated as a two dimensional plane whose thickness is negligible, thus there is no diffraction inside the object. The object transmittance (in two dimensions with complex values) represents the projection of the object on a transverse plane (object plane in Fig. 1.5), which shows how the object modifies the incident wave both in amplitude and in phase. Since we assume that the incident wave is a plane wave, the detected wave (diffraction wave) in the far field is then equal to the Fourier transform of the object transmittance. The reconstruction image that we get by computational algorithms should then reflect the object transmittance. To valid the projection approximation, the object should be “*optically thin*”. If e is the object thickness and d is the reconstruction resolution that we want to attend, then the “*optically thin*” condition can be described as

$$e < \frac{2d^2}{\lambda} \quad (Eq. 1-15)$$

The term $\frac{2d^2}{\lambda}$ describes the “*depth of focus*” (DOF), which is also a function of diffraction angle θ_{max} :

$$DOF = \frac{2\lambda}{\theta_{max}^2} \quad (Eq. 1-16)$$

When the object thickness is smaller than the DOF, the exit wave is associated to a single object plane, which corresponds to the reconstruction plane visualized with computational algorithms. Otherwise, there will be more than one object plane, thus more than one possible phase associated to the measured diffraction pattern. This can prevent convergence of iterative algorithms. One may need additional constraints on the object support to associate one and only one object plane for the reconstruction. In holographic experiments (FTH, HERALDO), the phase information is encoded in the hologram. Thus, there is one unique solution obtained in the plane of the object and the reference.

To conclude, in our lens-less imaging experiments, objects are “optically thin” and the diffraction wave is detected in the far field regime (Fraunhofer diffraction) in the small angle scattering regime.

1.2c Image formation in lens-less imaging: Detection

The detection of the diffraction pattern is realized by a CCD camera, which accumulates incoming photons (diffraction and noise) during the exposure time. Thus temporal information such as the phase of the wave function is lost during the detection. This is the *phase problem* well known in lens-less imaging. The measured

term is the photon flux, whose unit is $\frac{J}{m^2}$ or $\frac{\text{photons}}{m^2}$. Eq. 1-11 becomes (if we omit the constant factors)

$$F = I = \left| \psi \left(q_{\perp} = k \frac{r_{\perp}}{z} \right) \right|^2 \quad (\text{Eq. 1-17})$$

The measured diffraction signal (F) is then digitalized with a certain sampling ratio. We can use a discrete Fourier transform function to present the numerical data. The one-dimensional discrete Fourier transform of a N long vector f_m is

$$\tilde{f}_n = \frac{1}{\sqrt{N}} \sum_{m=0}^{N-1} f_m e^{\frac{2\pi i n m}{N}} \quad (\text{Eq. 1-18})$$

If a continuous function $f(x)$ is sampled by a sampling interval Δx , and its discrete Fourier transform is also sampled by a sampling interval Δq , then we have the following relation:

$$\Delta x \Delta q = \frac{2\pi}{N} \quad (\text{Eq. 1-19})$$

With a given sampling interval Δx , the highest frequency present in a discrete Fourier transform is the Nyquist frequency:

$$q_{\text{Nyquist}} = \frac{N \Delta q}{2} = \frac{\pi}{\Delta x} \quad (\text{Eq. 1-20})$$

In our diffraction experiments, when applying the Fourier transform on the detected diffraction signal, we get the autocorrelation of the object (or the object transmittance). The Eq. 1-19 becomes

$$\Delta k = \frac{2\pi}{N\Delta r} \quad (\text{Eq. 1-21})$$

where Δk is the pixel size of the CCD camera which contains $N \times N$ pixels, and Δr is the pixel size of the autocorrelation of the object transmittance. If the object transmittance occupies a region of $n \times n$ pixels in the matrix of $N \times N$ pixels and the object size is $a \times a$, we can deduce the relation between real physical terms and the discrete functions:

$$\frac{k}{z} = n\Delta r \quad (\text{Eq. 1-22})$$

During the phase retrieval reconstruction process, the sampling ratio is a key factor. When the sampling interval is too large, frequencies higher than the Nyquist frequency will be wrapped and will appear as lower frequencies. This is called “aliasing”. A suitable diffraction pattern for the reconstruction should be “oversampled”. The notion of “oversampling” is first proposed by D. Sayre in 1952 [19] using the Shannon sampling theorem for the phase problem in crystallography. The oversampling is possible only if the object transmittance is contained in a “support” (non-zero inside the support and null outside). We can define the oversampling ratio [20] as:

$$O = \frac{A_{\text{FOV}}}{A_{\text{object}}} = \frac{N_{\text{measured}}}{N_{\text{object}}} \quad (\text{Eq. 1-23})$$

where A_{FOV} is the “field of view” corresponding to the image containing N_{measured} pixels of measured amplitudes, in which the object occupies an area A_{object} of N_{object} pixels. Since the object transmittance is a complex-valued, there are $2N_{\text{object}}$ real variables to be recovered. The whole image provides N_{measured} equations. By considering the degrees of freedom of such a set of equations, one cannot get a unique solution unless: $2N_{\text{object}} \leq N_{\text{measured}}$. Therefore,

$$O \geq 2 \quad (\text{Eq. 1-24})$$

Another approach to the oversampling ratio is based on Nyquist–Shannon sampling theorem [21,22]. According the theorem, the sampling interval Δk (the pixel size of the CCD camera) of the diffraction pattern should obey

$$\Delta k \leq \frac{2\pi}{2q_{\text{Nyquist}}} \quad (\text{Eq. 1-25})$$

where q_{Nyquist} is the maximum frequency detected in the diffraction pattern. Since in the reciprocal space of the diffraction pattern, the maximum frequency is given by the size of the autocorrelation of the object that is the double of the object size, we deduce from Eq. 1-20:

$$q_{\text{Nyquist}} = \frac{2n\Delta r}{2} = n\Delta r \quad (\text{Eq. 1-26})$$

Applying Eq. 1-26 to Eq. 1-25, we get

$$\Delta k \leq \frac{2\pi}{2n\Delta r} = \frac{\lambda z}{2a} \quad (\text{Eq. 1-27})$$

From Eq. 1-21, Eq. 1-22 and Eq. 1-23, one can get the relation between Δk and the oversampling ratio:

$$O = \frac{\lambda z}{a\Delta k} \quad (\text{Eq. 1-28})$$

Therefore, we recover the oversampling condition as Eq. 1-24.

Note that Eq. 1-24 is a necessary condition for solving a unique reconstruction, but in general not sufficient. In one dimension case, the uniqueness is never guaranteed [23,24]. Fortunately, in case of more than one dimension, the uniqueness is almost guaranteed with an oversampled diffraction pattern [9,10].

When a diffraction pattern is taken, the theoretical resolution (which is diffraction limited) can be calculated as:

$$r = \frac{1}{2\sigma_{\max}} = \frac{\lambda z}{N_{\text{pixel}} P_{\text{pixel}}} \quad (\text{Eq. 1-29})$$

where σ_{\max} is the largest spatial frequency of the diffraction signal recorded by the CCD camera, N_{pixel} and P_{pixel} are respectively the corresponded pixel number and pixel size. This equation gives the first insight of the diffraction pattern quality.

I.3 Reconstruction: Phase retrieval algorithms

The phase retrieval algorithms for lens-less imaging are inspired by those used in crystallography. The first phase retrieval algorithm is proposed by Gerchberg and Saxton in 1972 [25]. The Gerchberg-Saxton algorithm can reconstruct an object using two intensity measurements (one in Fourier space and one in direct space), which

introduced the “modulus constraint” notion in the iterative process. In late 70’s, Fienup has improved this algorithm by using only one intensity measurement in the Fourier space (the diffraction pattern) to reconstruct the object [7,8]. Fienup’s hybrid input-output algorithm (HIO) has a significant contribution to the imaging community and is probably the most popular phase retrieval algorithm nowadays. In general, there are four steps in the iterative process (Fig. 1.7)

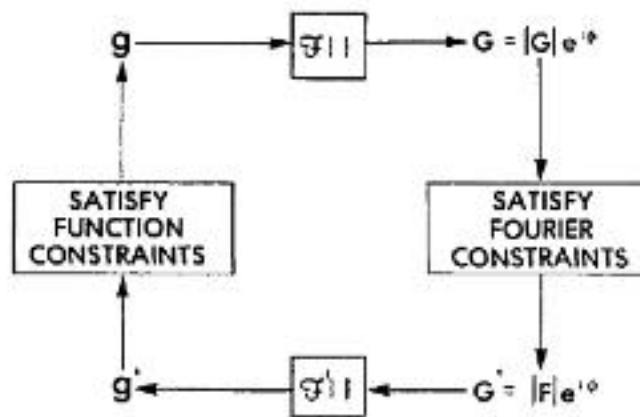


Fig. 1.7. Scheme of the phase retrieval algorithm. Picture extracted from Ref 6.

- 1) Apply the Fourier transform to the object (g): $G = |G|e^{i\phi}$ to get the phase term ϕ .
- 2) Apply the constraint in Fourier space (replace the amplitude by the measured diffraction intensity ($|F|$): $G' = |F|e^{i\phi}$.
- 3) Apply inverse Fourier transform on the G' to get g' .
- 4) Apply the constraint in direct space (such as the object support) to get object (g).

To start the iteration, one uses a random phase ϕ_r in step one. During the iterative process, an error factor based on the satisfaction of the constraints is calculated. A reconstruction solution can be achieved when the error factor is minimized (or under a fixed threshold).

In 2003, V. Elser has proposed a more general phase retrieval algorithm, the “difference map” [26], which is based on the “projections” of solutions on “constraints sets spaces”. The notion “constraints sets” (presented by C_1, C_2, C_3, \dots) are defined as subsets of a finite-dimensional Hilbert space (\mathcal{E}). The “constraints sets” can have two or more constraints corresponding to real physical meanings, such as the measured diffraction pattern intensity, the object support in direct space, etc. The goal of the reconstruction algorithm is to find the solution $x \in \mathcal{E}$, which satisfies:

$$\mathbf{x} \in \mathbf{C}_1 \cap \mathbf{C}_2 \cap \mathbf{C}_3 \cap \square \quad (\text{Eq. 1-30})$$

The notion “projection” (P_C corresponding to a constraint(C)) is then defined as: for every $x \in \mathcal{E}$ returns a point $P_C(x) = y \in C$ and such that $\|x - y\|$ is minimized. The condition (1-30) then becomes

$$x_{\text{sol}} = P_{C_1}(x_{\text{sol}}) = P_{C_2}(x_{\text{sol}}) = P_{C_3}(x_{\text{sol}}) = \dots \quad (\text{Eq. 1-31})$$

For a two-constraint problem, the difference map iteration can be defined as:

$$x_{n+1} = x_n + \beta D(x_n) \quad (\text{Eq. 1-32})$$

where

$$D(x) = y_2 - y_1 \quad (\text{Eq. 1-33})$$

$$y_2 = P_1[(1 + \gamma_2)P_2(x) - \gamma_2 x]$$

$$y_1 = P_2[(1 + \gamma_1)P_1(x) - \gamma_1 x]$$

where β , γ_1 and γ_2 are complex parameters.

Note that the HIO is a special case of the difference map when $\gamma_1 = -1$ and $\gamma_2 = \beta^{-1}$, which can be presented as

$$x_{n+1} = x_n + \beta [P_S((1 + \beta^{-1})P_M(x_n) - \beta^{-1}x_n) - P_M(x_n)] \quad (\text{Eq. 1-34})$$

where P_S and P_M are respectively the constraints on the object support and the measured diffraction signal.

The Relaxed Averaged Alternating Reflections (RAAR) algorithm is another popular algorithm proposed by Russel Luke in 2005 [27]. This algorithm can be defined as

$$x_{n+1} = x_n + \beta [P_S(2P_M(x_n) - x_n) - P_M(x_n)] + (1 - \beta)(P_M(x_n) - x_n) \quad (\text{Eq. 1-35})$$

Note that when $\beta = 1$, it is equivalent to the HIO.

During the last decade, many algorithms have developed (not presented here) and it is hard to say which algorithm is the best. Each algorithm is proposed for specific problems and applications. The experiments conditions and criterion of constraints for each algorithm is hardly the same. Some works [28, 29] comparing different

phase retrieval algorithms suggest that the HIO is the most efficient algorithm for well-controlled scattering experiments.

In this thesis work, phase retrieval reconstructions are realized using two computational codes:

- 1) The “Hawk” code [30] developed by our collaborator Filipe Maia in the research group of Professor Janos Hajdu in Uppsala University, Sweden. The code “Hawk” contains a set of phase retrieval algorithms, for example HIO and RAAR. I usually use the HIO algorithm for preliminary reconstruction of experiment data, and a combination of algorithms to get better reconstruction results.
- 2) The code “difference map” code developed by Pierre Thibault in the research group of Professor Veit Elser in Cornell University, USA.

Practically, the solution (reconstructed image) is not exactly the same from one iteration to the other one. After sufficient iterations (typically several hundreds of iterations), each iteration gives a very similar reconstruction solution with a corresponding error factor value. The error factor value is calculated based on the measured diffraction pattern and shows how “close” the reconstruction is compared to the measured data. One usually averages all reconstruction solutions whose error factor values are lower than a defined threshold to get the final image of the object. The resolution of reconstructed image is then estimated by the Phase Retrieval Transfer Function (PRTF) (Chapter III, section III.4).

I.4 Reconstruction: FTH and HERALDO

The phase problem is easily solved in FTH, which is a great advantage compared to the phase retrieval algorithms. But FTH involves more strict constraints on the sample preparation, which is not obvious in certain applications. In FTH, a pinhole (reference) is placed in the vicinity of the object at a certain distance (holographic separation) in the same transverse plane (object plane in Fig. 1.5). The entire sample (object + reference) transmittance can be defined as

$$t = o + r \tag{Eq. 1-36}$$

where o and r are respectively the transmittance of the object and the reference. As mentioned in the previous section, in Fraunhofer diffraction regime and projection

approximation, the measured hologram (the diffraction pattern) by CCD camera is the module square of the Fourier transform of the sample transmittance:

$$H = |\mathcal{F}\{t\}|^2 \quad (\text{Eq. 1-37})$$

The holographic lens-less technique offers a direct and non-ambiguous reconstruction. When applying the inverse Fourier transform to the measured hologram, according to the property of the autocorrelation (presented at the beginning of the chapter), we get

$$\mathcal{F}^{-1}\{H\} = \mathcal{F}^{-1}\{|\mathcal{F}\{t\}|^2\} = t \otimes t \quad (\text{Eq. 1-38})$$

Developing this equation, we have

$$\mathcal{F}^{-1}\{H\} = t \otimes t = o \otimes o + r \otimes r + r \otimes o + o \otimes r \quad (\text{Eq. 1-39})$$

The first two terms $o \otimes o + r \otimes r$ are the “central” terms, which correspond to the autocorrelations of the object transmittance and the reference transmittance. These two terms are centered and overlap at the origin. The last two terms, i.e. the complex conjugates $r \otimes o + o \otimes r$, are the holographic reconstructions located at the opposite sides of the “central” terms. Note that they are not two independent reconstructions, since they are complex conjugate “mirror” of each other. The FTH reconstruction is not the object transmittance itself but the cross-correlation between the object transmittance and the pinhole reference. In addition, one should respect the “holographic spatial separation” between the object and the reference to avoid the spatial overlap between the reconstruction terms and the “central” terms. If a is the size of object, then the distance between the object and the pinhole reference should be larger than $1.5a$.

The spatial resolution of the object image is limited by the size of the pinhole reference. A large reference will lower the resolution whereas a small one will increase it. Since the signal quality of the hologram depends also on the reference signal strength, there is a contradictory for the choice of the pinhole size. To optimize the reconstruction quality, the basic idea is to find strategies to increase the reference signal while keeping the reference size small. Various techniques have been proposed such as multiple references FTH [31], FTH with a well-prepared extended reference and deconvolution operator for reconstruction [32,33,34], massively parallel X-ray holography [35], holography with a well-prepared mask reference [34,35], etc.

HERALDO has been proposed to overcome the “paradox” in FTH. The pinhole reference in FTH configuration is replaced by an extended reference, such as a slit (1 Dimension), a rectangular (2 Dimensions), a triangle (2D), and etc. The extended reference $r(x, y)$ is placed close to the object $o(x, y)$ in the same transverse plane with a given holographic spatial separation. The measured hologram H has the same equation as Eq. 1-37. A linear differential operator $L^{(n)}\{\cdot\}$ is applied to the Fourier transform of the hologram. We then get the sum of a point Dirac delta function at (x_0, y_0) and some other function $g(x, y)$:

$$L^{(n)}\{r(x, y)\} = A\delta(x - x_0)\delta(y - y_0) + g(x, y) \quad (\text{Eq. 1-40})$$

where A is an arbitrary complex-valued constant, and $L^{(n)}\{\cdot\} = \sum_{k=0}^n a_k \frac{\partial^n}{\partial x^{n-k} \partial y^k}$ is an n -th order linear differential operator and a_k are constant coefficients. Note that the function $g(x, y)$ can be another Dirac delta function or any extended function.

Applying such linear differential operator on the autocorrelation (the inverse Fourier transform of the measured hologram), we have

$$\begin{aligned} L^{(n)}\{\mathcal{F}^{-1}\{H\}\} &= L^{(n)}\{t \otimes t\} \\ &= L^{(n)}\{o \otimes o\} + L^{(n)}\{r \otimes r\} + [L^{(n)}\{r\} \otimes o] + (-1)^n [o \otimes L^{(n)}\{r\}] \end{aligned} \quad (\text{Eq. 1-41})$$

According to the relation between cross-correlation and convolution when applying the differential operator, one get

$$L^{(n)}\{f \otimes g\} = (-1)^n [f \otimes L^{(n)}\{g\}] = [L^{(n)}\{f\} \otimes g] \quad (\text{Eq. 1-42})$$

Applying this property on Eq. 1-41, we get

$$\begin{aligned} L^{(n)}\{\mathcal{F}^{-1}\{H\}\} &= L^{(n)}\{t \otimes t\} = L^{(n)}\{o \otimes o\} + L^{(n)}\{r \otimes r\} + (-1)^n o \otimes g + g \otimes o \\ &\quad + (-1)^n A^* o(x + x_0, y + y_0) + A o^*(x_0 - x, y_0 - y) \end{aligned} \quad (\text{Eq. 1-43})$$

As similar to FTH, the last two complex conjugate terms are the reconstructions located at opposite sides of the central autocorrelation terms. Unlike FTH, the reconstruction resolution is not limited by the reference size. Practically, the resolution is closely dependent on the “sharpness” of the reference edge that determines the Dirac delta function. For example, the two extremes of slit and the corners of rectangular and triangle define respectively 2, 4 or 3 references.

The “HERALDO separation conditions” have a similar constraint like the FTH one: the features of the extended reference that will “produce” the Dirac delta function should have a minimum distance of $2a$ to the object, where a is the object size. An additional constraint should be respected to avoid the overlap between different reconstructions associated to different Dirac delta functions when there is more than one Dirac delta function: the distance between any pair of two features that “produce” Dirac delta functions should be larger than the object size a .

I.5 Beam requirements for lens-less imaging

CDI and HERALDO are both lens-less imaging techniques. As mentioned before, these two techniques can be realized using the same experimental setup, only the sample arrangement differs. The image reconstructions are performed separately using either a phase retrieval algorithm in CDI or direct mathematical operations in HERALDO. Obviously, high quality diffraction pattern is the key factor for both CDI and HERALDO (also for FTH). For a high-resolution reconstruction, we need a beam with the following requirements:

- Short wavelength
- High coherence
- High beam flux
- Ultrashort pulse duration

Short wavelength and ultrashort pulse duration are required to get high spatial resolution (nanometric scale or even atomic scale) and to perform dynamic studies on a femtosecond scale (or even attosecond scale in a near future). High coherence and beam flux ensure a high quality diffraction pattern with a good signal to noise ratio. Free Electron Laser facilities (FEL), Synchrotron facilities and High order harmonics beam lines are all qualified sources. In this thesis work, I have been interested in lens-less imaging techniques (CDI and HERALDO) using bright high order harmonics (HH) beam source. The High flux harmonic beam line developed at Saclay can provide intense coherent photons in the soft X-ray region (from several nanometers to several tens of nanometers) with brief pulse duration (typically in the femtosecond scale or even down to the attosecond scale). Compared to large-scale laser facilities, the inexpensive cost and relatively easy construction of harmonic beam line are of great advantage. The full control of beam properties makes it accessible to numerous applications from physics to biology. It is becoming a powerful imaging tool for users in various scientific domains.

I.6 Conclusion

This chapter has presented first the principle of lens-less imaging, in which the main obstacle for image reconstruction is the phase problem caused by the detection mechanism of the CCD camera. The phase retrieval algorithms and the Fourier transform holography are two main approaches to solve the phase problem. The former is an iterative process based on oversampling and constraints in both Fourier and direct space, while the latter encodes phase information into hologram by interference between object and reference. A discussion of the requirements of the suitable source for such imaging techniques has shown the potential of the high-order harmonic beam source, which provides high coherent and ultrafast (femtosecond scale) beam of short wavelength with a sufficient photon flux. A brief introduction of HHG is then presented, following by an introduction of the imaging formation process that occurs in lens-less imaging experiments. I present then several phase retrieval algorithms and the principle of holography style techniques (FTH, HERALDO) that are used for the scattering experiments realized during my PhD studies. A suitable source to perform ultrafast coherent imaging in the soft X-ray is the high harmonic generation. I briefly recall the principle of the source and more details are given about the practical aspects of source in the following chapter.

Chapter II -High harmonic generation

This chapter is a brief introduction to the High order Harmonics Generation (HHG) process. The purpose is to give few basics to understand the optimization of the source discussed in Chapter II. The more fundamental aspects of HHG are not presented here. We then describe the experimental set-up used at the CEA beamline and its performance.

II.1 Introduction

Thanks to the invention and the fast development of the laser, the research of light-matter interaction entered into a new era. At the end of the 20th century, powerful lasers can deliver peak intensities up to 10^{18} W/cm², which makes it possible to realize the frequency up-conversion from visible to the extreme ultra violet (XUV) domain. The HHG phenomenon is first discovered by research groups in Chicago [1] and in Saclay [2] at almost the same time (in 1987). They have observed intense harmonic emission by the atoms of a rare gas jet of a focused ultra-short infrared laser (Fig. 1.8a). In the studies conducted here, Argon (Ar), Krypton (Kr) and Xenon (Xe) gases have been mostly used. A typical spectrum is shown in Fig. 1.8b.

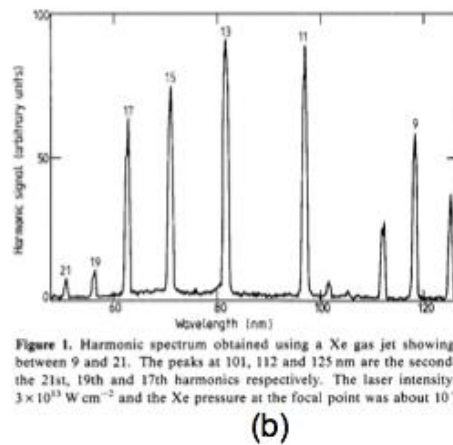
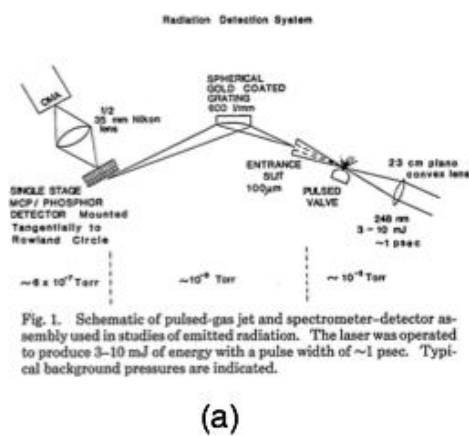


Fig. 1.8. (a) Scheme of HHG observation, picture extracted from Ref [3]. (b) HHG spectrum obtained using Xe gas jet, picture extracted from Ref [4].

The HHG phenomenon can be described in a semi-classic three-step model: tunnel ionization, classical acceleration and recombination (Fig. 1.9) [5,6].

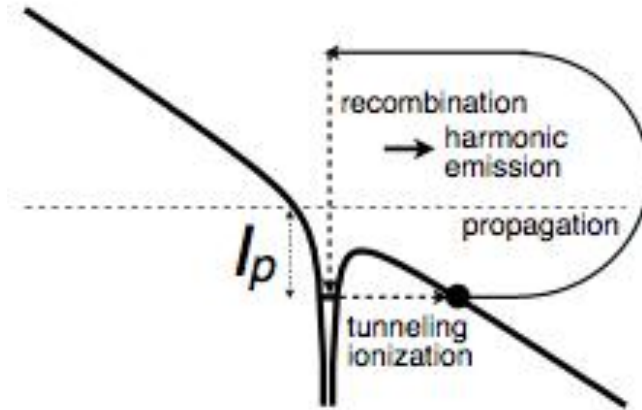


Fig. 1.9. Three-step model of high order harmonic generation.

In the first step, when close to the maximum of laser electric field that lowers the potential barrier, an electron can go through by tunnel effect. In the second step, the influence of atomic Coulomb potential is neglected. The electron is accelerated in the electric field. When the sign of the electric field changes, the electron might be driven back towards the ionic core, with whom it can recombine in the third step.

The recombination gives rise to the emission of a burst of soft X-ray light. The photon energy is equal to the sum of the electron kinetic energy acquired during its oscillation in the electric field and the ionization potential (I_p) of the atom/molecule. The maximum photon energy is governed by Eq. 1-44, which is called “cut-off” [5]. U_p is the ponderomotive energy -- the cycle averaged quiver energy of a free electron in an electric field.

$$\hbar\nu_{max} = I_p + 3.17U_p \quad (\text{Eq. 1-44})$$

Depending on the different behavior of electrons, there are two trajectories of recombination: long and short, which contributes differently to HHG. The spatial and spectral properties of the harmonic emission differ for each trajectory.

The spectrum of high order harmonics has a characteristic form, which contains three parts: the perturbative region, the *plateau* and the *cut-off* (Fig 1.10). It can be well calculated using a semi-classical model except the behavior of the *cut-off* region. Accurate HHG calculations are now obtained using a quantum model based on the strong field approximation (Lewenstein model) [7].

Since the HHG process is triggered by the laser’s electric field, the emitted photons are coherent, which is the basic for lens-less imaging. HHG has other advantages, such as the attosecond pulse structure, which is demonstrated in form of attosecond pulse train in 2001 [8]. We can also cite its natural synchronization with the driving infrared laser, which makes it suitable for ultrafast dynamics studies in a pump-probe geometry. I also would like to point out that the

HHG source has been used to seed a soft X-ray FEL resulting in pulse with improved temporal coherence [9].

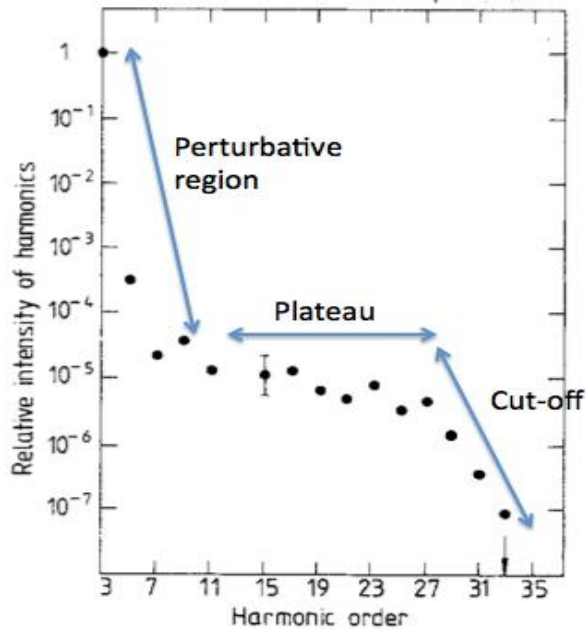


Fig. 1.10. A typical spectrum of HHG with three parts: perturbative region, *plateau* and *cut-off*. The original spectrum is extracted from Ref 22.

Practically, in the context of the application of HHG in lens-less imaging, we usually choose the harmonics in the *plateau*. They are usually more intense and stable than the *cut-off* harmonics. We also select through phase matching the short trajectory that exhibits better spatial and spectral coherence properties than the long trajectory.

II.2 Experimental set-up

All the imaging experiments in this thesis work have been accomplished using the High flux harmonic beamline at the CEA Saclay research center, France. The harmonic beamline is a table-top femtosecond soft X-ray harmonic source driven by the table-top infrared femtosecond laser LUCA (Laser Ultra Court Accordable). LUCA is a Ti:sapphire laser system, which delivers up to 50 mJ energy pulses at 800 nm with a pulse duration of 50 fs and a repetition rate of 20 Hz. The experiment is composed of a lens stage (in air) and three experimental chambers (in vacuum). At the lens stage, a long focal length lens ($f = 5.56$ m) focuses the infrared beam into the gas cell located in the first experimental chamber. We can adjust the IR beam aperture by a diaphragm located in front of the lens. The lens is motorized by a translation stage in the beam propagation direction with a movement range of 15 cm, which offers an easy control of the relative position of the beam focus and the gas cell.

The three experimental chambers of the High flux harmonic beamline are (Fig. 2.1):

- 1) HHG chamber: Up to 50 mJ laser energy can be focused into a gas cell to generate harmonics beam. The gas cell is a metal tube with two pinholes at its extremes filled with rare gas. We have easy and full motorized control of the gas cell in vacuum: the cell length is variable from 0 to 15 cm and its lateral position (y direction) to the beam propagation direction (z) is motorized by a translation stage; we can also adjust the orientation of the cell in z direction by tilting it in x and y directions (perpendicular to z) with precision.
- 2) Optics chamber with “imaging configuration”: The harmonics and IR beams propagate together into the optics chamber. An IR antireflective mirror separates them and sends the harmonics beam to the diffraction chamber. The residual IR is then filtered by aluminum filters located between the optics chamber and the diffraction chamber.
- 3) Optics chamber with “spectrum configuration”: We can also replace the IR antireflective mirror by a pair of toroidal mirror and plane grating for spectrum studies. The thin slit and the photomultiplier tube (PMT) are located at the end of the setup. We can also replace the PMT by an XUV camera to measure the harmonic beam profile in the far field or even an XUV wave front sensor.
- 4) Diffraction chamber (Fig. 2.2): The multilayer parabolic mirror (coated by Institut d’Optique) selects one harmonic order (25th harmonic in our experiments) and focuses the beam onto the sample located at its focus. The CCD camera behind the sample holder detects the diffraction pattern in the far field regime.

This harmonic beamline has delivered its first photons in 2007. First demonstration of CDI reconstructions of a test object has been published in 2009. This has encouraged further studies in lens-less imaging and beamline optimization. This chapter will follow the time line to present the “High Flux Harmonic” beamline developments.

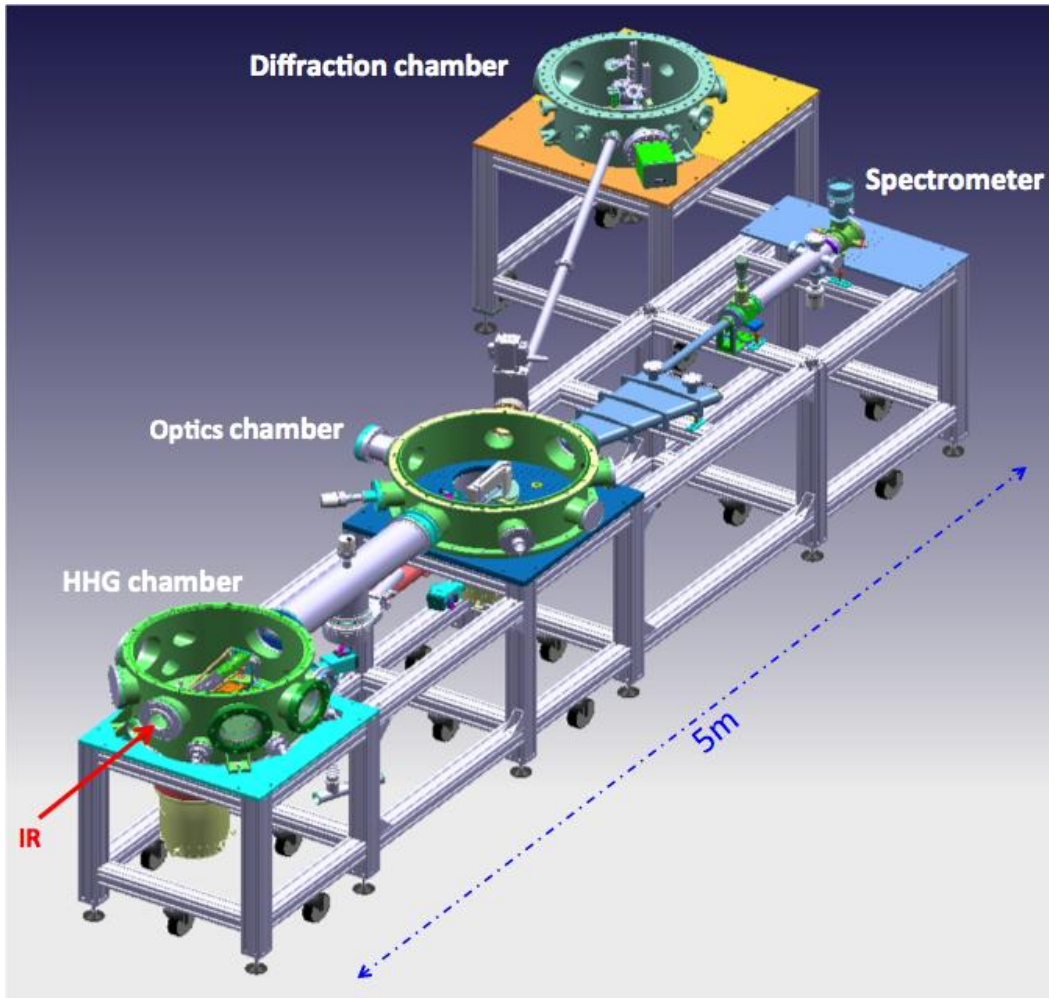


Fig. 2.1. Scheme of the High flux harmonic beamline. The red arrow at left bottom indicates the beam propagation direction. The infrared beam is first focused into a gas cell in the harmonic generation chamber. The optics chamber separates the harmonics beam from the IR beam and sends it into the diffraction chamber where the lens-less imaging experiments will take place. The optics chamber can also switch to a TM-PGM (Toroidal Mirror-Plane Grating Monochromator) type spectrometer for HHG studies. The entire setup is about 5 meters long.

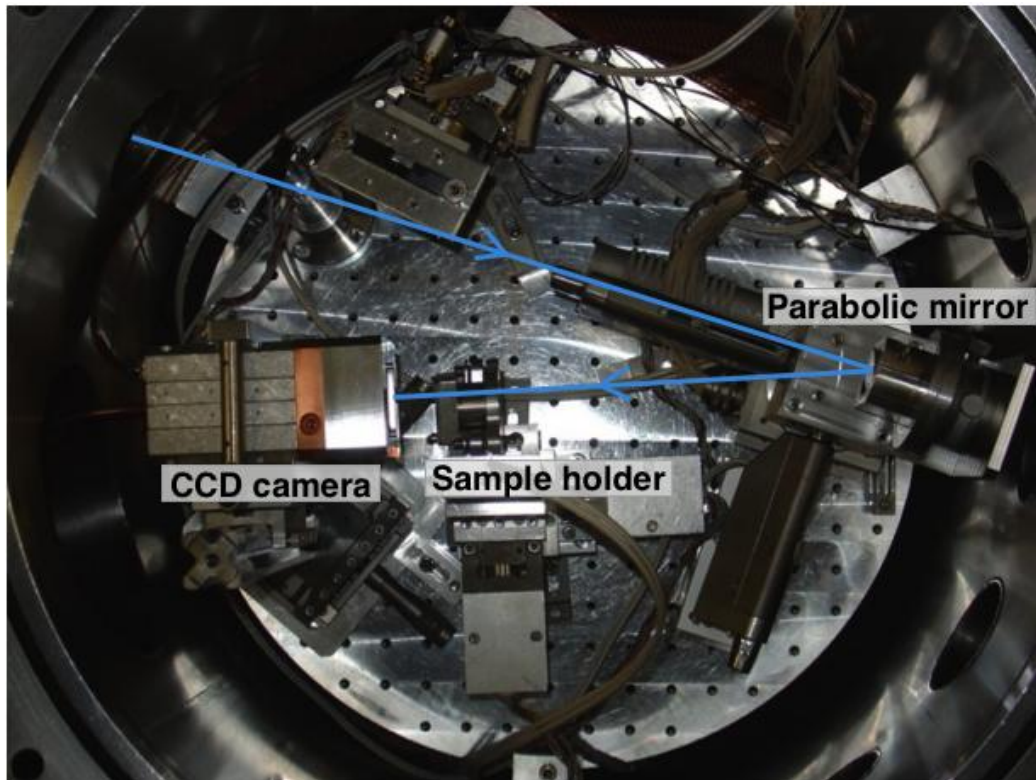


Fig. 2.2. Picture of the diffraction chamber. The parabolic mirror focuses the harmonics beam onto the sample, and the CCD camera located behind the sample holder detects the diffraction pattern.

II.3 HHG optimization and beamline standardization

I present in this section the effort to build a powerful, stable and reproducible harmonic beamline for imaging applications. The principle goal is to realize dynamical visualization (2D or 3D) of ultrafast physical phenomena on a femtosecond scale with nanometric spatial resolution. In coherent imaging, the X-ray photon flux on sample (single shot or multiple shots) determines the signal extension on the diffraction pattern (the maximum spatial frequency of the diffracted signal). A high signal extension corresponds to a high theoretical spatial resolution (Eq. 1-29, Chapter I). Moreover, the radiation damage of samples (especially biological ones) limits the maximum pulse energy for each shot, which is a real limitation for light sources that provides high average but low peak flux beam, such as synchrotrons. However, one can achieve high-resolution imaging with another strategy. The idea is to irradiate the sample with a single pulse short enough to capture the image before the onset of the radiation damage. The FEL or XFEL facilities can provide such X-ray pulses. HHG source has demonstrated such potential however further work was necessary to improve the quality of the CDI diffraction patterns. In this thesis work I present the optimization of the entire beamline (HHG process and all the optics) to finally get the maximum pulse energy available on sample for high-resolution single-shot

imaging. It has been also important to standardize the beamline to have stable beam performances, which was at the very beginning of my work unstable from day to day.

The harmonic beamline optimization has been realized in two steps:

- 1) HHG optimization: As mentioned before, we would like to maximize the harmonic pulse energy to get higher reconstruction resolution. However, it is not the only factor that influences the reconstruction quality. The wave front, the coherence and the spatial distribution of the intensity of the harmonic beam are also critical factors. The HHG optimization process conducted here has been to find an optimum compromise between all these factors to enhance the quality of diffraction patterns or holograms.
- 2) Focusing optimization: The sample is located at the focus of the parabolic mirror. The phase retrieval algorithms reconstruct the exit wave at the object plane (Chapter I, section I.2) that is equal to the sample transmittance in case of a plane wave illumination. Thus the harmonic beam focusing quality has a large influence on the reconstruction result. We need a homogenous focal spot and a proper spot size compared to samples.

We have used a Hartmann type wave front sensor to characterize and evaluate the quality of the generated harmonics beam before and after focusing optics (the parabolic mirror). The wave front sensor measures the wave front and the intensity of the harmonic beam, and reconstructs the beam profile using back-propagation functions. First we place the wave front sensor at a distance of 5 m from the gas cell without any focusing optics (Fig. 2.3). We measure the direct harmonics beam in far field and optimize the wave front as a function the HHG parameters, such as IR laser energy, IR beam aperture, gas cell length, gas pressure and etc. Then, we align the wave front sensor after the focus of the parabolic mirror to characterize and optimize the focal spot.

After the optimization process with the wave front sensor, we use a Young's double slits to characterize the harmonic beam coherence, and study the influence of the coherence on phase retrieval reconstructions. We measure the variations of the beam coherence using a similar process as the HHG optimization with the wave front sensor. The results show that it could be an alternative way to optimize the beamline, but less efficient and less accurate than the wave front sensor, because one has to check manually the fringe visibility of each interference pattern and only a small part of the beam is characterized in each measurement.

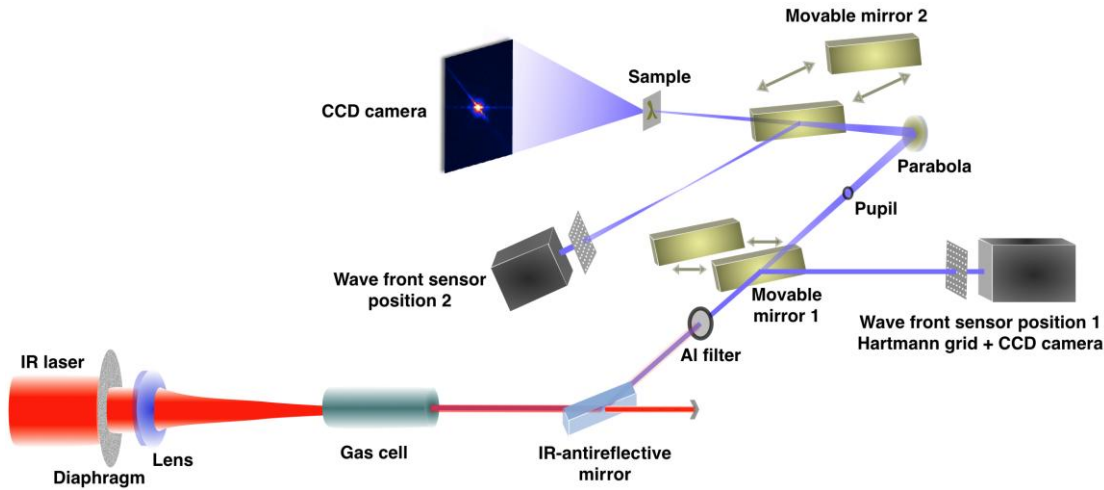


Fig. 2.3. Scheme of the optimization experiment setup. 1) HHG optimization configuration: Movable mirror 1 (multilayer plane mirror) is in and the wave front sensor is located at position 1 to measure the direct harmonics beam. 2) Focusing optimization configuration: Movable mirror 1 is out and mirror 2 is in; the wave front sensor is located at position 2 to measure the focused harmonic beam by the parabola. 3) Diffraction configuration: Two movable mirrors are out and no wave front sensor. The sample (Young's double slits) is located at the focus of the parabola and the XUV camera detects the diffraction pattern (far field interference of the slits exit waves).

II.3a HHG optimization and beamline standardization: wave front sensor

The Hartmann type wave front sensor "HASO" (produced by Imagine Optics Corp.) is composed of a Hartmann pattern grid and a XUV camera located 20 cm behind the grid (Fig. 2.4a). The harmonic beam goes through the Hartmann grid, which is an array of holes, and projects the "beamlets" sampled by each hole onto the XUV camera. The positions of the individual spot centroids are measured (Fig. 2.4c) and compared with reference positions (calibrated with perfect wave front, Fig. 2.4b). The measured local shifts of each beamlet can reconstruct the wave front of the harmonic beam. The measured beamlets present also the harmonic beam's intensity profile at a sampling rate of the grid. One can then deduce the aberrations of the beam. Using back-propagation functions, the harmonic beam profile at the point source can be reconstructed. These numerical calculations are realized within the paraxial approximation.

The wave front sensor is calibrated and provided by the research group of P. Zeitoun at Laboratoire d'Optique Appliquée (LOA), France. The Hartmann grid is 19 x 19 mm² large and contains 51 x 51 square holes that each is 80 x 80 μm² large and separated by 380 μm. The back-illuminated CCD camera has 2048 x 2048 pixels of 13.5 x 13.5 μm² each, operating at -40 °C. The typical calibration method is presented in Ref 14. In our case, a 10 μm pinhole positioned in the beam propagation path at 1 m from the gas cell output diffracts the beam and generates a

perfect wave front. The sensor accuracy is then experimentally measured to be $\lambda/50$ RMS (root mean square) at a wavelength $\lambda = 32$ nm, i.e. an accuracy of 0.64 nm RMS [10]. Note that an aberration of λ in amplitude corresponds to local phase aberration of 2π . One should be careful when using such a sensor to measure a wave front with very strong aberrations. The mismatch of beam lets and the reference positions could lead to wrong reconstruction of wave front if the aberration exceeds 2π . In our case, the harmonic beam has relatively weak aberrations so that the sensor is well adapted.

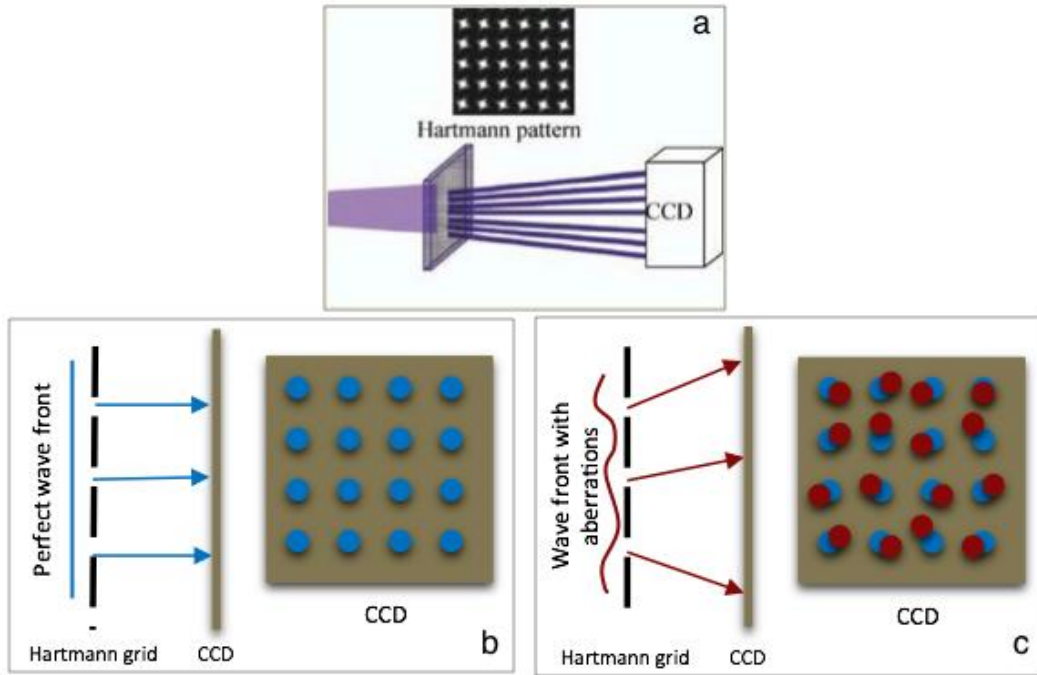


Fig. 2.4. Scheme of the Hartmann type wave front sensor. (a) The target beam goes through the Hartmann pattern grid, which is an array of holes, and projects onto the XUV camera behind. The XUV camera detects the sampled intensity of the beam. (b) The wave front sensor should be calibrated with a perfect beam before first use. The positions of the beam lets on the camera will be registered as reference positions (blue points). (c) The wave front is reconstructed from the measured local shift (red points) of each beam let compared to the reference positions.

In the first step, we have explored systematically several HHG parameters to optimize the harmonic flux and the beam wave front RMS value. The wave front RMS value describes how the measured wave front is distorted compared to a plane wave. According to the Maréchal's criterion, a beam is diffraction-limited at a given wavelength λ when the aberrant wave front amplitude is lower than $\lambda/14$ rms. As we assume a plane wave illumination in CDI, if the beam is far away from a plane wave, then the reconstruction will not correctly represent the sample transmittance but the ensemble exit wave (sample transmittance + incident wave). However, we can still extract the sample transmittance if we know the incident wave in priori, which requires a measurement of the incident wave front.

Practically, if the beam is not stable (aberrations change from shot to shot), simultaneous measurements of the incident wave and the sample diffraction pattern will be required. If the

beam is stable that measurements can be achieved in different shots, the relative position of the beam when hitting onto the sample should be known for extracting correctly the sample transmittance information.

In our experiment, we have optimized the wave front RMS value to the diffraction-limited ($\lambda/14$) and maximized the harmonic flux. The initial IR beam has a diameter of about 40 mm and is then limited in aperture by a diaphragm located in front of the focusing lens. We conclude the optimum parameters' value range: beam aperture = 20~21 mm, gas pressure = 8~9 mbar, gas cell length = 5~8 cm, effective laser energy = 15 mJ and the focus position is 2 cm behind the gas cell output. The beam aperture of 20~21 mm corresponds to a laser focal radius of 137~143 μm and the confocal parameter = 14,7~16 cm. The harmonic flux and the wave front RMS share the same optimum value range and are maximized with the same parameter values, which agrees with previous work [10].

For each wave front measurement, aberration contributions are calculated with Zernike polynomials, which is unstable from shot to shot. There is no obvious relation between aberration contributions and the harmonic generating conditions. Previously, two groups working on HHG optimization with wave front sensor reports trade-off conclusions of harmonic aberrations dependence on pump laser aberrations [10]. A further study on the aberration dependence of the High flux harmonic beamline is planned and it may lead to new HHG optimization.

The harmonic beam generated with optimum parameters has a wave front RMS of 0.11λ ($\lambda/9$), compared to a non-optimized harmonic beam whose wave front RMS is 0.79λ (Fig 2.5). Meanwhile, the spatial profile of the harmonic beam in far field has also been optimized, which is important for coherent imaging. The reconstructions of the harmonic beams at the source are shown in the Fig. 1 attached article.

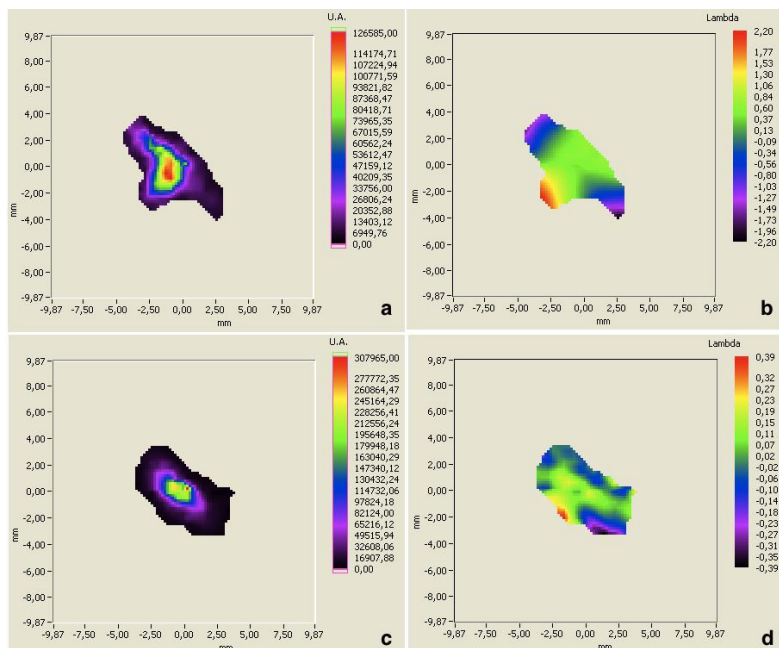


Fig. 2.5. Generating condition: gas pressure = 8 mbar, gas cell length = 8 cm, laser energy = 15 mJ, beam aperture = 24 mm for (a) and (b), and 21 mm for (c) and (d). (a) is the measured intensity and (b) is the measured phase of the non-optimized harmonic beam by the wave front sensor in far field. (c) and (d) are respectively the intensity and the phase of the optimized harmonic beam. Note that the absolute phase scales in (b) and (d) are different.

II.3.b HHG optimization and beamline standardization: Focusing optimization

In the second step, the wave front sensor is located behind the focus of the parabolic mirror to characterize the harmonic focal spot, which represents the illumination condition for coherent imaging. In the beam path from the harmonic source (output of the gas cell) to the sample (focus of the parabolic mirror), there are only two optics (IR-antireflective mirror and parabola) and one aluminum filter. The focusing quality, thus the illumination quality is strongly related to the alignment of the parabola. The parabola is motorized by translation stages and goniometers. It is initially aligned with residual IR beam as reference. The study with a wave front sensor allows direct measurements of the focusing quality with the harmonic beam (25th order) in the same condition as the coherent imaging. A fine adjustment is then possible for the parabola motorized in all translation and tilt directions to optimize the focal spot. Finally, the wave front sensor measurements in this configuration characterize the whole harmonic beam line until the diffraction stage by taking account of all elements in the beam line except the detection part. The optimization of the detection stage is associated to each particular imaging configuration, including sample conditions, imaging technique, final resolution, illumination quality, etc. It will be discussed in the following chapter.

Experimental results show that a fine adjustment of the parabola with the harmonic beam can optimize the focal spot's spatial profile and aberrations. Fig 2.6 shows the enhancement of the harmonic beam before and after the fine adjustment of the parabola. We get a harmonic beam of 0.154λ ($\sim\lambda/6$) RMS (Fig. 2.6d) instead of 0.326λ ($\sim\lambda/3$) RMS (Fig. 2.6b) measured at the Hartmann grid. Usually, the dominant aberration of the harmonic beam is the coma, which should be associated to the miss-alignment of the parabola. It is clearly observed in the reconstruction of the focal spot before fine adjustment. The focal spot after fine adjustment presents a homogenous and quasi-circular beam profile, with reduced coma aberration. The beam size (at $1/e^2$) is optimized from $7.8\ \mu\text{m}$ to $5\ \mu\text{m}$, which matches better our samples (usually within a window of $5 \times 5\ \mu\text{m}$). Compared to the $20\ \mu\text{m}$ focal spot used in the previous work of "music note" (also within a window of $5 \times 5\ \mu\text{m}$), the effective harmonic photons for diffraction are largely increased.

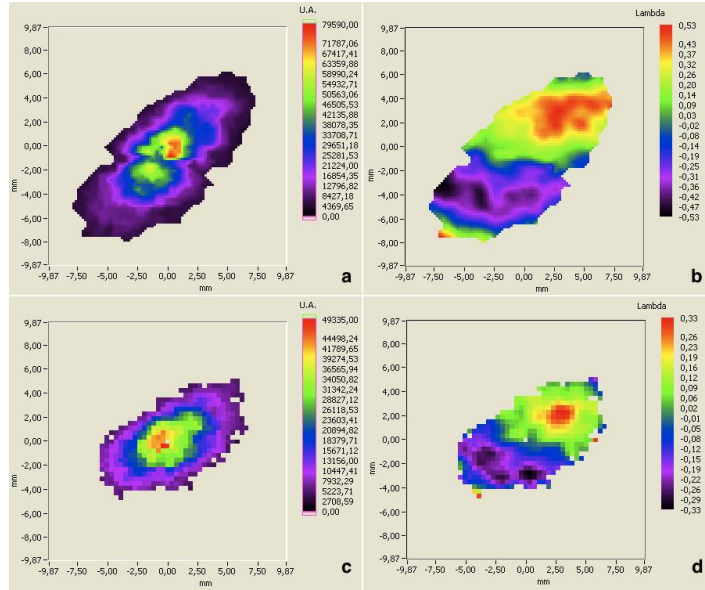


Fig. 2.6. (a) is the intensity and (b) is the phase of the 25th harmonic beam with initially aligned measured by wave front sensor. (c) and (d) are respectively the intensity and the phase of the harmonic beam with finely tuned parabola.

In the beam propagation direction (z direction), the focused harmonic spot changes quickly before and after the parabola focus position. The evolutions in both conditions (before and after fine adjustment) are similar, while the optimum adjustment provides quasi-circular focal spot in a range of ± 0.5 mm around the focal position, larger than in the other case (Fig. 2.7). This range is important for the coherent imaging as it give flexibility in positioning the sample. Usually, we use a sharp edge (for example, the edge of the sample membrane) to look for the focus position (Fig. 2.8). Typically, we can find the focus position with a precision of ± 0.2 mm, which fits the previous range of ± 0.5 mm. Note that a daily alignment of the IR laser during the initiating stage of the harmonic beam line is required, which could be critical for the harmonic focusing quality. The IR laser should be aligned as it was for the fine adjustment with wave front sensor to ensure an optimum focal spot. A permanent installation of wave front sensor in focusing optimization configuration could be a precise method for daily alignment, especially for experiment projects spanning over months. According to our experience, careful daily alignment (without wave front sensor) is sufficient for short-term experiments.

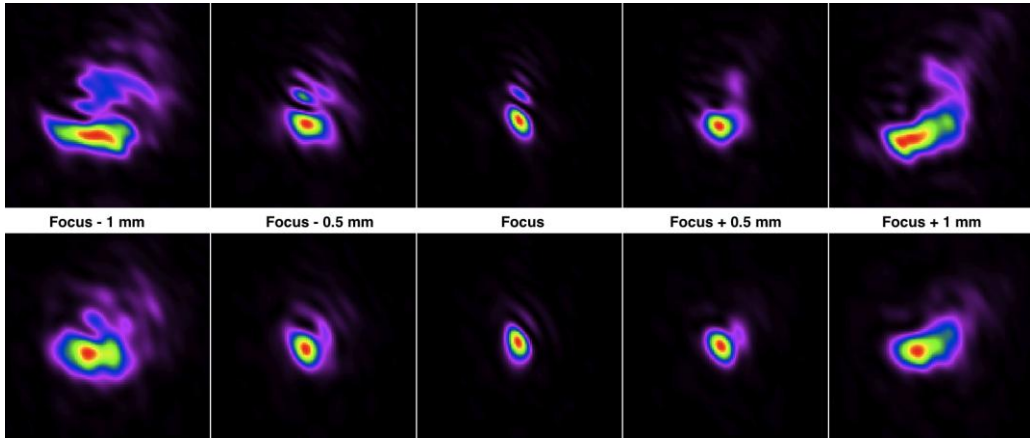


Fig. 2.7. The top line presents the evolution of the reconstructed harmonic beam spatial profile around the focus of the parabola before fine adjustment. The bottom line is for the case after fine adjustment.

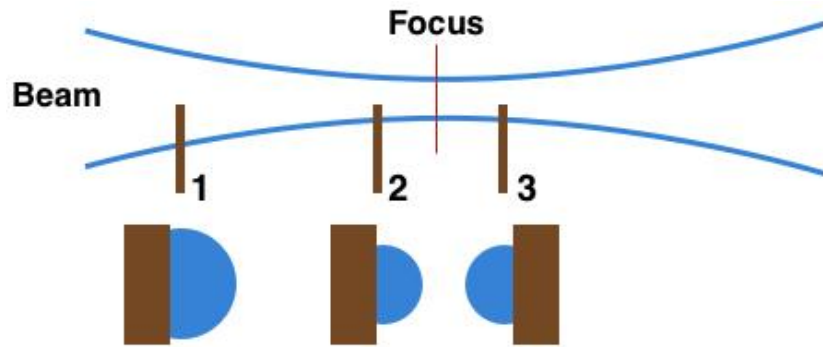


Fig. 2.8. Practically, to find the focus position of the beam, we move a testing edge (the brown squares) from position 1 to position 3 along the beam propagation direction at certain step. In position 1 and 2, the beam (blue circles) is cut from one side (for example, the left side). When we path the focus position, the beam will be cut from the opposite side (the right side in position 3). Then the focus position is fixed in a range and we can get more precise position by repeating the process with smaller step

II.3.d HHG characterization: spatial coherence at the focus

We are now interested in the behavior of the spatial coherence of the harmonic beam generated with different HHG conditions. We switch the harmonic beamline to the diffraction configuration and place a double Young slits at the sample position. The double slits are $1.5 \mu\text{m}$ long and 300 nm wide, separated by $4 \mu\text{m}$, fabricated by a nano-focused ion beam (FIB, CSNSM facility in Orsay University). The CCD camera records the interference pattern in the far field (19 mm behind the double slits). We use the similar exploration process of the HHG parameters as the optimization with wave front sensor. The studied parameters are gas cell length, gas pressure and beam aperture.

The evolutions of the fringe visibility and the diffraction pattern intensity are compared as a function of other generating parameters (Fig. 2.9 to Fig. 2.11). All the measurements are in single-shot regime. The measured fringe visibility is up to 0.8 ~ 0.84 in optimum range of HHG parameters, and lower than 0.5 in certain conditions. The fringe visibility, thus the spatial coherence of the harmonic beam, has the same evolution behavior as the diffraction intensity (which is proportional to the harmonic beam intensity at focus). We conclude that the harmonic flux, wave front quality and the spatial coherence can be optimized under the same HHG condition. These three factors are essential for coherent imaging. They influence the diffracted signal strength (or signal to noise ratio), the illumination wave front and the accuracy of the phase information encoded in the diffraction pattern.

Compared to the harmonic beam size (5 μm), the Young double slits (separated by 4 μm) measurements characterize the beam of its outer part. One should use a set of Young double slits separated by different distances to have a full characterization of the beam coherence (one measurement for one distance). Otherwise, a coherence-testing pattern can be used to measure the beam coherence of several different distances within one measurement.

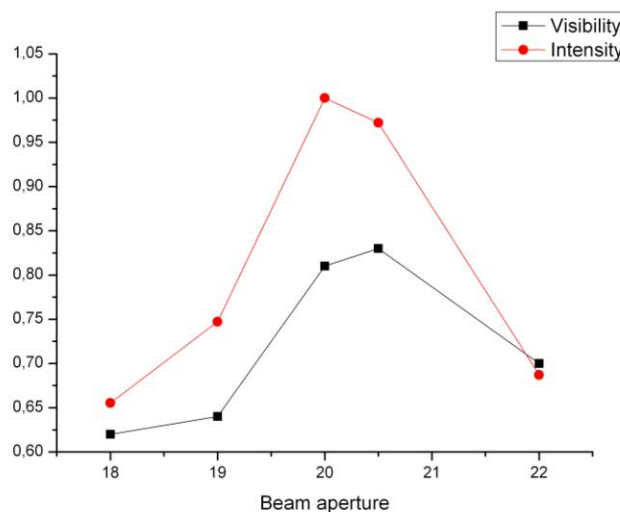


Fig. 2.9. The black and red curves present respectively the variations of fringe visibility and the diffraction pattern intensity as a function of beam aperture. The intensity curve is normalized to the maximum intensity detected.

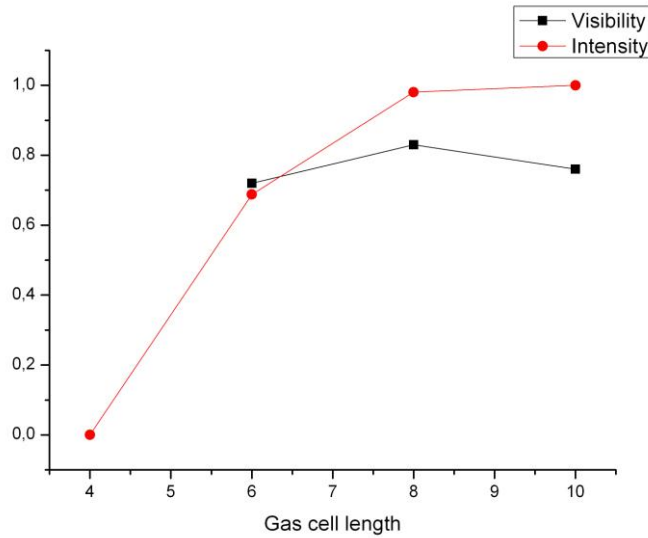


Fig. 2.10. The black and red curves present respectively the variations of fringe visibility and the diffraction pattern intensity as a function of the gas cell length. The intensity curve is normalized to the maximum intensity detected. Note that the diffraction intensity for gas cell length = 4 cm is too weak to be detected; however the direct harmonic beam without the presence of the double slits can be detected by the CCD camera.

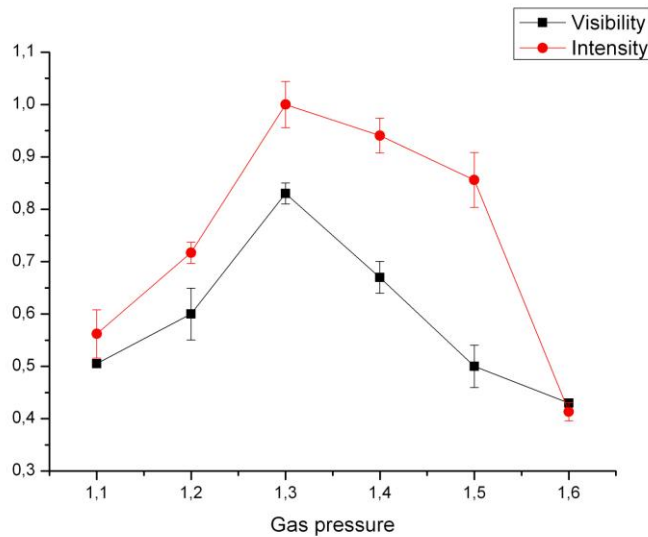


Fig. 2.11. The black and red curves present respectively the variations of fringe visibility and the diffraction pattern intensity in function of gas pressure. The intensity curve is normalized to the maximum intensity detected.

II.4 Laser Modal Filtering for HHG optimization

We have shown how the harmonic beamline, optics filters and also wave front and coherence can be controlled and improved. Is it possible to accomplish further optimization of the HHG properties by improving the driving laser beam? Since the HHG phase matching depends on the IR laser focusing quality and its propagation in the generating medium, the wave front and the spatial profile of IR laser along with its temporal properties have important roles in the HHG process. Some previous studies showed some correlation between the IR laser and the generated harmonic pulse of their wave fronts [10-11]. Further enhancement of the harmonic beam can be expected from spatial and/or temporal improvement of our IR laser beam. In practice, the IR beam (LUCA laser described earlier) before and after the temporal compression stage looks inhomogeneous with a triangle-like shape in the center part of the beam. There is a clear need of improving the spatial profile of the IR beam. The diaphragm that we located before the focusing lens to control the beam aperture is somehow a kind of spatial filter of the IR beam, which optimizes the HHG by adjusting its focal geometry, ionization and harmonic dipole properties [12]. However its application is quite limited. We have shown for example during the wave front studies that the HHG beam is strongly affected when the diaphragm is too widely opened. Phase matching is in particular destroyed when “bad” infrared modes superimposes in the HHG generating media.

In this section, studies of further improvement of the IR beam before injection into the gas cell will be presented, and followed by the results of HHG in condition of these improvements.

II.4a Modal Filtering: setup

There are various approaches to improve the IR beam quality. As cited above, the use of a diaphragm can optimize the HHG yield [12], a set of transmission phase plates can be used to create a flat-top laser beam to increase the interaction volume and the HHG efficiency [13], or using a truncated Bessel beam produced by argon-filled hollow fiber for HHG [14], or improving the laser wave front by deformable mirrors and genetic algorithms to optimize HHG efficiency [15], and etc. Our approach is inspired by the hollow fiber compression technique [16], which generates sub-10 fs laser pulses by a capillary filled with gas, called “*post compression*”. In our case, the fiber will not be filled with gases. We will mainly use the coupling between the laser modes and the fiber modes to improve the IR beam.

In the femtosecond regime, intense laser beam can easily lead to degradation of optical elements in the beam path, including the compression gratings. Therefore, we decide to place the hollow fiber before the compression stage and after the final amplification stage of LUCA laser. We then operate in picosecond regime, where related problems (mainly thermal problems) are easy to handle experimentally. The setup is shown in Fig. 2.12. A hollow-core fiber in silica of 30cm-long with a core radius $a = 125\mu\text{m}$ is located after the amplification stage of LUCA laser, which

delivers a laser beam of up to 180 mJ/pulse centered at 795 nm, at a repetition rate of 20 Hz, with a pulse duration of about 200 ps. The hollow-core fiber is operated in vacuum of about 10^{-3} mbar. The IR beam is first focused into the hollow-core fiber, then couples with the fiber mode and diverges at the fiber output. A set of lenses located after the fiber collimates the filtered IR beam into the compression stage. Finally, the compressed femtosecond laser beam (up to 50 mJ/pulse) is used for HHG.

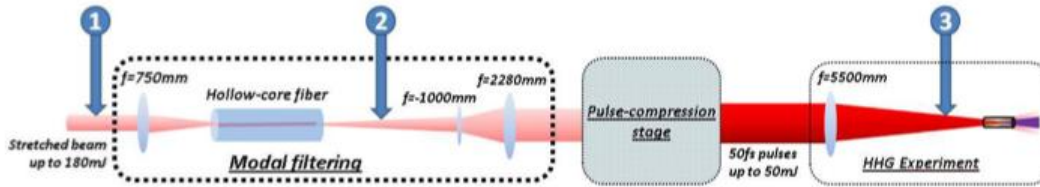


Fig. 2.12. Scheme of the modal filtering. The hollow-core fiber is located between the compression stage and the amplification stage of LUCA laser to filter the IR beam.

This scheme of hollow-core fiber is based on the theory of propagation of an electromagnetic wave in a cylindrical dielectric waveguide. In theory, the laser beam will be coupled with the fundamental mode of the fiber, which is EH_{11} in our case [17,18]. The reason to choose EH_{11} mode is because it has a similar transverse distribution as the Gaussian mode TEM_{00} in both near and far field. The optimum coupling efficiency of perfect a Gaussian mode is about 98%, corresponding a beam waist $\omega_0 = 0.65a$. It gives a first idea of the beam size at the entrance of the fiber. Moreover, the other guided modes are strongly attenuated during the propagation in the fiber. Thus, a spatial filter by modes selection of the laser beam is established. We call this technique “modal filtering”.

II.4b Modal Filtering: experimental results

The modal filtering is tested and quantified by several series of measurements of the laser beam by beam profilers and wave front sensor. We are interested in the laser beam’s spatial profile, the wave front quality, the modal composition, the pulse energy (energy transmission of the modal filtering) and its temporal properties after pulse compression stage, which are measured by a SPIDER interferometer [19]. The wave front sensor used here is a Shack-Hartmann type that the grid is an array of micro-lenses, instead of holes in XUV sensor, and using the same principle of wave front measurement. We quantify the laser beam at different stages with and without the presence of the modal filtering. Fig. 2.13 is an overview of the laser beam quality comparison, measured and simulated by wave front sensor.

The measurements and simulations have demonstrated the high efficiency of the modal filtering on the laser beam quality improvement. The experimental results and theoretical predictions agree with each other. A quasi-mono-mode diffraction-limited beam of up to 50 mJ pulse energy and pulse duration of ~ 50 fs is given after the compression stage. In the point of view of laser systems, the modal filtering is a successful system of beam spatial quality improvement. With respect to our purpose, the modal filtering is made to increase the harmonic phase matching and the harmonic beam quality. Since the filtered beam loses about 30% pulse energy compared to the non-filtered beam and the highly non-linear property of the HHG process, we are not sure whether this modal filtering can optimize the harmonic beam in our generating conditions. A campaign of HHG experiments has taken place to compare the harmonic flux and the spatial profile of the harmonic beam in far field with and without the modal filtering. Unfortunately, we didn't have the opportunity to do the complete measurements of the harmonic beam with a XUV wave front sensor as presented in the previous section. However the previous conclusion shows that when the harmonic flux and the beam coherence are optimized, the wave front is not far from optimization. A good compromise is then found for coherent imaging.

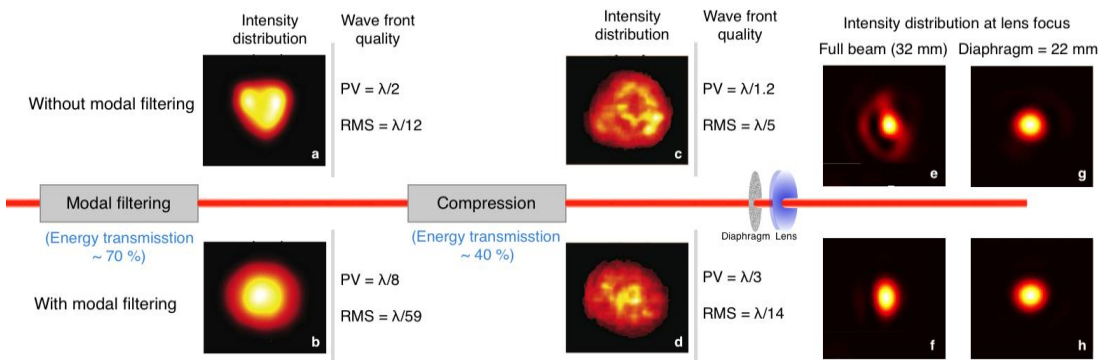


Fig. 2.13: Wave front measurements and simulations of the beam with and without modal filtering at different places on the beam path. Intensity distributions and wave front variations of the beam are presented for each position.

The HHG measurements with and without the modal filtering are realized in the “spectrum configuration” of the harmonic beamline (section II.1). A Toroidal mirror and a plane grating are located in the optics chamber. We use a thin slit and a photomultiplier tube (PMT) for the spectrum measurements and a CCD camera for the harmonic spatial profile measurements. The HHG optimization with modal filtering is realized using the same process as presented in the section II.3b. We are looking for a good compromise between harmonic flux and the spatial profile of the beam by varying different generating parameters, such as gas pressure, gas cell length, beam aperture, lens's focus position and IR pulse energy. Spectrum studies and optimization of HHG with Neon are presented here (similar studies have been also conducted in argon). The goal was to generate efficient harmonics around 20 nm to be applied for an application in single-shot imaging of cobalt magnetic nanodomains. As a result, the harmonic photon number generated in neon is increased by a factor ~ 4 when using the modal filtering.

Fig. 2.14 presents an example of the 37th harmonic generated in Neon with (a) and without (b) the modal filtering. With a beam aperture = 24 mm and a laser energy = 21.5 mJ, 2.9×10^6 photons/pulse are measured by the CCD camera with the modal filtering, instead of 0.8×10^6 photons/pulse without modal filtering and with a laser energy of 33.5 mJ. The harmonic flux ($\times 4$) and the HHG efficiency ($\times 6$) are both increased.

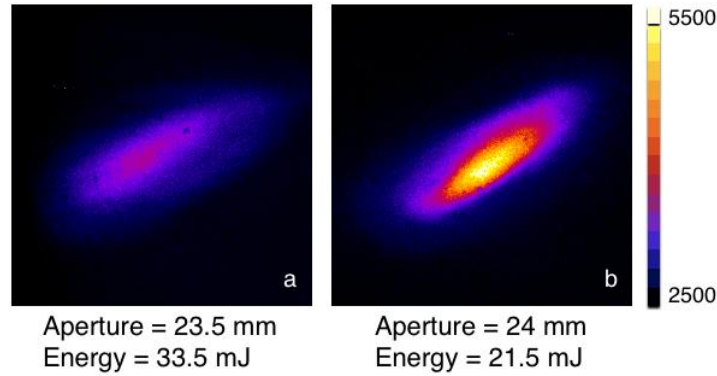


Fig. 2.14. 37th harmonic generated in Neon without (a) and with (b) the modal filtering in such conditions: lens's focus position is at 2 cm behind the gas cell output, gas pressure = 48 mbar and gas cell length = 7 cm. The measurements are in single-shot within a window of $3.37 \times 3.37 \text{ mm}^2$ detected by the CCD camera in the far field.

The modal filtering is a successful laser beam optimization system by filtering the laser modes with a high coupling efficiency. The filtered laser beam is quasi-mono-mode of EH_{11} , close to Gaussian beam, and is diffraction-limited before and after the pulse compression stage. Meanwhile, the pulse duration after compression remains comparative with non-filtered case. In the point of view of HHG, the modal filtering increases the harmonic conversion efficiency by a factor 6 in Neon. The harmonic flux is increased by a factor of 4 in Neon. Similar studies have been conducted in argon and we obtained an increase of a factor 2.5 in the conversion efficiency. However, it can be further improved in Argon but we had to cut off a large amount of laser energy to have a good spatial profile. To increase the harmonic flux in Argon with a proper spatial profile, we should change our experiment setup, for example, using a longer focal length lens (>5.65 m) to avoid too high laser intensity in the generating medium.

Another advantage of such device is the stability of the laser beam position on the focusing lens and inside the generating medium, which is important for a good alignment between the laser beam and the gas cell, and thus a stable HHG during a full day. The harmonic beam detected by the CCD camera is more stable in its spatial profile, intensity and position on the camera from shot to shot, compared to the case without modal filtering. We have observed a slow movement of the beam position in vertical direction after the output of the fiber, which is correlated to the working period of the air conditioner in the laser room. This slow movement is then corrected by a servomotor mounted on one plane mirror in the beam path before injection into the fiber.

II.5 Conclusion

In this chapter, the High flux harmonic beamline is presented with three main parts, the historical development, the optimization with XUV wave front sensor and the modal filtering device. The actual setup of the harmonic beamline for coherent imaging applications is presented in Fig. 2.16. The hollow-core fiber is installed between the amplification stage and the compression stage. The filtered beam is then focused into the gas cell by a lens of 5.65 m focal length. The harmonic beam is separated from the IR beam by an IR-antireflective mirror and an aluminum filter. A multilayer parabola selects one harmonic order and focuses it onto the sample located at the focus of the parabola. The CCD camera detects the diffraction pattern of the sample in far field. Note that, we have optimized the harmonic transmission of the beamline by using a high-tech aluminum filter (purchased from LUXEL Corp.) of 60% transmission for concerned wavelength in our case, compared to previous Al filter of 10% transmission (used in Ref. 11).

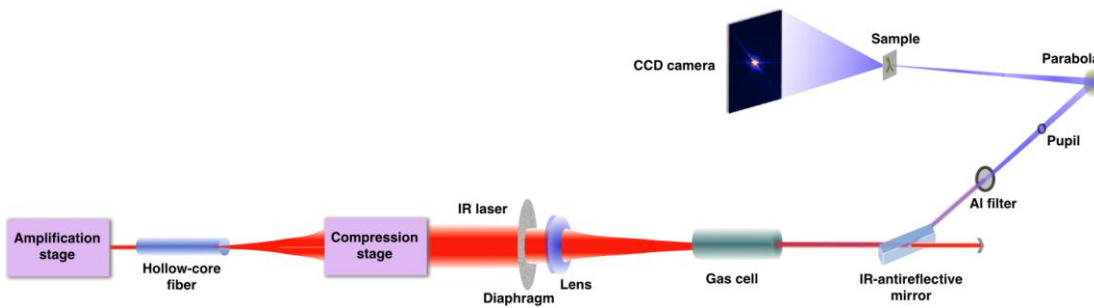


Fig. 2.16. Up-to-date setup of the High flux harmonic beamline for coherent imaging applications.

The High flux harmonic beamline is easy to switch to the spectrum configuration for other studies than coherent imaging. In both case, a μJ harmonic source (about 10^{11} photons per shot for 25th harmonic, $\lambda = 32$ nm) is generated at the output of the gas cell, with a wave front RMS of $\lambda/9$ before parabola and $\lambda/6$ after focusing, which is two times the diffraction-limited ($\lambda/14$). The combination of the intense harmonic flux and the good wave front quality promise high-quality diffraction pattern for coherent imaging. The campaign of harmonic wave front measurements result in an optimized HHG and a standardization of the beamline's daily operation conditions. Different generating parameters have been studied in this campaign. The finely adjusted parabola offers a focal spot size with a better quality and with a size well adapted to our imaging samples. The Young's double slits study has demonstrated a high coherent harmonic beam (fringe visibility more than 0.8 at the focus) and concludes that the harmonic flux, the wave front quality and the beam coherence can be optimized at the same generating condition. The modal filtering device provides a quasi-mono-mode laser beam for HHG and leads to improvement of the harmonic conversion efficiency. Even though we are actually not able to focus all the laser energy into Argon to generate much more harmonic photons than before,

some feasible modifications on the beamline (space needed) can potentially resolve the problem. Nevertheless, the harmonic flux in Neon is increased 6 times with the modal filtering. In both gases, the spatial profile of the harmonic beam in far field and the beam stability from shot to shot are better with the modal filtering. Fig. 2.17 is a typical spectrum of the HHG in Argon on the High flux harmonic beamline. The measured spectral width of the 25th harmonic (full width at half maximum) is 0.65 nm that the temporal coherence ($\Delta\lambda/\lambda$) is 0.02.

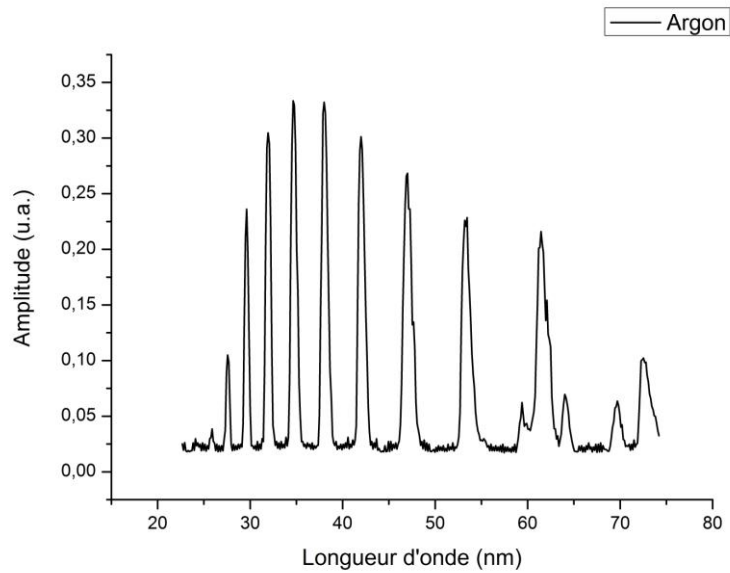


Fig. 2.17. The spectrum of the harmonics generated in Argon.

The harmonic beam used for coherent imaging in the Chapter III is summarized below:

Wavelength	32 nm
Pulse energy at the focus of the parabola	5×10^8 photons/pulse, ~ 3 nJ/pulse
Pulse duration	20 fs
Repetition rate	20 Hz
Intensity of the focal spot (5 μm diameter)	$\sim 10^{12}$ W/cm ²
Spatial coherence	> 0.8
Temporal coherence	0.02

Table 2.2. Summary of the harmonic beam's properties

This ultrafast and brilliant harmonic source promises high-resolution reconstructions of coherent imaging with a femtosecond time scale. The imaging experiments will be presented in the following chapter.

Even though our harmonic beam is 3 to 4 magnitude orders less than the beam delivered by the FEL facilities (for example, FLASH at Hamburg and LCLS at Stanford). Our beamline facilitates the experimental working conditions, with a relative easy control of the harmonic beam. The inexpensive cost and compact dimension of such beamline promises wider implementation in the world, thus much more beam time for various applications. Dynamic studies can be realized by a simple installation of a pump-probe setup.

Chapter III -Coherent Diffractive Imaging and Holographic imaging

III.1 Introduction

In this chapter, I present the demonstration of different coherent imaging techniques (CDI, HERALDO) using our high flux harmonic beamline. The diffraction experiments are accomplished after the wave front sensor HHG optimization (Chapter II, section II.3), and without the laser modal filter (which was added into the beamline later). CDI and HERALDO share the same experimental setup as described in Chapter II (Fig. 2.24 without modal filter). Typical image reconstructions in single-shot regime for CDI and HERALDO are respectively reported in Paper I and Paper III. The important aspects of coherent imaging, such as the beam's coherence, the signal-to-noise ratio of diffraction patterns, the comparison of different extended references in HERALDO, the comparison of CDI and HERALDO are also discussed here.

III.2 Sample preparation

All the test objects presented in this chapter have been fabricated using the focused ion beam (FIB) facility at the Centre de Spectromètre Nucléaire et de Spectrométrie de Masse (CSNSM, Orsay, France). The silicon nitride membranes are supported by silicon substrate on one side (Fig. 3.1), which defines the membranes aperture varying from $150 \times 150 \mu\text{m}^2$ to $500 \times 500 \mu\text{m}^2$. On such large window, we can fabricate more than 100 objects in one membrane. The thickness of the membranes varies from 50 nm to 150 nm to ensure that objects are two dimensional for our harmonic beam (Chapter I, section I.2b). Before etching, the membranes are covered by a gold layer (around 50 nm thick) whose transmission efficiency is less than 1.5×10^{-3} (Center of X-Ray Optics (CXRO) database) for the 25th harmonic (wavelength of 32 nm). This layer removes the direct beam and ensures that we have a pure transmission object for our imaging tests. Test objects are designed on 512×512 pixels bitmap files, which guide the focused ion beam [1] during the drilling process. The object definition is achieved with a precision of about 10 nm. The fabrication result can then be observed by scanning electron microscope (SEM) combined with the FIB (Fig. 3.2). The manipulation of FIB is delicate and one should respect strictly

the precautions and operation rules. For example, the alignment of the membrane with the focal plane of the ion beam and the choice of the parameters to tune the ion beam directly influence the fabrication quality.

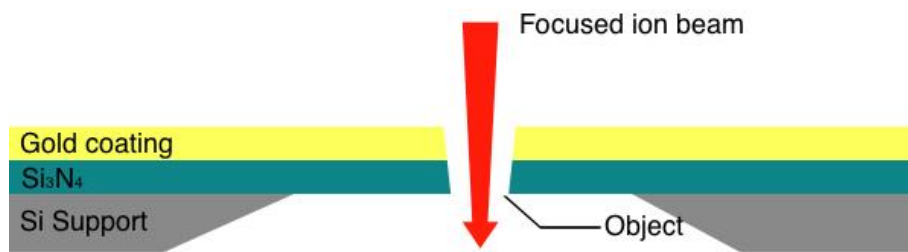


Fig. 3.1. Scheme of test objects fabrication.

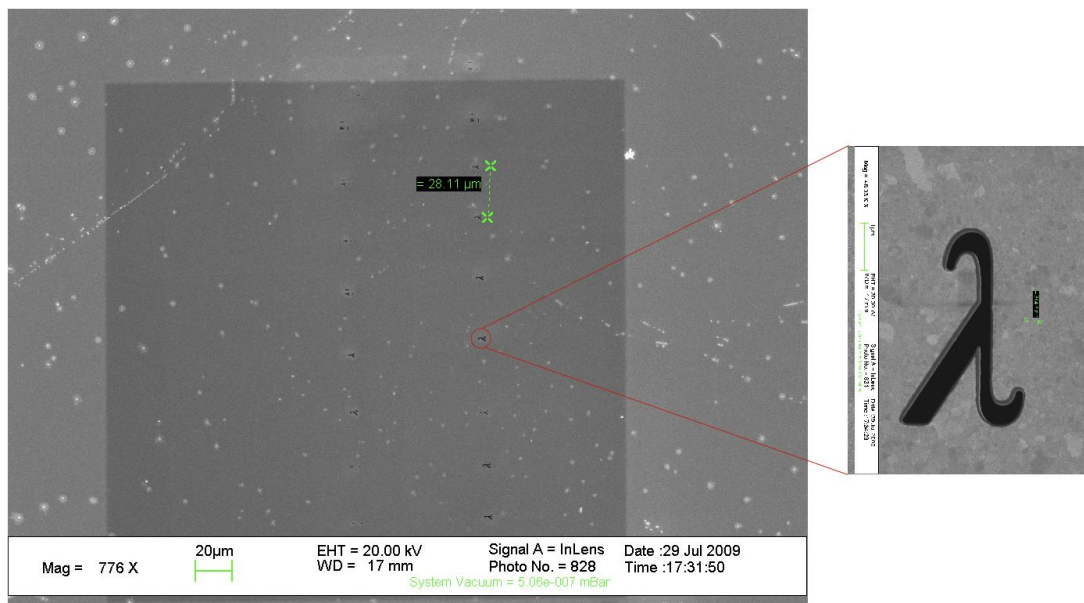


Fig. 3.2. Example of SEM image of a membrane's overview after FIB fabrication, with a zoom-in on one single object.

As mentioned previously, CDI requires an isolated object located in an extended vacuum space to fulfill the oversampling condition. In this case, the measured diffraction pattern is composed of the diffracted photons by the object and the direct beam, which is not blocked by the object. In our case, the test object acts as an opaque mask with a binary transmission. This means that the transmission of etched area is "1" and the membrane is "0". According to the Babinet's principle [2], the diffraction pattern from an opaque body is identical to that from a hole of the same size and shape except for the overall forward beam intensity. Therefore, our test objects can be considered as "conjugate" term of a real object, which would be well isolated. The

direct beam for such objects is composed of the transmitted photons of the membrane and the photons going through the object hole without diffraction, which usually presents as an intense spot in the center of the measured diffraction pattern. In FEL facilities, due to the high intensity of the pulse, the direct beam even in single-shot saturates the CCD camera so that one should place a beam stop to block it. However, the beam stop blocks also the low frequencies of the object diffraction. Since our harmonic beamline is less intense than a FEL, the beam stop is not necessary and the measured diffraction pattern contains all information. Note that even if our test objects used here are pure transmission object without phase modulation, CDI is also suitable for resolving objects presenting phase modulation (Chapter I, section I.2b).

III.3 Detection of the diffraction pattern

During the diffraction experiments, the first difficult task is to find the test objects. The objects (having a size smaller than $5 \times 5 \mu\text{m}^2$) are located in a membrane window of hundreds μm large, which is held by a sample holder with motorized translation stages. First without pumping, we use a HeNe laser, which is pre-aligned with the IR pump laser at a distance of $\sim 8 \text{ m}$, to find the membrane window position by checking the different transmission of the silicon nitride membrane and the silicone substrate. Then in vacuum, we use the harmonic beam to find the position of the membrane window's edges. Note that the translation stages of the sample holder used in this chapter provide a precision of $1 \mu\text{m}$, which has been upgraded to 1 nm during my thesis work (new sample holder used in Chapter IV). With the help of the SEM image (such as presented in Fig. 3.2), we scan over the possible regions containing objects with harmonic beam (size of $\sim 5 \times 5 \mu\text{m}^2$) to find one first object. Since the objects have been etched in a strict line frame, it is then easy to find other ones with a pre-calculation of the objects separation shown in SEM image. At last, we align the object with the harmonic focal spot in the beam propagation direction.

Considering the spectral range ($10 - 100 \text{ nm}$) explored during our experiments, we use a UV-X PI-MTE CCD camera fabricated by Princeton Instruments. It has a chip size of 2048×2048 pixels with a pixel size of $13.5 \times 13.5 \mu\text{m}^2$. The compact CCD camera (about 10 cm in the longest direction) can be located inside the experiment chamber and operates with a vacuum down to 10^{-7} mbar . It is then easy to motorize the CCD camera with translation stages. The camera can be cooled down to -40°C by water-cooling system to reduce the readout noise. The detection efficiency can be presented as:

$$I_{ADU} = \frac{\gamma_e Q}{G} N_{\text{photon}} \quad (\text{Eq. 3-1})$$

The intensity I_{ADU} of the diffraction pattern on each pixel corresponds to the analog-to-digital unit (ADU), which is the CCD's output count. The ADU (or the *count*) is linearly proportional to the incident photon number on each pixel (N_{photon}), and has a dynamic range from 0 to 65535 encoded on 16 bits. G is the system gain defines the relationship between the number of electrons acquired on a CCD and the ADU generated. Q is the quantum efficiency of the CCD camera presenting its probability to produce electrons from incident photons, N_{photon} . γ_e is the number of electrons generated by one incident photon, described as:

$$\gamma_e = \frac{\text{Photon Energy (eV)}}{3.65} \quad (\text{Eq. 3-2})$$

For the 25th harmonic beam (38.74 eV), 10 electrons are generated for one incident photon. For the 39th harmonic beam (60.45 eV) used in Chapter IV, 16 electrons are generated. The quantum efficiency is ~ 40% for the spectral range from 30 eV to 100 eV. The system gain is 1.3 electrons/ADU as designed and measured by the manufacturer. The relation can then be simplified to $I_{ADU} = 3N_{\text{photon}}$ for H25.

III.4 Implication of the spatial coherence in the CDI reconstructions

As presented in Chapter II, we have estimated the spatial coherence of our harmonic beam using Young's double slits (fabricated by FIB, Fig. 3.3a). The idea is to optimize the HHG for CDI with a good compensation between photon flux, wave front quality and beam coherence. Since the Young's double slits can also be considered as a CDI object, I have tried to reconstruct them using diffraction patterns (interferogram) taken under different HHG conditions (Fig. 3.3). This procedure will evaluate the sensibility of the CDI reconstruction process to the beam coherence. The double slits are 1.5 μm long and 300 nm wide, separated by 4 μm which is close to the size of the beam (about 5 μm). The measured diffraction photons in these single-shot detections range from 10^5 (Fig. 3.3b,c,g) to 10^6 (Fig. 3.3d-f). The spot in the center is the direct beam transmitted by the membrane, which does not influence significantly the CDI reconstruction process.

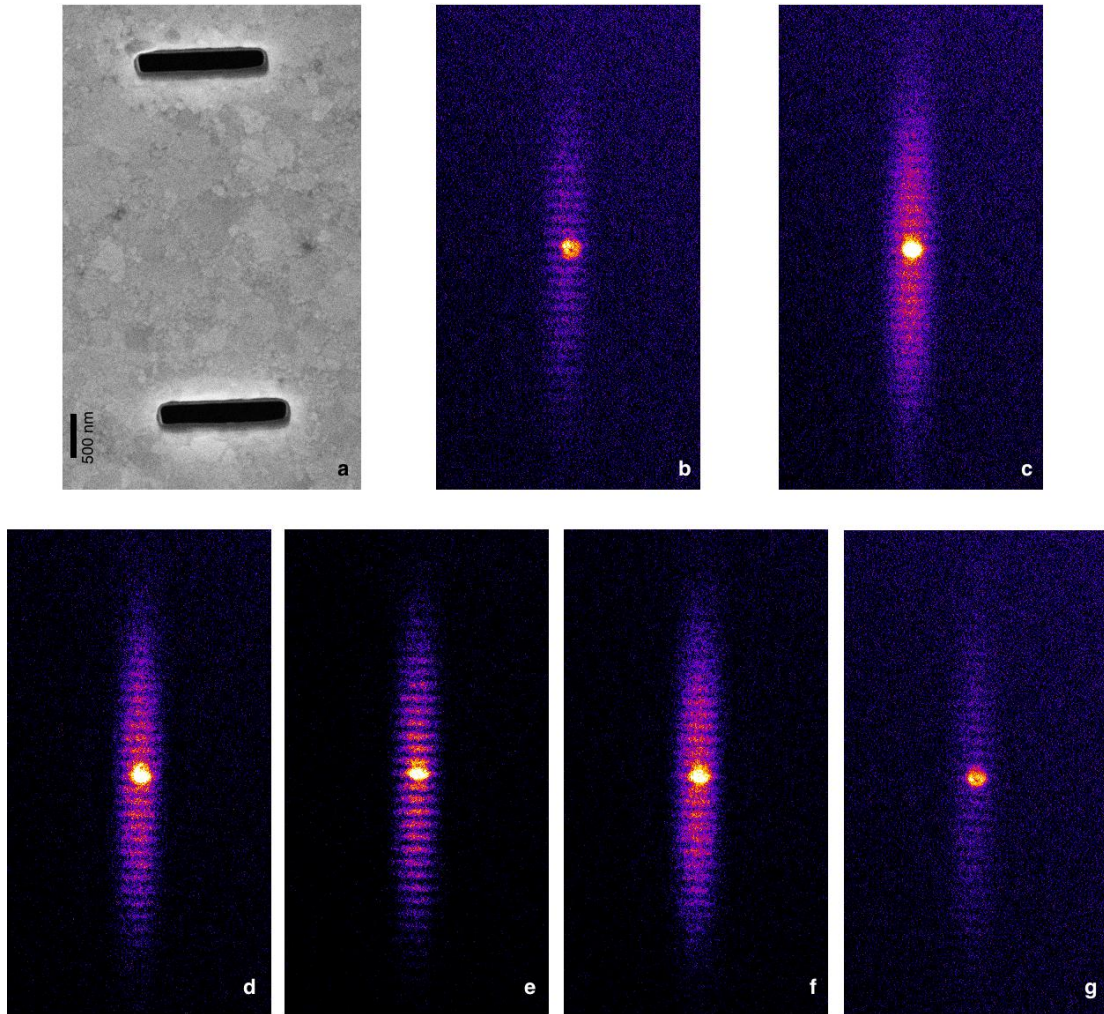


Fig. 3.3. (a) SEM image of the Young's double slits. (b) to (g) typical fringes measurements corresponding to different HHG conditions presented in Fig. 2.19. The gas pressure varies from 11 mbar (b) to 16 mbar (g). All fringes are measured with a window size of 800 x 800 pixels. Here they are cropped for a better presentation.

A reconstruction of the double slits has been possible only in certain cases. In the case of poor visibility combined with poor intensity (such as Fig. 3.3g), the iterative process cannot converge. Good reconstructions are achieved for HHG conditions combining both intensity and visibility optimization (such as Fig. 3.3c-e). Reconstructions are less good for fringes with a visibility around 0.5 (such as Fig. 3.3b and f), even for fringes with maximized diffraction photons (such as Fig. 3.3f). The reconstruction with best resolution (138 nm) is presented in Fig. 3 of Paper I. Here, Fig. 3.4 presents the two reconstructions for Fig. 3.3c and d, corresponding to a fringe visibility respectively 0.6 and 0.67, and the measured diffraction intensity of Fig. 3.3d is about 1.3 times higher than the other. Note that Fig. 3.3f has similar diffraction intensity as Fig. 3.3d, but a poor fringe visibility of ~ 0.5 makes the iterative algorithm not able to identify the two slits. For all slits reconstructions, the initial support is calculated by the Fourier transform of the measured diffraction

pattern, which corresponds to the autocorrelation of the double slits (Fig. 3.5). If the beam is totally coherent, based on the definition of the autocorrelation, the ratio between the maximums of the center part (green circle) and the side part (red circle) should be equal to 2. This ratio is directly related to the beam coherence, which becomes smaller when the coherence is limited. During the iterative process, the support is refined (reduced in space) for each iteration with a threshold, usually defined by its intensity distribution. Thus, for fringes with limited coherence, the side parts will have a weak intensity. In such case, the information will be eliminated by the threshold, which is set to avoid any unreliable reconstruction. In such case we usually obtain only one slit reconstruction, the second slit being missed by the artificially truncated support used in the algorithm. This is a standard problem in CDI when using a symmetric object. CDI applies better for non-symmetric objects as the support ambiguity is removed.

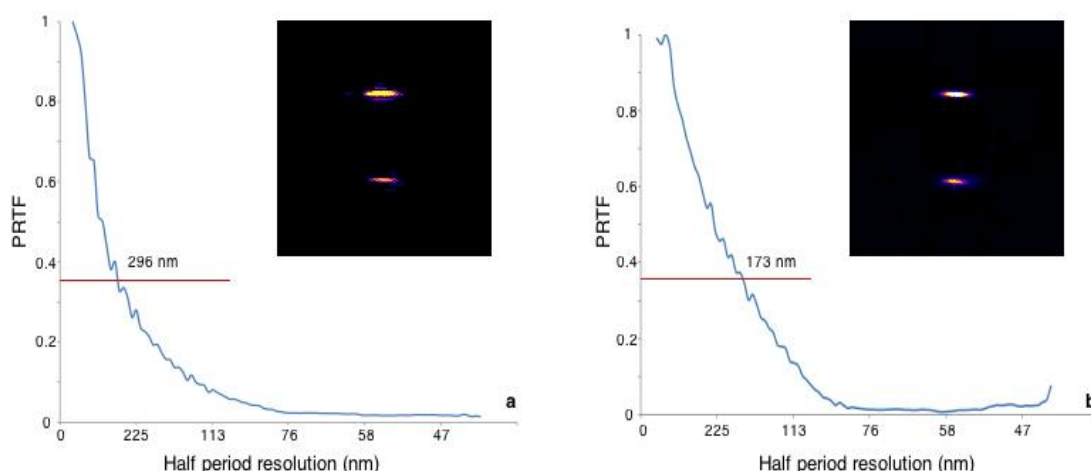


Fig. 3.4. (a) and (b) are respectively the reconstructions of Fig. 3.3c,e. The resolution estimated is 296 nm and 173 nm.

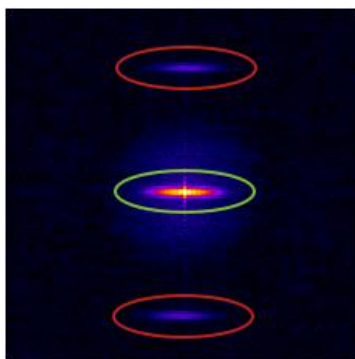


Fig. 3.5. Autocorrelation of the Young's double slits, calculated from a measured diffraction

pattern.

We estimate the reconstruction resolution in CDI using the phase retrieval transfer function (PRTF), which is the ratio between the absolute value of the Fourier transform of the reconstruction and the square root the measured diffraction intensity:

$$PRTF(v) = \frac{|\mathcal{F}\{Reconstruction\}|}{\sqrt{I_{Diffraction\ pattern}}} \quad (\text{Eq. 3-3})$$

The resolution is given at the ratio of $1/e$, according to the PRTF criterion [3]. v is the spatial frequency of the diffraction pattern, equal to $D/\lambda z$, where D is the distance of the concerned pixel to the center of the diffraction pattern, and z is the distance between the detection plane and the object plane.

III.5 Experimental results of CDI

After the beamline optimization, we have performed CDI experiments using texts objects, such as the “lambda” presented in Paper I. We have been able to reconstruct the “lambda” ($3.2 \mu\text{m} \times 2 \mu\text{m}$) from a single-shot acquisition (20 fs pulse duration) with a spatial resolution of 78 nm (equal to 2.5λ), which is largely improved compared to the 119 nm reported in A. Ravasio *et al.* [4], which was realized with a non-optimized beam and focus. The object “note” ($3 \mu\text{m} \times 2.8 \mu\text{m}$) in the latter has been retested and we got a single-shot reconstruction with 75 nm spatial resolution, which is close to the 40-shot reconstruction reported in previous work. The final reconstruction presented in Fig 3.6 is an average of 14 best different reconstructions output after 1000 iterations of the RAAR algorithm. The original diffraction pattern is recorded in a window size of 2048×2048 pixels. It is cut into a size of 848×848 pixels and then binning 4×4 (16 pixels integrated into one large pixel) for the reconstruction to accelerate the algorithm calculation. Thus, each pixel of the reconstruction has a size of 53 nm (p_{object}), calculated by following equation:

$$p_{object} = \frac{\lambda z}{N_{pixel} p_{camera}} \quad (\text{Eq. 3-4})$$

where N_{pixel} is the number of pixels of the window size and p_{camera} is the pixel size of the camera. Note that, the oversampling ratio for these CDI objects is about 10, thus

the 4×4 binning still qualifies for the oversampling condition. The improvement of the reconstruction quality is mainly due to the increased photon flux. Indeed, we have detected a few 10^7 diffracted photons in the single-shot measurements of “lambda” and “note”, compared to 5×10^5 photons in the previous work. Since there is no measurement of the beam’s wave front and coherence in the former experiment, the comparison on these aspects is not possible. Note that the relative poor reconstruction quality of Young’s double slits (with good coherence) is due to the lack of diffracted photons ($\sim 10^6$ photons are detected in the best case). The low diffraction efficiency is caused by the geometry of the double slits, which are situated at the edges of the beam when well aligned. On the contrary, our test objects are perfectly aligned with the more intense part of the soft X-ray focused beam.

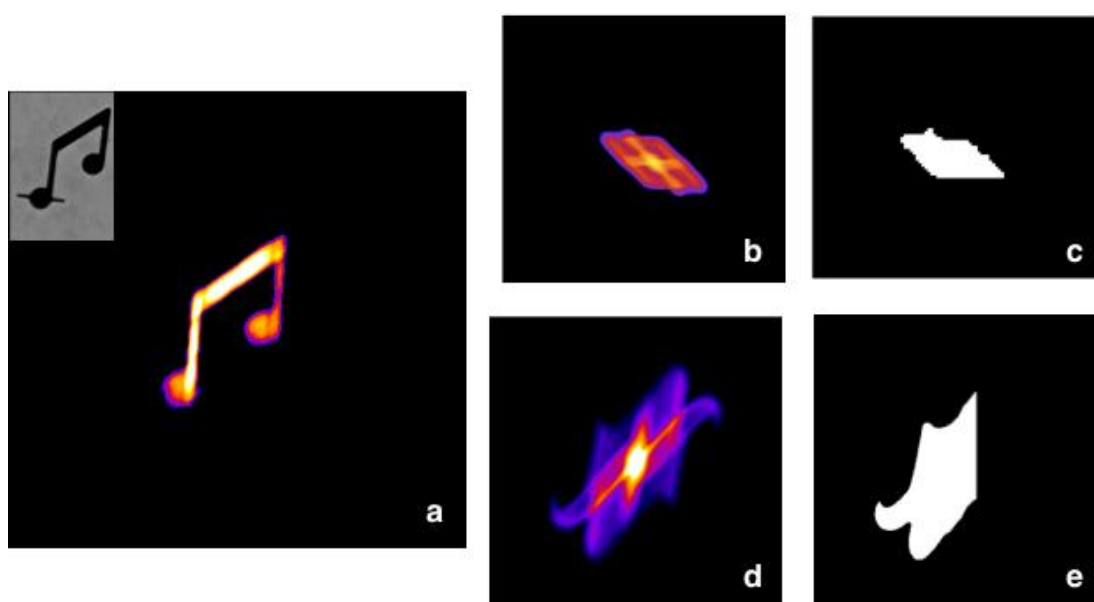


Fig. 3.6. (a) The “note” reconstruction in single-shot detection with a presentation of its SEM image. The missing slit is due to the radiation damage after long time exposure. The radiation damage is an important constraint on FEL facilities, especially for biological samples. Discussions have arisen on this subject [5,6]. (b) and (d) are respectively the autocorrelation for “note” and “lambda”. During the iterations, the reconstruction of the object can flip horizontally or vertically due to the symmetry of the autocorrelation. Thus non-symmetry masks (c and e) are applied to the autocorrelation when calculating the support to avoid the flip.

In fact, the object geometry is another important factor for the CDI reconstruction, beside the three-coupled factors of the harmonic beam (wave front, coherence and photon flux). For example, “note” and “lambda” are simple objects that present in general two main directions of diffraction. Compared to objects that have diffraction signals extended in all directions (such as the Airy disk of a circle), the diffraction pattern of objects like “note” and “lambda” will have higher photons/pixel values, as

the photons are mainly located in the main diffraction axes. Thus better signal-to-noise ratio and higher spatial frequencies are obtained for the reconstruction under the same illumination condition. Fig. 3.7 illustrates the importance of the object geometry for CDI with comparison between objects “note” and “phos”. The latter is composed of 3 Greek letters with a total size of $3.2 \mu\text{m} \times 2.5 \mu\text{m}$. The red rectangles in the diffraction patterns show the spatial extension of the diffracted signal: 1100×850 pixels for “note” and 460×460 pixels for “phos”. The maximum spatial frequencies of the diffracted photons are $\pm 12.2 \mu\text{m}^{-1}$ and $\pm 9.4 \mu\text{m}^{-1}$ for “note”, and $\pm 5.1 \mu\text{m}^{-1}$ for “phos”. The theoretical resolution is then limited to 53 nm for “note” and 98 nm for “phos”. However, the measured diffracted photons are the same: 2.8×10^7 for “note” and 2.7×10^7 for “phos”. The reconstruction of “phos” is not satisfying: only the “ ω ” is resolved while the other two letters are partially or non-resolved at all. Since the objects have similar size, the poor reconstruction should not be related to illumination problem or coherence problem. The object geometry could be therefore a constraint for single-shot CDI experiments at our harmonic beamline. In multiple-shot regime, we are able to accumulate enough signals to have sufficient spatial extension of the diffraction pattern for high-resolution reconstructions, as demonstrated in previous work of A. Ravasio *et al.*. The other method to amplify the diffraction signal is to use extended reference, which still keeps the possibility of high-resolution reconstruction (section III.10).

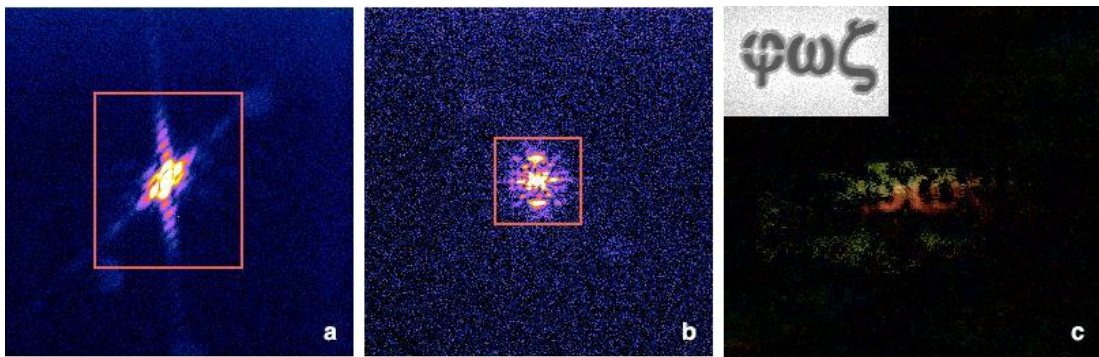


Fig. 3.7. (a) and (b) Diffraction patterns of “note” and “phos”, displayed with the same color scale. The red rectangles present the extension of the diffracted signals. Images are taken with a window size of 2048×2048 pixels. The two half-circle at the edge of the red rectangle in (a) are parasite signals. (c) is a typical reconstruction after 2000 iterations of object “phos”. The SEM image of “phos” is on the top corner.

We have tested another object “Eiffel tower” (Fig. 3.8a), which has a size of $5 \mu\text{m} \times 4 \mu\text{m}$ and is more complex than “note” and “lambda”. The single-shot diffraction pattern presented here has three main diffraction directions and is more “homogeneous” than “note” and “lambda” with signal extension size of 800×800 pixels. The maximum spatial frequency is $\pm 8.88 \mu\text{m}^{-1}$, corresponding to a theoretical

resolution (Chapter I, section I.2c) of 56 nm. The calculated autocorrelation (Fig. 3.8b) shows a high agreement with the simulation (Fig. 3.8c). Thanks to the presence of the star beside the tower, which acts like a holographic reference in the autocorrelation calculation, we can clearly identify the Eiffel tower in the autocorrelation. However no FTH or HERLADO reconstructions can be processed, except that applying a particular de-convolution operator well adapted to the star shape on the autocorrelation may probably lead to reliable reconstruction. Fig. 3.8d is the CDI reconstruction of the single-shot diffraction pattern after 3000 iterations, compared to the reconstructions of 400-shots (Fig. 3.8e) accumulation taken before the harmonic beamline optimization. The single-shot reconstruction presents a lack of illumination on the top and the bottom part of the tower, which can also be observed in the autocorrelation. The star is blurred which could be related to the radiation damage suffered by the object during long time exposure. Due to the instability of the beam before optimization, the reconstruction of the multi-shot detection does not show significant improvement, but is in fact more blurred. However, the accumulated illumination provides more photons and thus a “clearer” vision over the entire object.

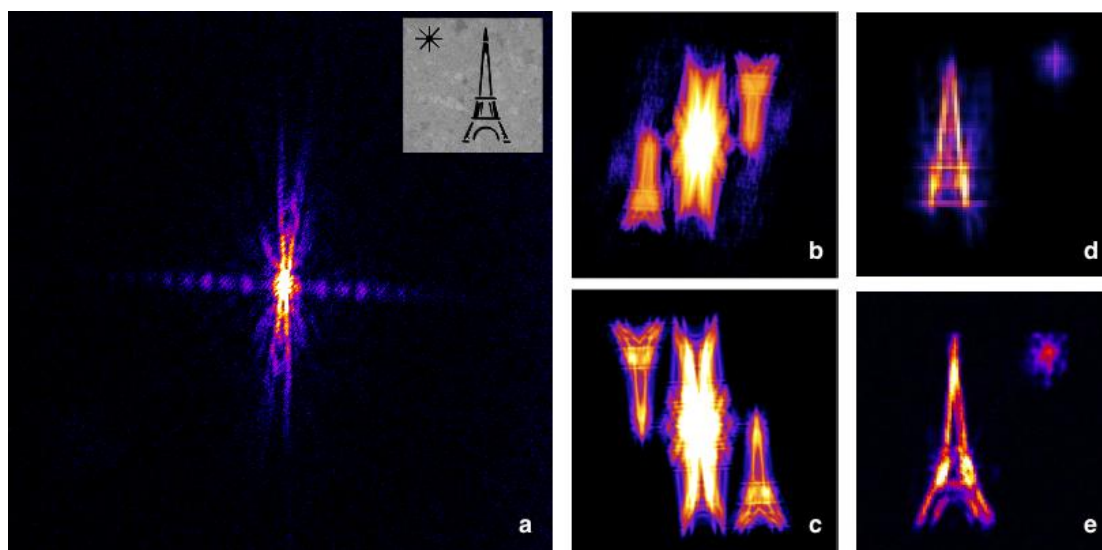


Fig. 3.8. (a) Single-shot detection of the “Eiffel tower” object with its SEM image on the top. (b) Autocorrelation calculated from (a), compared to the numerical simulation of the SEM image (c). (d) Reconstruction of single-shot detection with a spatial resolution of about 110 nm. (e) Reconstruction of 400-shots detection obtained before the harmonic beamline optimization. The reconstruction has been realized by Pierre Thibault (Cornell Univ. and now TU Munchen).

III.6 Experimental results of Fourier Transform Holography

We have prepared two test objects to perform Fourier Transform Holography (FTH) experiments. Object “h” has a size of $\sim 1.6 \mu\text{m} \times 2.4 \mu\text{m}$ and the other is a “geometry grid” object with a size of $1 \mu\text{m} \times 1 \mu\text{m}$ (Fig. 3.9). For each test object, we have etched two identical reference pinholes in vertical and horizontal directions. Different pinhole sizes have been combined to the objects: 300 nm or 240 nm (diameter) for “h”; 110 nm or 145 nm for “geometry grid”. The FTH experiment will be then confronted to the HERALDO technique using different extended references. The comparison of these two techniques is discussed in Paper IV. Here, I would like to show some complementary experimental results that are not presented in the manuscript.

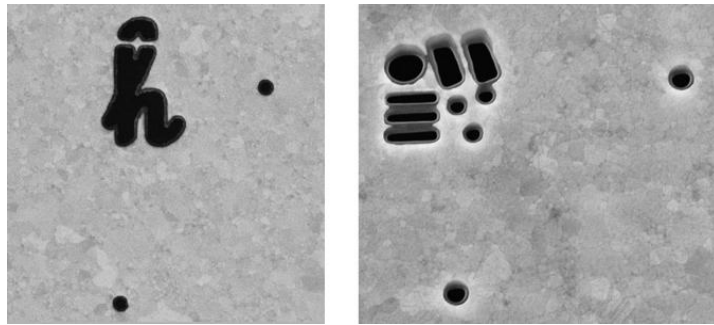


Fig. 3.9. SEM images of holographic objects “h” and “geometry grid”.

The “h” object can be constructed from single-shot detection as shown in Fig. 3.10. The diffraction pattern is recorded in a window size of 2048×2048 pixels with a signal extension of $\sim 350 \times 350$ pixels, corresponding to a maximum spatial frequency of $3.89 \mu\text{m}^{-1}$. The hologram contains $\sim 7 \times 10^6$ photons and presents no privilege diffraction directions and contains the full speckles that encodes the phase information. Applying a Fourier transform on the hologram, we get the two pairs of reconstructions associated to the two pinholes references. Note that there are only two independent reconstructions in this case, since the reconstructions in opposite positions are the complex conjugates. In the case of Fig. 3.10, the images obtained with the vertical pinhole are much intense than the ones by the horizontal pinhole. This is due to a misalignment between the object (including the references) and the harmonic beam. To estimate the spatial resolution, I plot the profile of the reconstruction along the white line (Fig. 3.10). This allows us to visualize the noise and the sharpness of the object edges. According to the 10%-90% Rayleigh criterion, the resolution is estimated to be around 220 nm, which is close to the resolution limitation defined by the pinhole size of 300 nm. A low-pass filter (Gaussian filter) has then been applied on the hologram to knock out the noise in high frequencies where no diffractive signals are recorded. The width of the Gaussian filter is chosen to adapt the maximum diffraction extension and the filtered hologram is presented in Fig. 3.10b. The reconstruction of the filtered hologram highly agrees with the non-

filtered one. The profile plotted at the same position is the smooth “version” of the previous one, which is the convolution between the noised profile and the Gaussian filter. The two profiles have same contrast of ~ 0.64 . In the case of FTH, the low-pass filter only leads to a more comfortable vision of the reconstruction, the spatial resolution being the same. But in the case of HERALDO of two-dimensional references, the low-pass filter is essential for the reconstruction (section III.9). However, in all cases, it imposes a resolution limit related to the filter width.

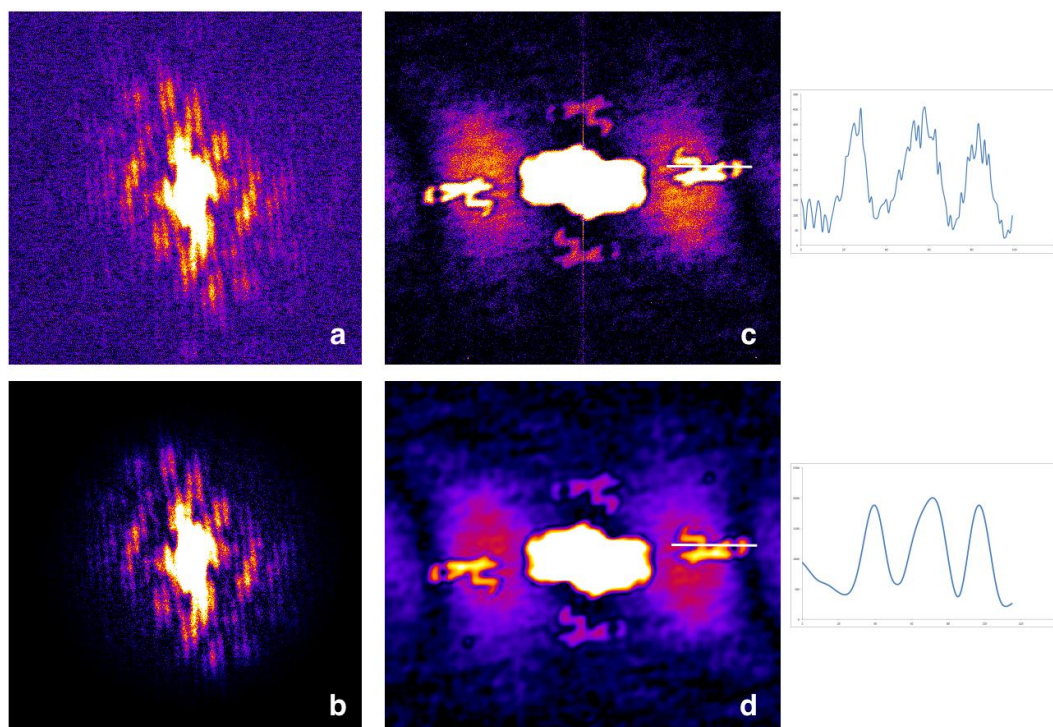


Fig. 3.10. (a) A zoom-in (400 x 400 pixels) of the original single-shot detection (2048 x 2048 pixels) of “h” object with pinholes of 300 nm. (c) Reconstructions from the original data, with the profile plotted at the white line position. (b) Hologram filtered by a low-pass filter with respect to the diffraction signal extension. (d) Reconstructions of the filtered data, which presents the same profile as the previous one.

The “geometry grid” is also reconstructed from single-shot measurement (Fig. 3.11b). The measured diffraction photons is $\sim 2 \times 10^6$ that is less than the “h” diffraction due to the smaller object size and smaller pinholes. The diffraction pattern (Fig. 3.11a) is recorded with a binning ratio of 2 (4 pixels integrated into a large one). The signal extension of 320 x 200 “large” pixels (thus, 640 x 400 normal pixels) corresponds to maximum spatial frequencies of $7.1 \mu\text{m}^{-1}$ and $4.4 \mu\text{m}^{-1}$ respectively. A low-pass filter has been applied onto the hologram to have a better vision of the reconstruction. All the components of the grid are well reconstructed (Fig. 3.11c). The profiles in vertical and horizontal directions show a contrast of ~ 0.6 . Note that the tree horizontal slits have a width of 95 nm and are separated at a center-to-center distance of 95 nm. Fig.

3.11d is another single-shot diffraction pattern obtained for the same object which contains $\sim 3.2 \times 10^6$ diffracted photons, higher than Fig. 3.11a. However, we cannot observe fringes in the speckles in Fig. 3.11d, compared to the clear interference signature in Fig. 3.11a. The lack of interference fringes leads to worse reconstruction quality so that the components of the grid are “missed” in the reconstructions (Fig. 3.11e). The zoom-in of the two independent reconstructions shows that the big circle and the three small holes are not resolved in different reconstructions. Moreover, the other components are also less resolved, compared to Fig. 3.11c. We can obtain the “missed” components by averaging coherently (complex value calculation) the two independent reconstructions, as shown in Fig. 3.11f. However, the final reconstruction present a contrast of ~ 0.4 in vertical and horizontal profiles, which demonstrates a worse resolution compared to that in Fig. 3.11c. The lack of interference fringes should be related to a coherence problem of the harmonic beam for this acquisition. Note that these two diffraction patterns were taken before the modal spatial filter upgrade of the harmonic beam (Chapter II, section II.4). Indeed, the statistics over ten single-shot acquisitions recorded consecutively for the same object show a total of three holograms lacking of interferences. Still, the stability was enough for the data recorded during this campaign. The comparison here demonstrates the importance of the balance between the photon flux and the beam coherence in coherent imaging. A relatively less intense beam but with a higher coherence can lead to a better reconstruction quality than a more intense beam with less coherence.

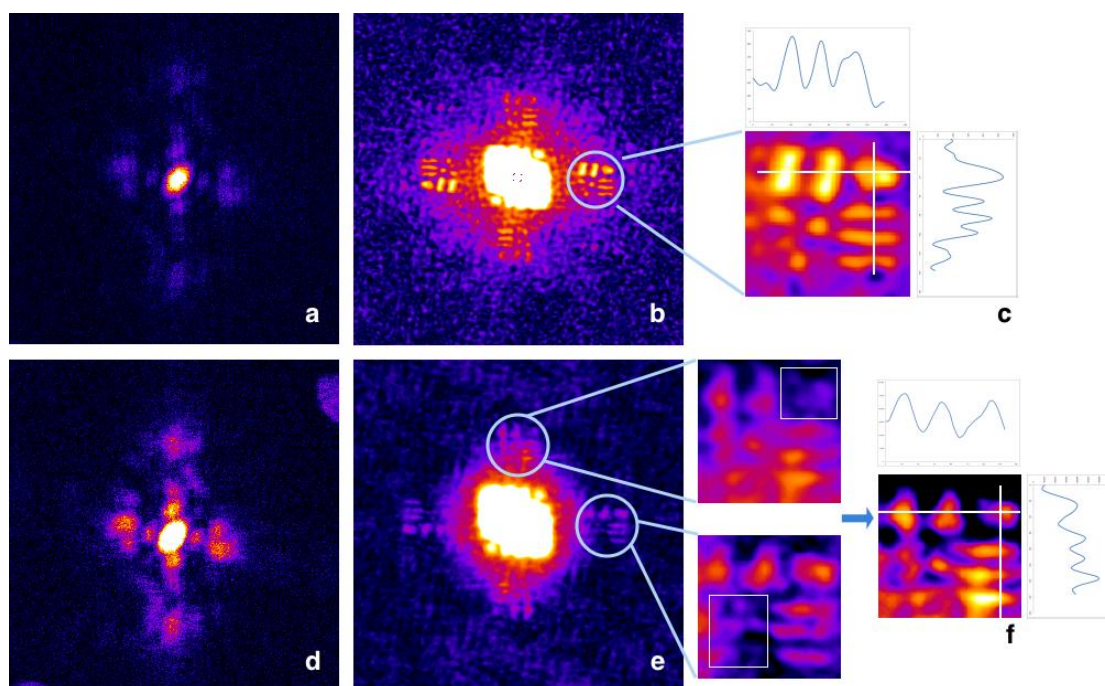


Fig. 3.11. (a) A zoom-in (400 x 400 pixels) of the single-shot acquisition (600 x 600 pixels) with clear interference fringes of test object “geometry grid”. (b) Reconstructions of (a) and

its zoom-in (c). (d) A zoom-in (300 x 300 pixels) of the single-shot acquisition (682 x 682 pixels) of the same object, with a higher diffraction signal and a lack of interference fringes. The signals at the top and bottom corners are parasite light. (e) Reconstructions of (d) with non-resolved components of the object. (f) The final reconstruction by coherent averaging of the two independent reconstructions in (e).

III.7 Experimental results of holography with extended reference

Holography with extended references (HERALDO) has been tested with a linear slit reference. In this configuration, the reconstruction resolution is limited by the slit width in the direction perpendicular to the slit orientation. By applying a linear differential operator along the slit reference shown in Fig. 3.12, we get two Dirac functions that are similar to the pinhole reference in FTH at its extremities (Fig. 3.12b). The holographic separation condition requires that our test object (letter “ ϕ ”) should be separated from the reference slits at a distance at least equal to two times the object size (Fig. 3.12d). The object “ ϕ ” covers an area of $2 \mu\text{m} \times 1.7 \mu\text{m}$ and the slit width is 130 nm and 145 nm respectively for horizontal and vertical one with a length slightly longer than the object. The total object and references are within a window size of $4.5 \mu\text{m} \times 4.5 \mu\text{m}$.

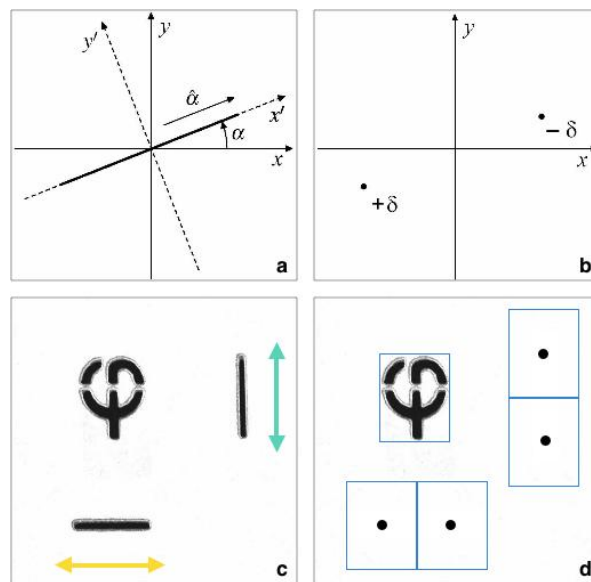


Fig. 3.12.(a) Applying linear differential operator ($\hat{\alpha}$) on slit reference (at angle α) leads to two Dirac functions (b) at the extremities of the slit. (c) The test object “ ϕ ” with two slit references. (d) The slits’ length and the distance to the object are chosen to satisfy the holographic separation condition. There should be no recovery between the blue rectangles, which is the object size.

Fig. 3.13 show both single-shot and multiple-shot acquisitions of the HERALDO holograms. In Fig.3.14, we see that by applying a linear differential in each direction given by the slits to the autocorrelation of the hologram (a) we get four independent reconstructions (b,c). They can be averaged to enhance the reconstruction quality. The single-shot reconstructions are shown in Fig. 2 and 3 in Paper III. The estimated resolution is 110 nm, corresponding to a spatial frequency of $4.55 \mu\text{m}^{-1}$, while the multiple-shot (10 shots) reconstructions have a resolution of 80 nm (corresponding to $6.25 \mu\text{m}^{-1}$ spatial frequency, red circle in Fig. 3.13b), which is limited by the width of the slit reference. However, the signal extension in multiple-shot (yellow circle in Fig. 3.13b) is much larger than the limit given by the spatial resolution of the recovered image. Indeed, in the reconstruction process, the spatial resolution is limited by the manufactured size and quality of the references. It is possible to estimate this limit by applying a linear differential operator to the slits presented in the high resolution SEM image (Fig. 3.15). The particular shape of the calculation result is our reference. The deviation from a perfect pinhole (or a Dirac function) will affect the final reconstruction resolution. In the case of a slit reference, the resolution limit is not uniform for all orientations. The longest side of the “point source” imposes a resolution limitation of ~ 85 nm, which agrees with the estimated reconstruction resolution.

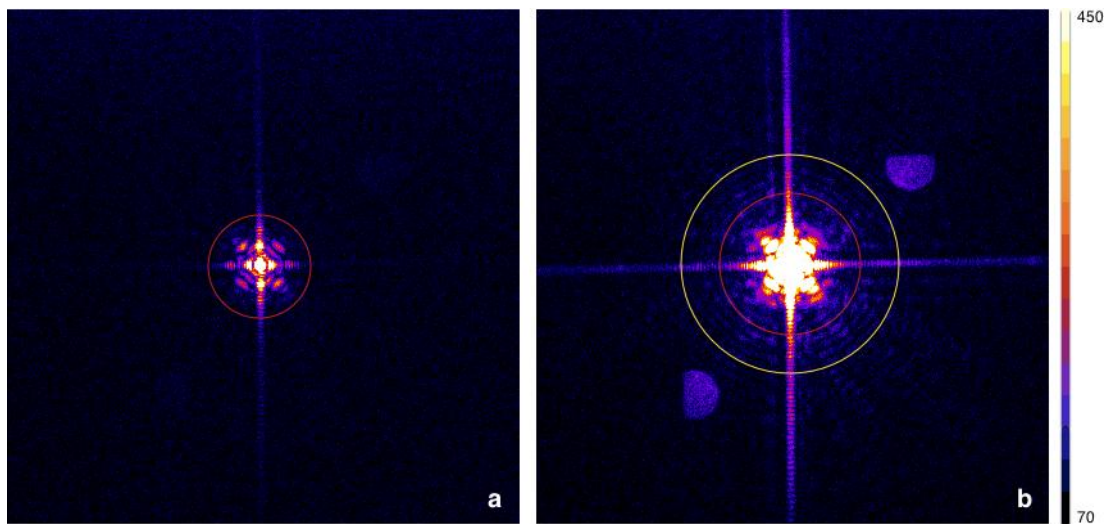


Fig. 3.13. (a) Single-shot diffraction pattern of the HERALDO object “ ϕ ”. (b) 10-shot diffraction pattern of the same object presented in the same color scale. The signals of two half-circle outside the yellow circle are parasite light. Red circles shows the spatial frequencies corresponding to the estimated reconstruction resolutions. The yellow circle shows the signal extension given by the resolution limit.

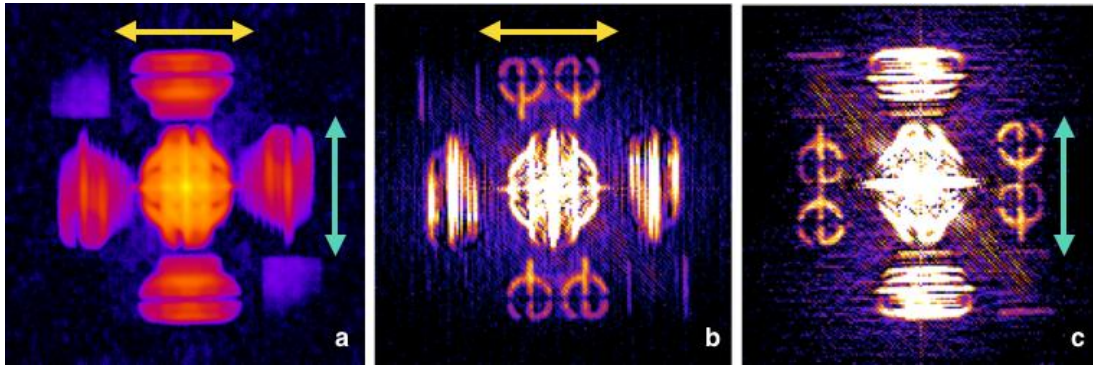


Fig. 3.14. (a) Autocorrelation for the 10-shot acquisition hologram. (b) is the derivation along the horizontal slit (yellow arrow) of the autocorrelation (a). (c) is the derivation along the vertical slit (green arrow) of the autocorrelation (a). Each reconstruction (b) and (c) shows two independent reconstructions. The crossed terms between the object and the reference show already the shape of “ ϕ ”. The crossed term between the two references (the square at left top and right bottom) shows that the illumination is not uniform for the entire sample. This can also be observed in the reconstructions (b, c) where the object “ ϕ ” is more intense in the inner part.

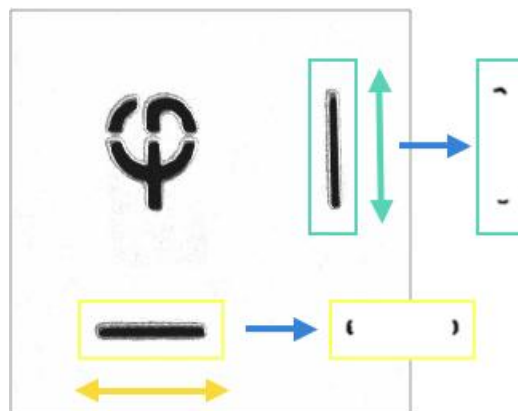


Fig. 3.15. SEM image of the sample. The derivations of the slits are shown in the rectangles at the right of the blue arrow. They exhibit four moon shape patterns, which are the deviation from an equivalent “point source” of the slit references simulated from the SEM image by applying linear differential operator. The green square is the result of vertical linear differential operator, and the yellow square is the horizontal one.

III.8 Signal-to-noise ratio (SNR) analysis

For all the three imaging configurations (CDI, FTH, HERALDO), the signal-to-noise ratio is a key factor for the reconstruction quality. In our experimental conditions, the noise can be separated into four independent components according to their nature:

- 1) The parasite light noise: as shown in the measured diffraction patterns, we have sometimes detected parasite light signals, usually at the outer part of the diffraction pattern (Fig. 3.13b). It is due to the IR and/or harmonic reflections inside the experimental chamber, and/or the transmission of the parasite light through the sample holder.
- 2) The photon noise: it is directly related to the diffraction signal and obeys to the Poisson distribution. The signal-to-noise ratio can be described as $SNR = \frac{N}{\sqrt{N}} = \sqrt{N}$, where N is the photon flux (or photon numbers).
- 3) The readout noise: it is related to the CCD camera readout quality, which is the uncertainty introduced during the process of quantifying the electronic signal. The readout noise mainly arises from the on-chip preamplifier [7]. It is characterized by its standard deviation $\sigma_{readout}$ (or its variance $\sigma_{readout}^2$).
- 4) The dark noise (dark current): it is introduced by the thermally generated electrons within the silicon layers of the CCD. The dark current describes the statistical variation of the thermal electrons at a given CCD temperature and a given exposure duration, obeying also to the Poisson law. It is characterized by electrons/pixel/sec.

Practically, the noise reduction has been realized at the detection stage through several steps. The parasite light noise can be easily removed after detection, since it is usually located in the region without diffraction signal in our experiment. We have also added light shields and filters (as what we did for magnetism experiments in Chapter IV) to stop the parasite light before detection. We cannot reduce the photon noise due to its nature, but we can increase the associated SNR by increasing the total photon number (beamline output, light transport and focus optimization) because of the square root relation of the photon noise SNR. One can also bring the CCD camera closer to the object plane to have a higher photons/pixel ratio to enhance the SNR associated to the photon noise. Note that, the CCD-object distance should always fulfill the sampling ratio for FTH/HERALDO or the oversampling condition for CDI. Moreover, multiple-shot accumulation can also enhance the SNR. The dark noise can be reduced by cooling down the CCD camera, which is 0.05 electrons/pixel during 100 seconds exposure at -40°C, according to the CCD camera fabricant. The readout noise depends on the readout frequency of the camera. Our CCD camera has two available readout frequencies: 1 MHz and 100 kHz. The reference value (standard deviation) given by the CCD camera fabricant is 8.8 electrons for 1 MHz and 4 electrons for 100 kHz, corresponding respectively to 6.8 ADU and 3.1 ADU. The disadvantage of using 100 kHz is the long CCD readout time, which is up to 30 seconds, compared to the 4.5 seconds for 1 MHz. Note that the readout time depends on the CCD chip size (or total pixel numbers). The CCD camera offers an option to read only a part of the CCD chip defined by users (called region of interest) to reduce

the readout time. In practice, according to the measurement in dark condition (Fig. 3.16), the measured readout noise for 1 MHz and 100 kHz is respectively 9.2 ADU and 3.2 ADU, thus ~ 12 electrons and ~ 4 electrons. The other option provided by the CCD camera to enhance the readout SNR is the hardware binning, which combines charge from adjacent pixels into a single large pixel during the readout process. In the ideal case, the enhancement is equal to the binning ratio. For example, if each normal (non-binning) pixel has signal of 20 electrons and a readout noise of 10 electrons, then a single large pixel of 3×3 binning ratio will have a signal of 180 electrons and a readout noise of 10 electrons (it is introduced only once during the readout process). The SNR of a large pixel is then 9 times larger than that of a basic pixel unit. Note that the *hardware* binning is different to the *software* (or *numerical*) binning, which combines adjacent pixels after the readout process, thus the software binning does not change the SNR associated to the readout noise, but still increases the SNR of photon noise for each large pixel. One should again be careful of the sampling ratio when binning the pixels. The measured diffraction pattern is the superposition of the diffracted signal and the different noises, among which the dark noise and the parasite light noise are easy to handle. Usually, with a low diffraction signal, the noise is dominated by the readout noise, which is called readout-noise limited; with a high diffraction signal, the photon noise is dominant, which is called photon-limited. For the wavelength used in our imaging experiment (H25, 32 nm), one detected photon generates 10 electrons (Eq. 3-2), which is comparable to the readout noise at 1MHz. In our experiment, the measured diffraction patterns are mainly influenced by the readout noise and the photon noise. The SNR of the diffraction pattern is then

$$SNR_{diffraction\ pattern} = \frac{N_{detected\ signal}}{\sqrt{N_{detected\ signal} + \sigma_{readout}^2}} \quad (\text{Eq. 3-5})$$

Overall, we distinguish in our diffraction patterns two regions: the region of low spatial frequencies is photon limited and the region of high spatial frequencies is readout-noise limited.

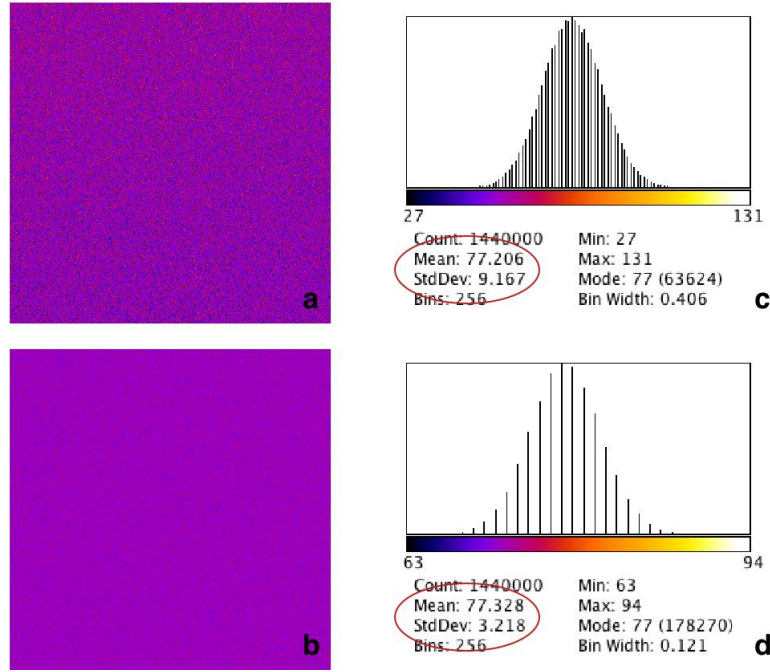


Fig. 3.16. Measurements in dark condition at 1 MHz (a) and 100 kHz (b) and the respective histogram (c) and (d).

III.9 HERALDO reconstruction and noise

An analysis of the photon noise influence in the HERALDO technique can be found in the thesis of M. Guizar-Sicairos ([8], Chapter 5, section 5.6). The SNR is analyzed in photon-limited statistics with theoretical discussions and numerical simulations. The findings are that the HERALDO technique is robust to the photon noise, and the bulk of noise contribution by the extended reference is effectively filtered during the reconstruction procedure. However, in our experiment, the diffraction patterns are far from photon-limited, due to the harmonic flux and its relatively low photon energy. An important step in the HERALDO reconstruction process is to apply the linear differential operator associated to the reference shape in the object space (the autocorrelation). This step, in practice, is realized by applying a point-by-point multiplicative filter, $W_{p,q}$, in the Fourier domain (the diffraction pattern or the hologram), where p and q is the index of the diffraction pattern pixel. Then, the object image is reconstructed by applying an inverse Fourier transform on the “filtered” diffraction pattern. In fact, $W_{p,q}$ is a high-pass filter, as presented in Fig. 3.17. This kind of high-pass filter will amplify the high spatial frequency region that is dominated by the readout noise. As a consequence this will degrade the HERALDO reconstructions of our recorded holograms. To eliminate the amplified readout noise, one can apply a low-pass filter, such as a Gaussian filter. In Fig. 3.17, the high-spatial-

frequency region of the multiplicative filters is eliminated by a super Gaussian filter (third order) with a diameter of 2000 pixels (full width at half maximum). The multiplicative filters are calculated in a window size of 2200 × 2200 pixels. In the following example of experimental data, I will show that the low-pass filter is essential to the HERALDO reconstruction process, especially with diffraction patterns significantly influenced by readout noise.

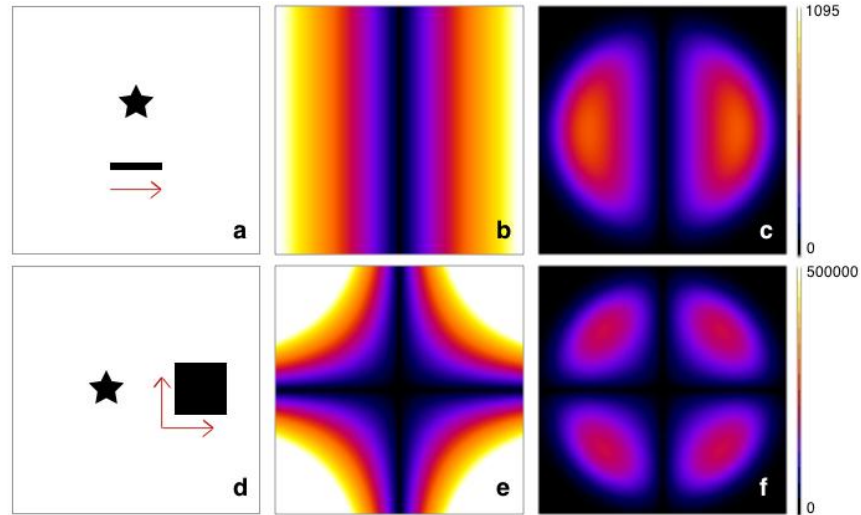


Fig. 3.17. Numerical simulation of the multiplicative filters (b and e) associated to one-dimensional slit reference (a) and two-dimensional square reference (d). The “star” is the object. (c) and (f) are the results of applying a super Gaussian filter (third order) on the multiplicative filters.

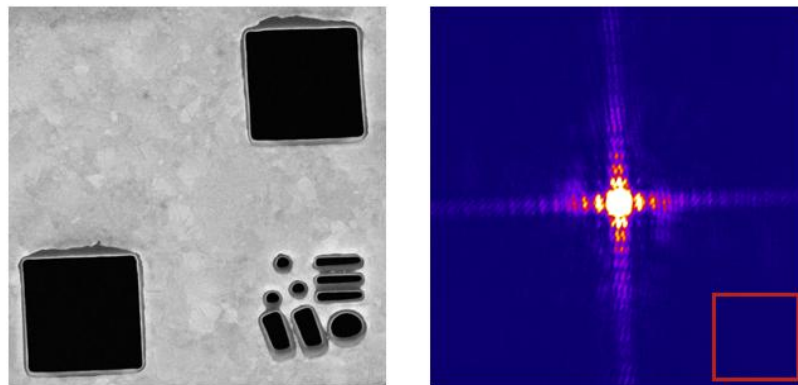


Fig. 3.18. (left) Test object A: SEM image of the geometry grid object with two square references. (right) Measured single-shot diffraction pattern of test object A.

The test object A (Fig. 3.18 left) is a geometry grid object (1 μm × 1 μm) with two square references (slightly larger than 1 μm × 1 μm). The object-reference distances

are slightly larger than the object size (holographic separation). The two squares can provide eight independent reconstructions (associated to the eight corners of the two squares) in one acquisition. We obtained a single-shot diffraction pattern with a readout frequency of 100kHz and within a window size of 600 x 600 pixels of 2 x 2 binning ratio (corresponding to 1200 x 1200 non-binned pixels). The measured diffraction signal is $\sim 6 \times 10^7$ photons. The readout noise has a standard deviation of 4 ADU and an average of 14 ADU, measured in the red square (Fig. 3.18 right) where there is no diffraction signal.

Fig. 3.19 presents the effect of the low-pass filter during the reconstruction process. When no low-pass filter is used (left column), the high spatial frequencies of the hologram are significantly amplified after applying the multiplicative filter. The reconstructions are completely covered by the noise. When applying a low-pass filter, whose diameter is too large (800 pixels) to eliminate all the amplified readout noise (middle column), the object is reconstructed but with a low quality. Applying a suitable low-pass filter (right column), whose diameter (400 pixels) is small enough to eliminate most readout noise at high spatial frequencies, the object is then clearly reconstructed. To quantify the noise contribution, we can use the power SNR of the reconstructed image [8]:

$$SNR_r = \frac{\sum_{p,q}^{N_o} |o_{p,q}|^2}{N_o (\sigma_{p,q}^2)} \quad (\text{Eq. 3-6})$$

SNR_r is the ratio between the signal energy and the noise energy presented in the reconstruction image. The signal energy $\sum_{p,q}^{N_o} |o_{p,q}|^2$ is calculated by integrating the signals inside the object region N_o (bleu square in Fig. 3.19), and the noise energy is the multiplication of N_o and its variance calculated in the region without signals (white square). Here, the noise energy is the total contribution of photon noise and readout noise. Note that SNR_r only accounts for the statistical noise and does not include the effects of resolution loss.

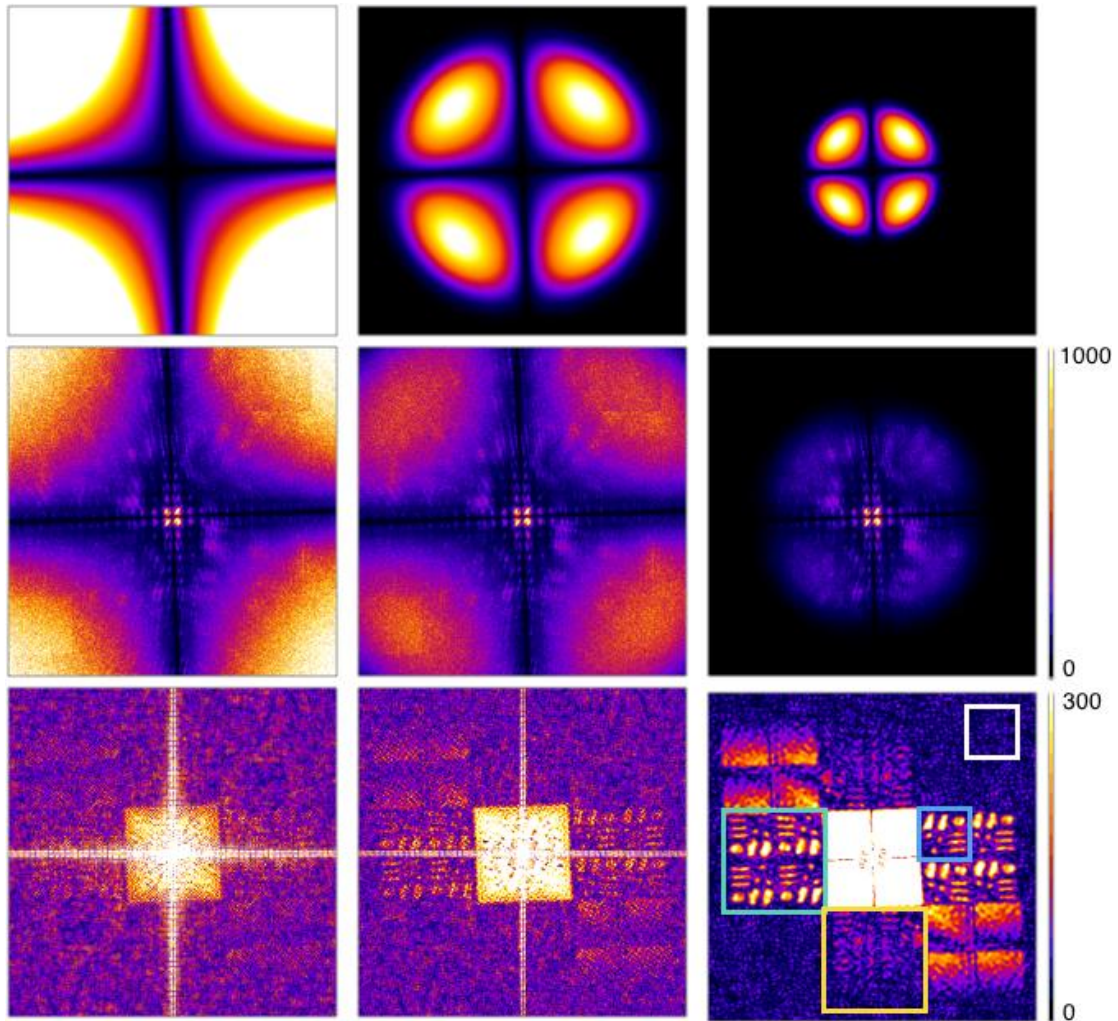


Fig. 3.19. Influence of the low-pass filter during the reconstruction process. (first row) Multiplicative filter with and without Gaussian filter. (second row) Results of the multiplication (in Fourier space) of the measured diffraction pattern by the HERALDO multiplicative filter with and without Gaussian filter. (third row) Inverse Fourier transform of the second row, giving the reconstructions. The eight independent reconstructions are within the green and the yellow square (each associated to a square reference). The bad reconstructions in the yellow square should be due to a miss-alignment that one reference has not been sufficiently illuminated. Note that the multiplicative filter is slightly tilted to agree with the diffraction axis.

I have then reconstructed the object A with different diameter of the low-pass filter (from 200 to 1000 pixels, every 100 pixels). The reconstructions are shown in Fig. 3.20. When the filter diameter increased, it is more difficult to reconstruct the object and more noise appears. We also note that the reconstruction is more blurred with smaller filter diameter. To estimate the resolution, I have plotted the profile of the reconstruction at the white line position in Fig. 3.21, and compared it to the

calculated SNR_r . The SNR_r increases with smaller filter diameter that high spatial frequencies (dominated by the readout noise) are eliminated. But the measured contrast (reflecting the resolution) does not always increase. It is maximized (0.76) at a filter diameter = 400 pixels, then decreases quickly at smaller diameters. The corresponding theoretical resolution for different filter diameter is presented in Table 3.1. Note that the measured contrast for diameter = 300 pixels (2×2 binning) is 0.65 and the period of the three horizontal slits of the object is ~ 190 nm. It means that the reconstruction resolution is worse than 95 nm, which is not limited by the filter diameter (75 nm). Therefore, the contrast decrease should be related to other factor like a loss of constructive diffraction signal.

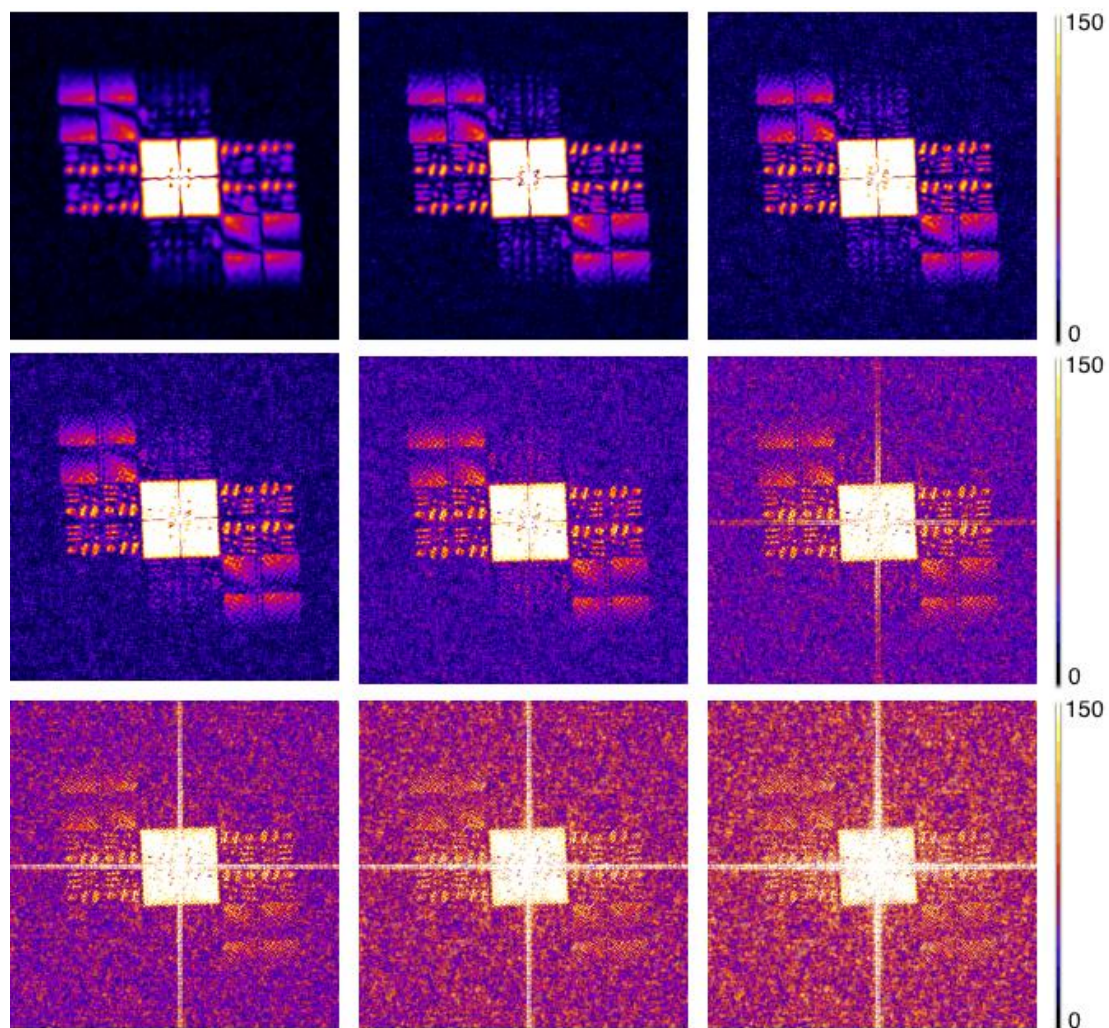


Fig.3.20. Reconstructions with different low-pass filter diameter. (first row from left) Diameter = 200, 300 and 400 pixels. (second row from left) Diameter = 500, 600 and 700 pixels. (third row from left) Diameter = 800, 900 and 1000 pixels. All images are presented with the same color scale.

Filter diameter	400	600	800	1000	1200	1400	1600	1800	2000
Non-binning									
2 x 2 binning	200	300	400	500	600	700	800	900	1000
3 x 3 binning	130	200	260	330	400	470	530	600	670
Theoretical resolution (nm)	113	75	56	45	38	32	28	25	23

Table 3.1. Theoretical resolution for different low-pass filter diameter with different binning ratio.

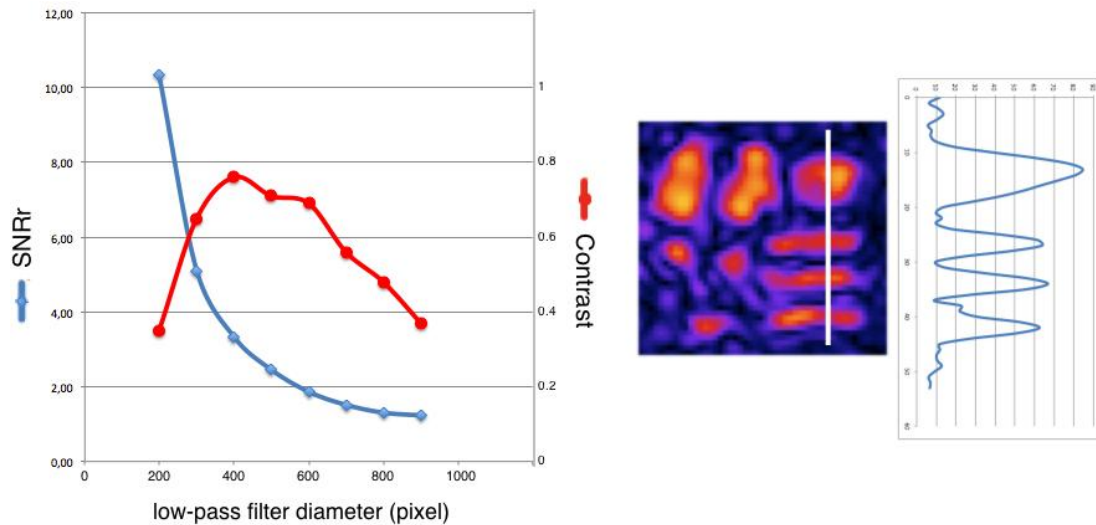


Fig. 3.21. (right) For each reconstruction, the measured contrast corresponds to the white line position. (left) Evolution of the SNR_r and the contrast with different low-pass filter diameter.

Since the readout noise is not correlated from one pixel to another, we can classify the pixels of the diffraction pattern by choosing two reasonable thresholds. To simplify the calculation, I use the ADU as the signal and noise unit in this section. I assume that for one pixel, it is *readout-limited* when there is no diffraction signal, which means that the ADU count of this pixel is within the readout noise distribution. The latter can be measured in a region far away from the diffraction signals, such as the red square in Fig. 3.18. A pixel is *photon-limited* when the ADU count of the pixel gives a photon noise 10 times higher than the readout noise. For example, with 1MHz readout frequency, the readout noise is equivalent to one photon signal (see section...). Moreover, a pixel whose ADU count is between these two thresholds is said to be *mixed-noise*. And a pixel is *non-ADU* if its ADU count is

zero after applying the low-pass filter. Therefore, all pixels are classified into four types, among which *photon-limited* and *mixed-noise* pixels provide useful signals for the reconstructions, and *non-ADU* pixels have no contribution to noise or useful signal. Fig. 3.22 presents the evolution of these four kinds of pixels when different filter diameters are used. Clearly, tighter low-pass filter turns more *readout-limited* pixels to *non-ADU* pixels, and that's the reason why the contrast of the reconstruction increases. However, for filter diameter smaller than 600 pixels, the *photon-limited* and *mixed-noise* pixels begin to decrease (eliminated by the tight filter, turned to *non-ADU* pixels). This can explain why the contrast decreases after the maximum. Therefore, one should find a good compromise between eliminating more *readout-limited* pixels and keeping more *photon-limited* and *mixed-noise* pixels. Fig. 3.23 shows the three kinds of pixels' distribution for a filter diameter of 400 pixels, where *mixed-noise* pixels are as important as *photon-limited* pixels for reconstruction. The sum of these two kinds of pixels presents almost the entire diffraction signals. The *mixed-noise* pixels are more influenced by the low-pass filter, as we can see in Fig. 3.22 where it decreases two times quicker than the *photon-limited* pixels.

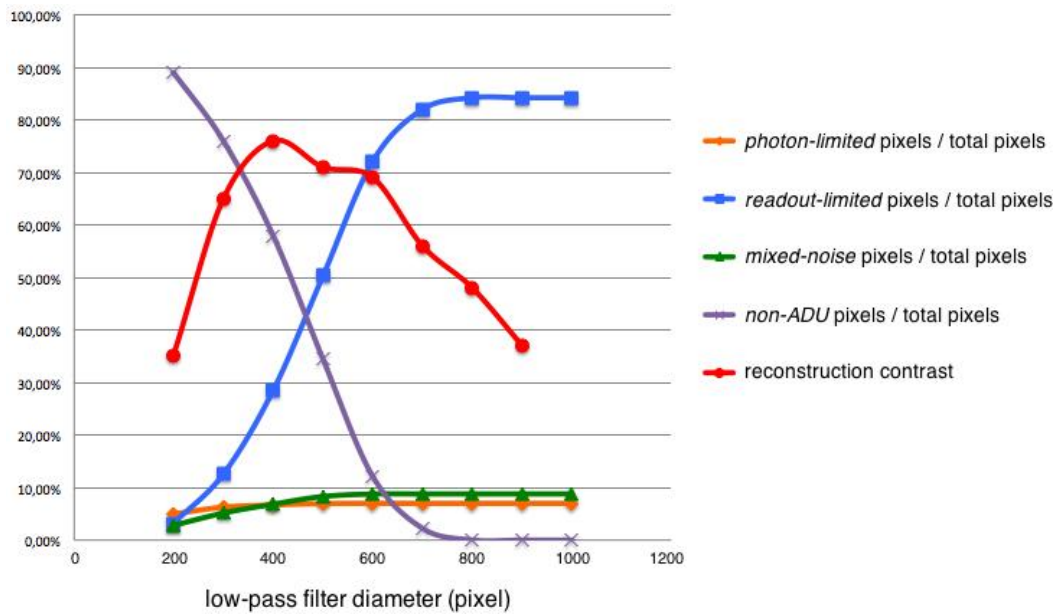


Fig. 3.22. Evolution of the four kinds of pixels with different filter diameters. The curves are the ratios between each kind of pixel number to the total pixel number. The reconstruction contrast curve is also plotted here for comparison.

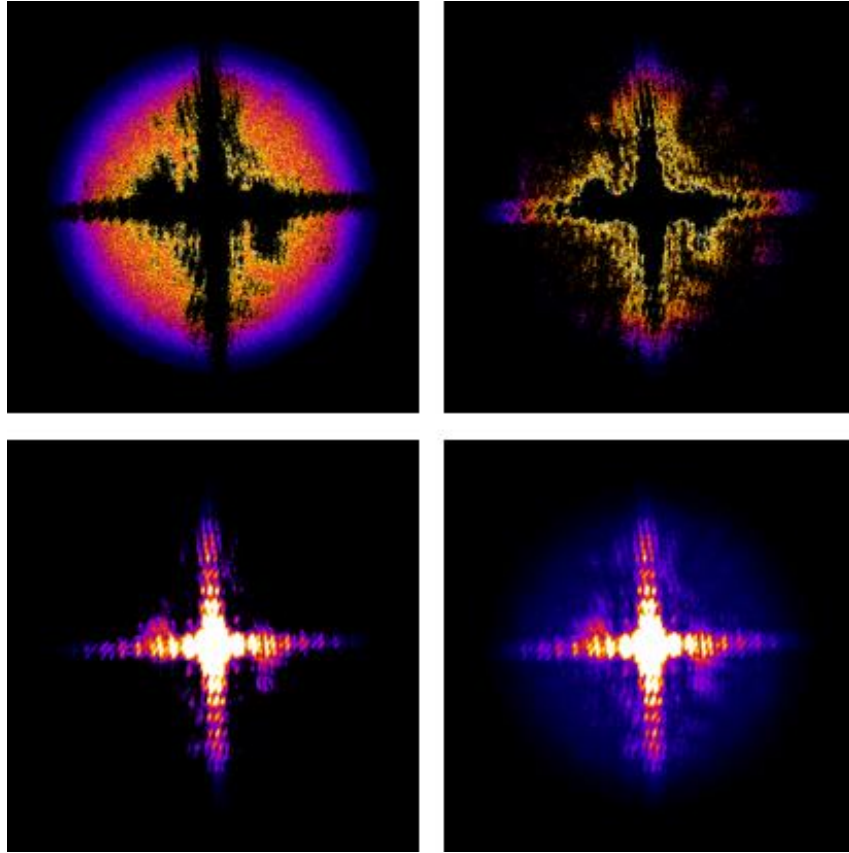


Fig. 3.23. (Top row) Distribution of readout-limited pixels (left) and mixed-noise pixels (right). (Bottom row) Distribution of photon-limited pixels (left) and total pixels (right). Images are filtered by a super Gaussian filter of 400 pixels diameter.

I present now another example (test object B), which is a geometry grid ($1\mu\text{m} \times 1\mu\text{m}$) with two slits reference (slightly longer than $1\mu\text{m}$) separated from the grid far enough to fulfill the holographic separation conditions (Fig. 3.24). The presented single-shot diffraction pattern (Fig. 3.24) is obtained with a readout frequency of 1MHz and within a window size of 600×600 pixels at a 2×2 binning ratio. The measured diffraction signal is $\sim 1.2 \times 10^7$ photons. The readout noise has a standard deviation of 9.8 ADU and an average of 38 ADU.

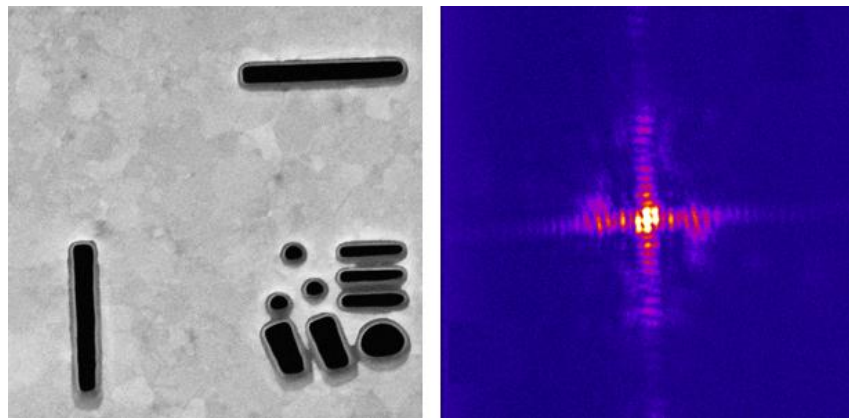


Fig. 3.24. SEM image of the test object B (left) and the measured diffraction pattern (right).

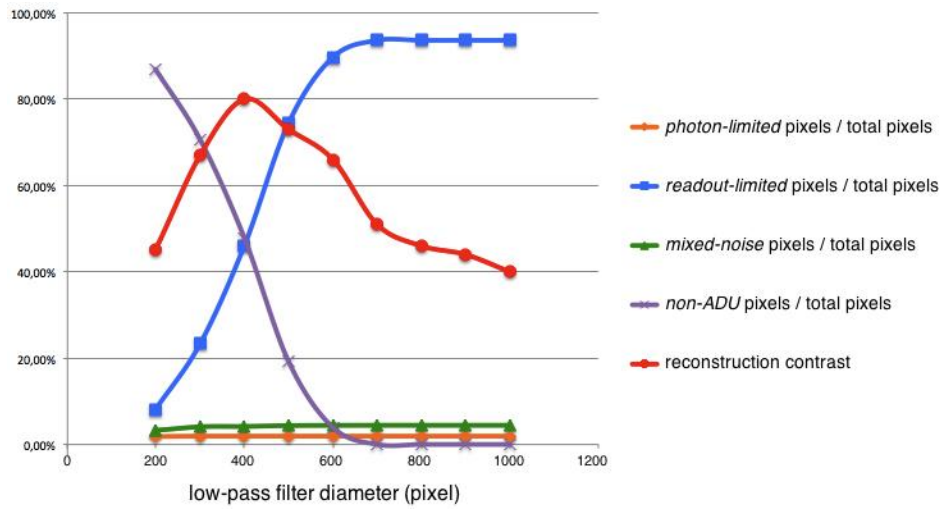


Fig. 3.25. Evolution of the four kinds of pixels with different filter diameters. The curves are the ratios between each kind of pixel number to the total pixel number. The reconstruction contrast curve is also plotted here for comparison.

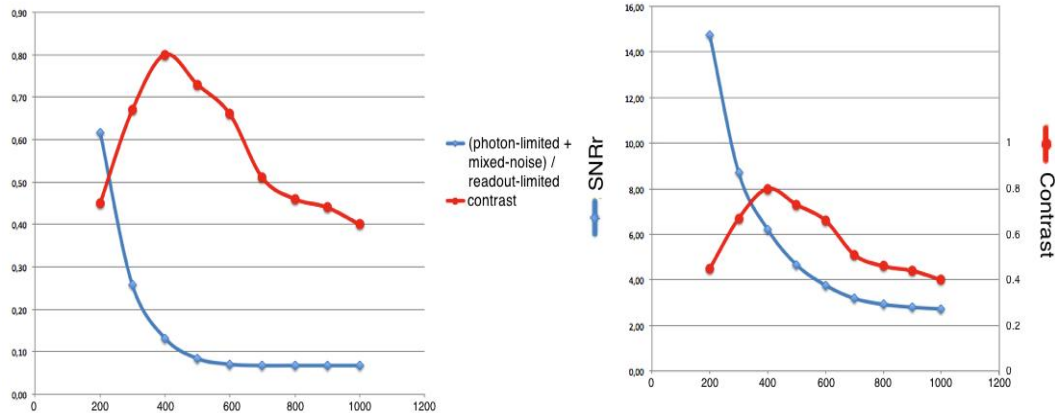


Fig. 3.26. (left) The blue curve presents the evolution of the ratio between (photon-limited + mixed-noise) pixels and the readout-limited pixels. (right) SNR_r evolution (blue curve) and the reconstruction contrast (red curve).

Using the same analysis method, similar results are obtained for the four kinds of pixels evolution (Fig. 2.25). The reconstruction contrast is again maximized (0.8) at a diameter = 400 pixels. Fig. 2.26 presents the variation of the ratio between (photon-limited + mixed-noise pixels) and readout-limited noise. The reconstruction contrast is enhanced to a relatively good range (> 0.6) when this ratio begins to increase. And the latter has a good agreement with the SNR_r in their evolution behavior. It confirms that the noise energy in the reconstruction image has a large contribution from the readout noise, which limits the reconstruction quality. Fig. 3.27 is a reconstruction of

object B with filter diameter = 400 pixels. Note that, reconstructions without low-pass filter are also resolved (Fig. 3.27 left) for this object due to the one-dimensional reference. The multiplicative filter is order 1 for one-dimensional reference and two for two-dimensional references. Therefore, the amplification of the readout noise is less important with slit reference than square reference, which is the advantage of one-dimensional reference. However, the resolution of the two-dimensional reference is theoretically non-limited, compared to the resolution limitation in the perpendicular direction of the slit reference.

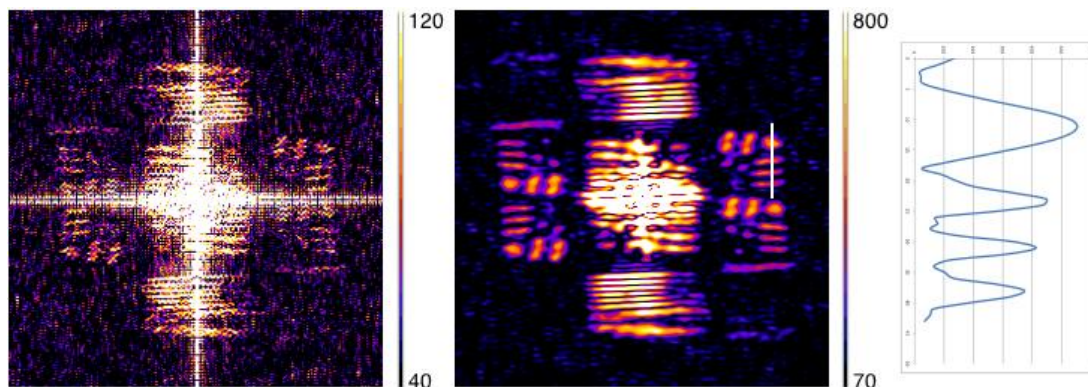


Fig. 3.27. Reconstruction of test object B without (left) and with (center) a low-pass filter diameter of 400 pixels. (right) Profile of the reconstructed object at the white line position.

III.9a HERALDO reconstruction and noise: Detection stage optimization with multiple shot acquisition

As demonstrated in the previous examples, the reconstruction of our diffraction patterns is mainly limited by the amplified readout noise. Therefore, the optimization of the detection stage will then focused on the readout noise. First, we can increase the incident harmonic beam flux by shots accumulation to have a higher signals/pixel ratio. Thus more pixels are then *photon-limited* or *mixed-noise*. Fig. 3.28 presents a comparison between single-shot and multiple-shot acquisition of the test object C, which is the same geometry grid ($1\mu\text{m} \times 1\mu\text{m}$) with two square references (slightly larger than the object) just beside it, which offer four independent reconstructions in one acquisition. Please refer to the caption of Fig. 3.28 for the detailed explanation of the reconstruction geometry. The measured 5-shot diffraction pattern has 2.9×10^8 photons and the single-shot acquisition has 5.9×10^7 photons. The ratio between the measured photons is ~ 4.9 . The standard deviation of the readout noise is 8.8 ADU and 9.6 ADU respectively for the single-shot and the 5-shots detections, with a same average of 33 ADU. Both images are recorded within a

window size of 1200 x 1200 non-binning pixels and the readout frequency is 1MHz. Comparing the analysis result (Table 3.2) of the 1-shot and 5-shot best reconstructions (Fig. 3.28 second row), which correspond to the highest reconstruction contrast, the *photon-limited* and *mixed-noise* pixels are increased by 3.4 and the SNR_r is increased by 1.5. Applying the Equation 3-6, we can get following equations:

$$SNR_{r_{single-shot}} = \frac{S_1}{P_1 + L_1} = 2.95$$

$$SNR_{r_{five-shot}} = \frac{S_5}{P_5 + L_5} = 4.51$$

where S is the signal energy, P and L are noise energy contributed respectively by the photon noise and the readout noise. And we have $S_5 = 5S_1$ and $P_5 = 5P_1$. Since the readout frequency and hardware binning ratio is the same, we have $L_5 = L_1$. Thus

$$\frac{P_1}{L_1} = 1.31$$

$$\frac{P_5}{L_5} = 6.55$$

The single-shot acquisition has equivalent photon noise and readout noise contributions in its reconstruction, while the 5-shot reconstruction is mainly influenced by the photon noise. The disadvantage of the accumulation is the eventual blur of the diffraction pattern due to the instable beam position, and radiation damage for certain samples.

	Filter diameter	$\frac{\text{photon} + \text{mix}}{\text{readout}}$	$\frac{\text{photon} + \text{mix}}{\text{total}}$	SNR_r	Theoretical resolution	Reconstruction contrast
1-shot	600 pixels	0.12	2.73%	2.95	75 nm	0.61
5-shot	800 pixels	0.26	9.38%	4.51	56 nm	0.75

Table 3.2. Analysis results of 1-shot and 5-shot best reconstructions.

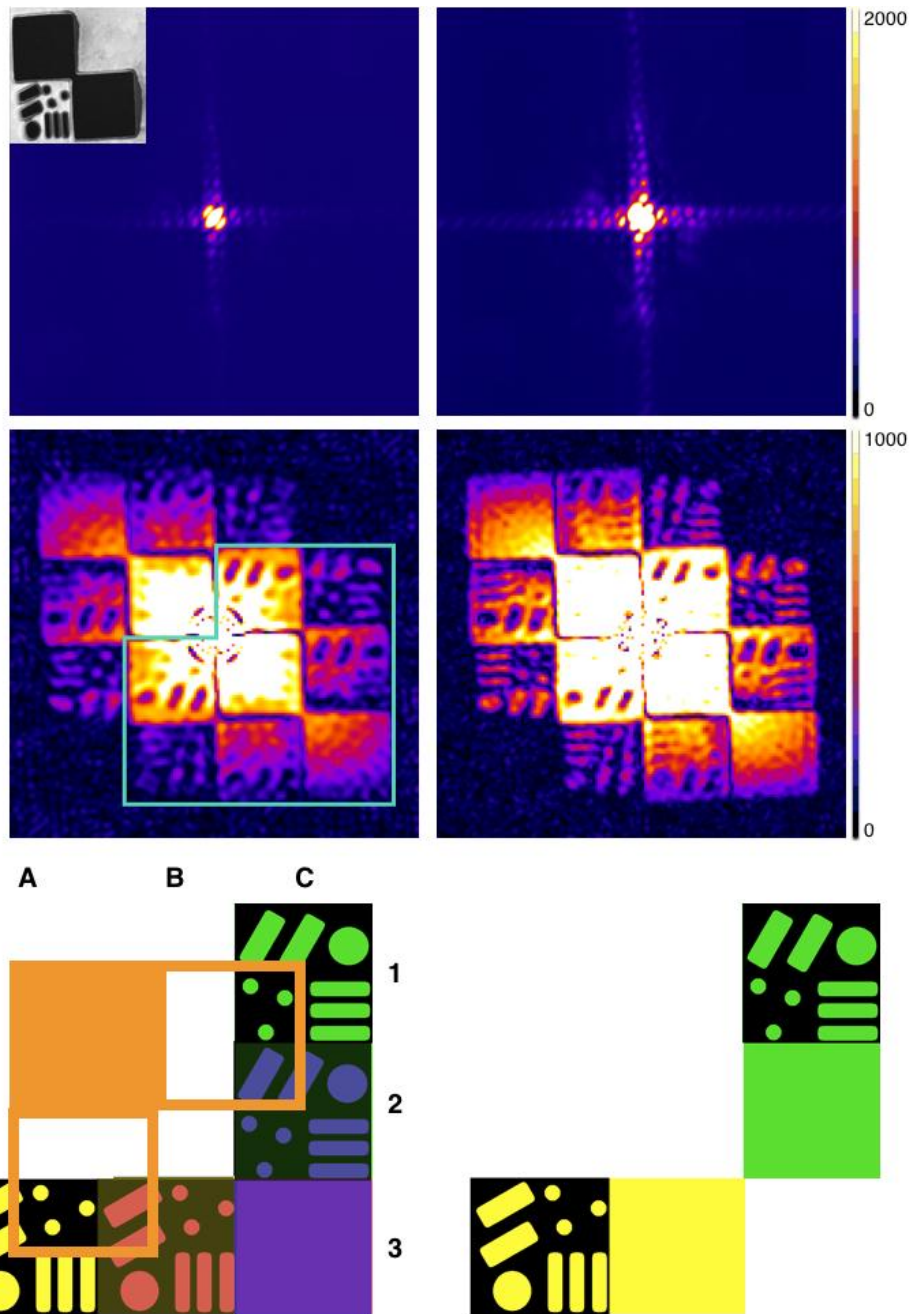


Fig. 3.28. Diffraction patterns (first row) and best reconstructions (second row) for single-shot (left) and 5-shot (right) detections of object C. The SEM image of object C is presented at the left-top. (third row) Reconstruction geometry: the yellow, red, blue and green rectangles (object with one square reference) are 4 independent reconstructions related to the 4 corners of the two orange hollow-squares (object centered on the corner). The orange full-square presents the object position. Yellow and red reconstructions are in the same direction, and the green and blue ones in the other. There is signal superposition of yellow reference and red object at B3, of green reference and blue object at C2, and of red reference and blue reference at C3. Moreover, the C1 and C2 corners are Dirac functions of opposite sign (+ and -) after derivation (refer to slit reference). Therefore, we observe the positive and negative reconstructions at C1 and C2 in the experimental results.

III.9b HERALDO reconstruction and noise: Detection stage optimization with hardware binning

The detection can also be optimized with the *hardware* binning option. The test object D (Fig. 3.29. top left) has the same geometry grid with one square reference close to the object. The total test object size is $\sim 2\mu\text{m} \times 2\mu\text{m}$, and the reference can provide three independent reconstructions. Considering the sampling ratio limit, I choose the hardware binning ratio of 1x1, 2x2 and 3x3. The detected diffraction patterns are presented in Fig. 3.29, with a zoom-in of a region (white square) where signals are confused with noises in 1x1 binning and are then emphasized in 2x2 and 3x3 binning. Note that the measured diffraction signal is 2.7×10^7 , 1.5×10^7 and 1.2×10^7 photons respectively for 1x1, 2x2 and 3x3 binning. With less diffracted signals, hardware binning is still able to extract the signal out of the noise, which can then be used for the image reconstruction. The readout noise for different hardware binning ratio is similar, with measured values of 8.8, 10 and 9.6 respectively for 1x1, 2x2 and 3x3 binning ratio.

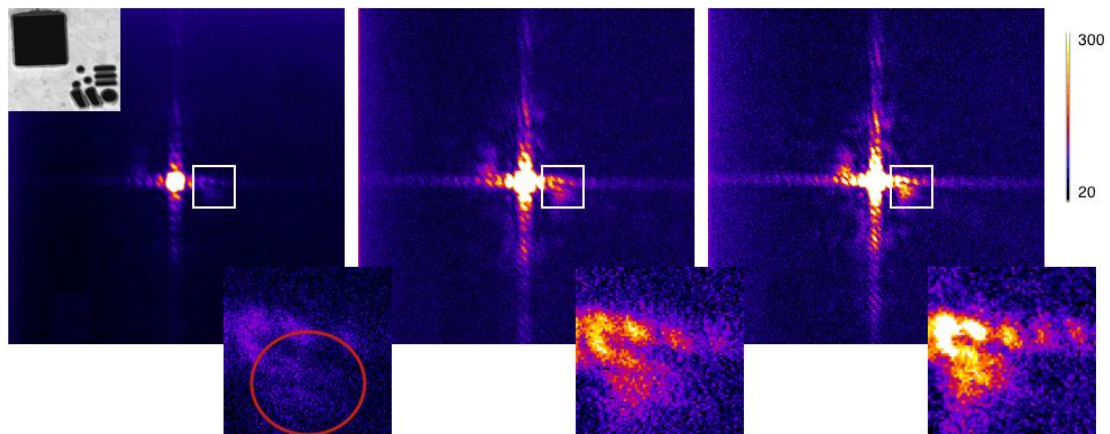


Fig. 3.29. Diffraction patterns for 1x1, 2x2 and 3x3 binning ratio (from left to right) of the test object D (top left). The zoom-in pictures correspond to the white square in each image and the red circle indicates the region where signals are extracted using higher binning ratio. The window size for each hologram (from left to right) is respectively 1200 x 1200 pixels, 600 x 600 pixels and 467 x 467 pixels. All the images are presented with the same color scale.

The reconstructions are realized with the same low-pass filter diameter of 400 pixels for 1x1 binning, 200 pixels for 2x2 binning and 130 pixels for 3x3 binning. The results (Fig. 3.30) present clear improvement of the *SNR*, when applying a higher binning ratio. Since the *SNR* does not take account of the resolution, I plot the profile at the white line position for each reconstruction to compare the achieved resolution (Table

3.3). The contrast is improved by hardware binning but the effect is not dramatic. Comparing the (photon-limited + mixed-noise)/total pixels percentage, 3x3 binning ratio does not extract more signal from noise and in this case, the 2x2 binning is enough. Note that the three horizontal slits of the object are not resolved in any of the three reconstructions.

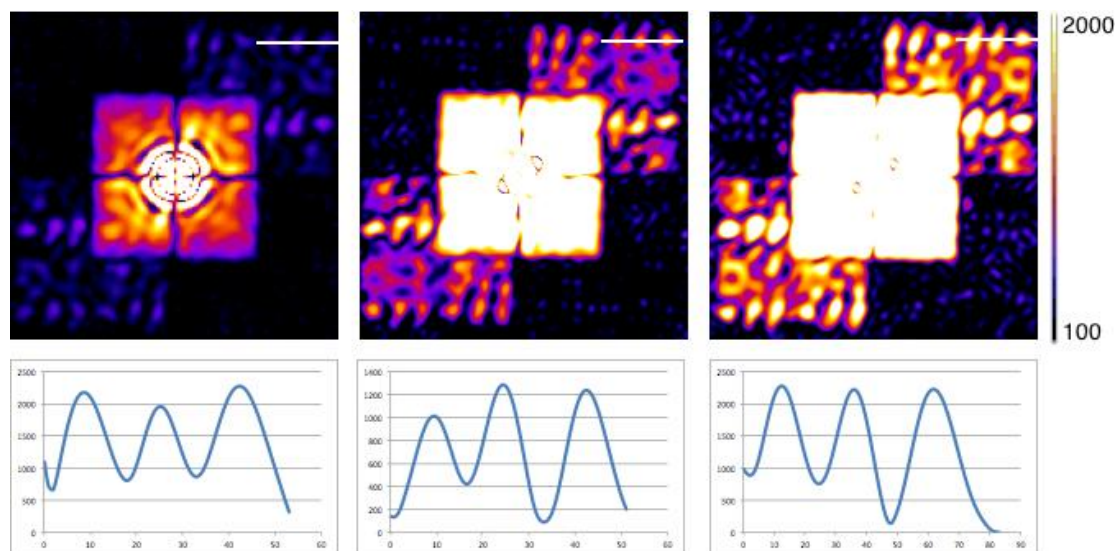


Fig. 3.30. Reconstructions of the diffraction patterns in Fig. 3.29 with 1x1, 2x2 and 3x3 binning ratio (from left to right). The plotted profile corresponds to the white line position. All images are presented with the same color scale.

Analysis Binning	Filter diameter	$\frac{\text{photon} + \text{mix}}{\text{readout}}$	$\frac{\text{photon} + \text{mix}}{\text{total}}$	SNR _r	Theoretical resolution	Contrast
1x1	400 pixels	0.11	1.14%	2.55	113 nm	0.64
2x2	200 pixels	0.33	2.76%	4.8	113 nm	0.68
3x3	130 pixels	0.35	2.80%	7.55	113 nm	0.69

Table 3.3. Analysis results of 1x1, 2x2 and 3x3 binning ratio reconstructions, with the same low-pass filter diameter (400 non-binning pixels).

After tuning the different parameters, the best reconstruction is achieved with a filter diameter of 200 pixels on 3x3 binning diffraction pattern (Fig. 3.31 white square). The measured reconstruction contrast is 0.67 and 0.71 for horizontal and vertical directions, with $SNR_r = \sim 3$. All the components of the object is resolved, especially the three slits and the three small holes.

This example shows clearly the signal improvement by using a proper hardware binning. Higher binning ratio does not always lead to more signals extracted from noise. And, one should always remember to respect the sampling ratio of the diffraction pattern. The other advantage of hardware binning is to reduce the long readout time when using 100kHz readout frequency.

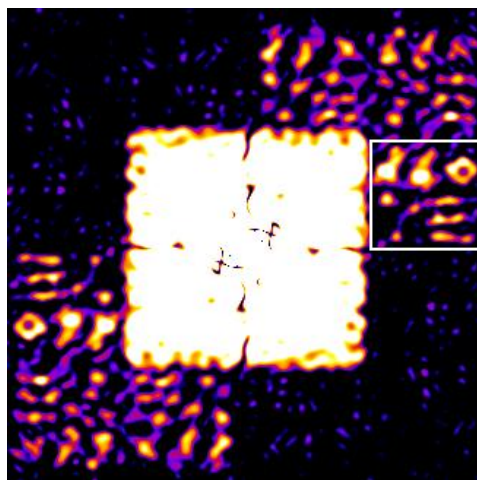


Fig. 3.31. Best reconstruction (white square) realized with a low-pass filter of 200 pixels diameter on the 3x3 binning diffraction pattern.

III.9c HERALDO reconstruction and noise: Detection stage optimization with the readout frequency

We consider now the test object A (Fig. 3.18). The diffraction patterns recorded with 1 MHz and 100 kHz readout frequencies are shown in Fig. 3.32. The two diffraction patterns have equivalent signals ($\sim 2 \times 10^7$ photons). The readout noise's standard deviation is 10 ADU and 4ADU respectively for 1 MHz and 100 kHz, with the same noise average (~ 30 ADU). Images are taken with 2x2 binning ratio and a window size of 600 x 600 pixels. Reconstructions (Fig. 3.33) are made with a low-pass filter of respectively 300, 400 and 500 pixels diameter. According to the analysis results (Table 3.4, correspond to the reconstructions in the yellow square), SNR_r is increased

by a factor of ~ 1.4 for 100 kHz reconstructions, with about 2 times more *photon-limited* and *mixed-noise* pixels. The resolution (contrast) is also better with 100 kHz readout frequency. Moreover, the reconstructions associated to another reference (in green square), which is difficult to be resolved (due to bad illumination of the reference), are better reconstructed at a 100 kHz readout frequency.

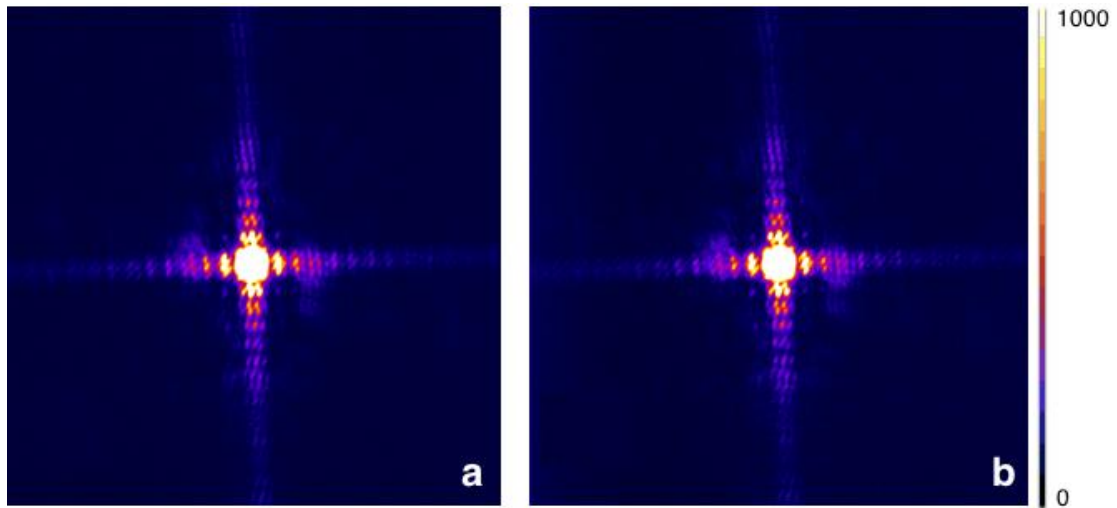


Fig. 3.32. Diffraction patterns taken with 100 kHz (a) and 1 MHz (b) on test object A.

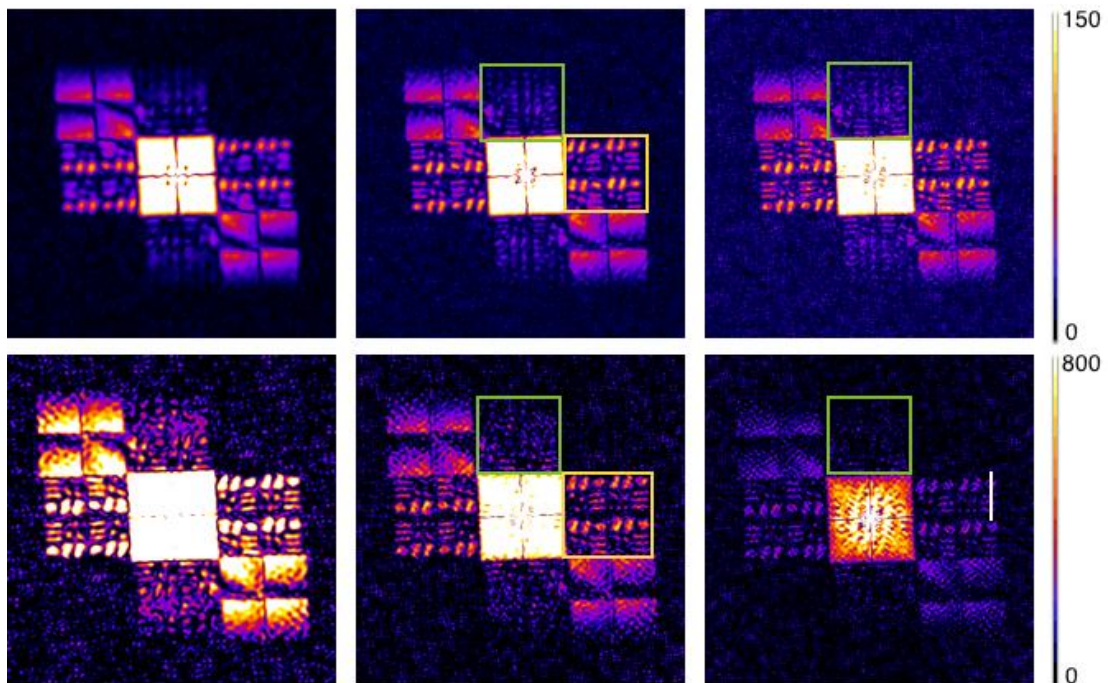


Fig. 3.33. Reconstructions of 100 kHz (first row) and 1 MHz (second row). They are made with filter diameters of 300, 400 and 500 pixels (from left to right). Green and yellow squares are associated to different square reference. The reconstruction contrast in Table 3.4 is

measured at the white line position.

Analysis Frequency	Filter diameter	$\frac{\text{photon} + \text{mix}}{\text{readout}}$	$\frac{\text{photon} + \text{mix}}{\text{total}}$	SNR	Theoretical resolution	Contrast
1 MHz	300 pixels	0.36	6.73%	3.83	75 nm	0.66
100 kHz	300 pixels	0.91	11.42%	5.1	75 nm	0.65
1 MHz	400 pixels	0.19	7.24%	2.24	56 nm	0.71
100 kHz	400 pixels	0.47	13.54%	3.33	56 nm	0.76
1 MHz	500 pixels	0.12	7.76%	1.7	45 nm	0.59
100 kHz	500 pixels	0.30	15.25%	2.45	45 nm	0.71

Table 3.4. Analysis results of the reconstructions.

III.9d HERALDO reconstruction and noise: other reference configurations

We have tested other HERALDO reference configurations. The test object E (Fig. 3.34E) is a geometry grid ($1 \mu\text{m} \times 1 \mu\text{m}$) located in a large square ($2 \mu\text{m} \times 2 \mu\text{m}$), which offers three independent reconstructions. The test object F (Fig. 3.34F) has the same geometry grid with two right-angled and isosceles triangles ($1 \mu\text{m} \times 1 \mu\text{m}$), which also offers three independent reconstructions associated to their corners. Note that the reconstruction associated to the right angle is the same as the one associated to a square reference. Diffraction patterns of the test object E is taken within a window size of 1200×1200 pixels without binning (Fig. 3.34a) and 600×600 pixels with a 2×2 binning ratio (Fig. 3.34b). The measured diffractions have a 1.5×10^7

photons and 2.1×10^7 photons with and without binning, respectively. Reconstructions are made with the same low-pass filter diameter: 400 pixels for non-binning and 200 pixels for 2x2 binning. Similar to previous results, the 2x2 binning provides a better reconstruction quality. In fact, two reconstructions of the non-binning diffraction pattern are not clearly resolved and the measured contrast of the other one is only 0.48, compared to 0.5 ~ 0.63 for the three reconstructions of 2x2 binning.

The test object F is imaged with a lower flux harmonic beam than that of the object E (Fig. 3.34). The 10-shot acquisition of the object F contains about 8×10^7 photons. It is due to the low optimization of the harmonic generation, probably caused by the position deviation of the IR laser beam before the focusing lens. In fact, IR beam properties are influenced by its propagation in the air before the focusing lens. The beam position at the lens plane is influenced by the room temperature, which is supposed to remain stable and cool during the experimental time. However, sometimes the strong temperature variation outside the building influences the room temperature that is tuned by air-conditioners (especially during the summer). This problem is later corrected by the laser modal filter with a servo system. The diffraction pattern is recorded within a window size of 1300×1300 pixels without binning. The readout noise is 9.5 ADU (standard deviation). Reconstructions from different references (blue and green square) are presented in Fig. 3.34f-g. The reconstruction quality is not comparable to the 5-shot acquisition of test object C (Fig. 3.28), probably due to a combination effect of low flux and low coherence harmonic beam generated in non-optimized conditions.

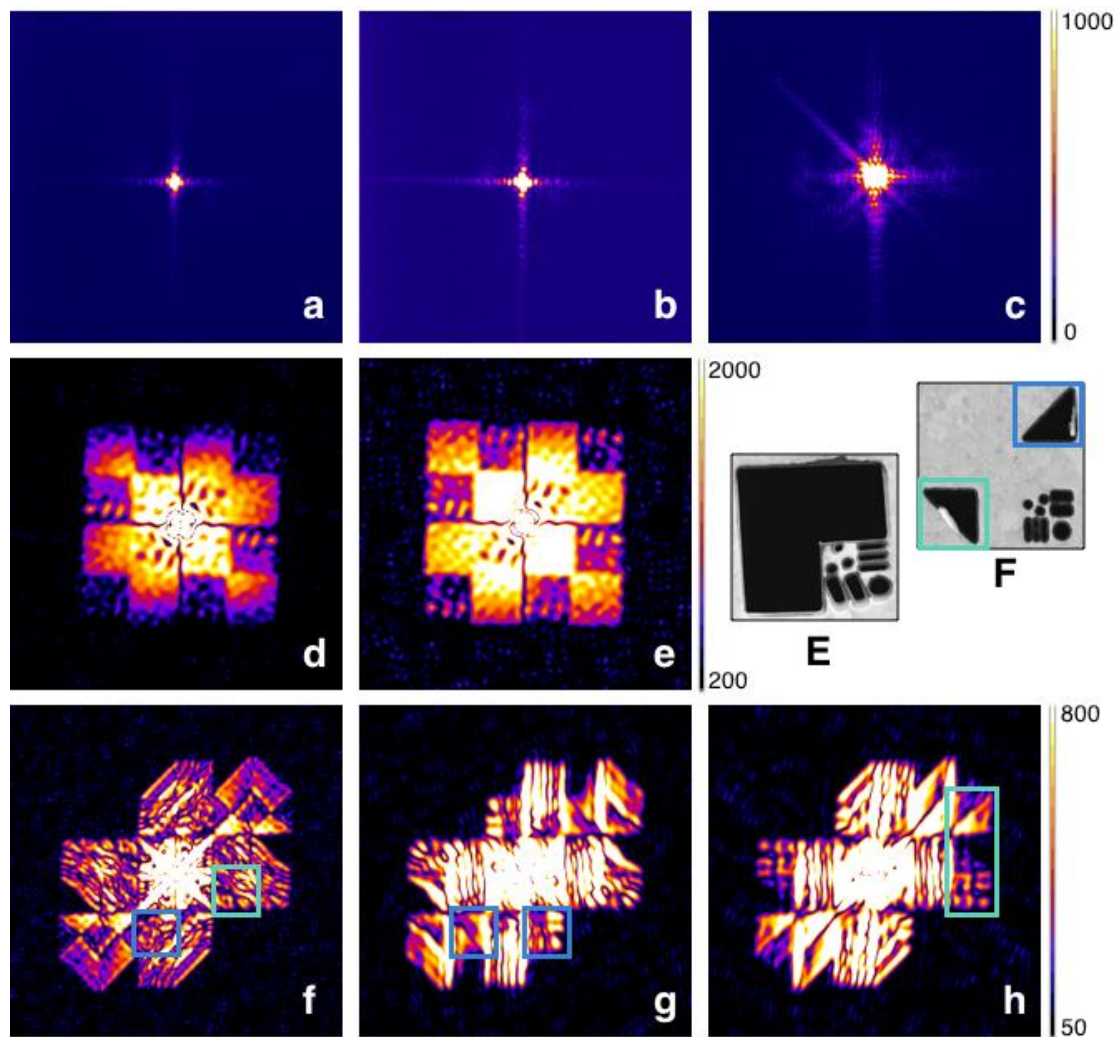


Fig.3.34. The test object E is reconstructed from a single-shot acquisition (b). The reconstructions (e) of 2x2 binning ratio present better quality than non-binning ones (d). The test object F is reconstructed with 10-shot acquisition (c). The reconstructions in green (f,h) and blue squares (f,g) are respectively associated to the references in green and blue square in the SEM image.

III.9e HERALDO reconstruction and noise: conclusion

We have first tested HERALDO with one-dimensional reference (slit) and two-dimensional reference (square). The step-to-step reconstruction process shows that the main obstacle for our experiment is the amplified readout noise located at high spatial frequency region. The amplification is introduced by the multiplicative filter applied on the diffraction pattern in the Fourier space, which corresponds to a differential operator for the autocorrelation in object space. The amplified noise then

degrades significantly the reconstructions after the inverse Fourier Transform. Thus, a low-pass filter in the Fourier space is required to eliminate the amplified noise. The analysis of different type pixels (*photon-limited*, *mixed-noise* and *readout-limited* pixels) presents the effectiveness of the low-pass filter with different diameter in Fourier space. In object space, the SNR_r and the contrast of the reconstruction characterize the reconstruction quality and the resolution. However, the latter is limited by the low-pass filter. Secondly, we have investigated the detection parameters (hardware binning, readout frequency, accumulation) to reduce the readout noise in the diffraction patterns. Different object-reference positions for two-dimensional references have been tested. In summary, the square reference does not provide higher reconstruction ability, compared to the slit reference. Due to the higher amplification of the readout noise by the former, the slit reference is a better choice for HERALDO technique on our harmonic beamline. However, the square or two-dimensional references are probably better for FEL facilities. Indeed, since the radiation flux and the photon energy are much higher, the diffraction pattern will be close to photon-limited. Compared to the FTH, which can also be considered as a special case of HERALDO, the latter presents higher reconstruction quality due to the signal amplification by the extended reference.

III.10 CDI reconstructions of HERALDO objects

To compare the reconstruction ability of CDI and HERALDO, we have made test objects of the geometry grid without any references. The diffraction pattern of such object (Fig. 3.35a) has much lower signal ($2 \sim 4 \times 10^6$ photons) than HERALDO objects, which has additional signal contribution from the extended references. The diffraction surface of the CDI geometry grid ($1 \mu\text{m} \times 1 \mu\text{m}$) is 8 times smaller than the lambda object ($3 \mu\text{m} \times 2.8 \mu\text{m}$). It has similar surface as the Young's double slits ($2 \times 1.5 \mu\text{m} \times 0.3 \mu\text{m}$) but with more complex structures. In this case, the phase retrieval code is not able to converge.

Meanwhile, the phase retrieval code succeeds in reconstructing the HERALDO geometry grid with its references. The test object is similar to object A (the geometry grid is $1 \mu\text{m} \times 1 \mu\text{m}$ large), but with fabrication default for the square references (the material inside the square is not completely removed) (Fig. 3.35d). It limits the HERALDO reconstruction from the corner close to it but in principle should not degrade the reconstruction by the phase retrieval code.

Fig. 3.35 presents two reconstructions (e,f) corresponding respectively to single-shot diffraction patterns containing 2.3×10^7 photons (b) and 1.1×10^7 photons (c).

Diffraction patterns are taken within a window size of 2048 x 2048 pixels without binning and at a readout frequency of 1 MHz. The difference of the reconstruction quality is due to the different signal strength. In the better reconstruction (Fig. 3.35e), the geometry grid is well resolved with a contrast equivalent to HERALDO results, and the defaults of the two references has also been reconstructed. Note that the curved edge at the left side of the square above the geometry grid is the reconstruction of the fabrication default. The little space between the non-removed material and the square edge in the SEM image is not resolved in the reconstruction. The noise in the red square of Fig. 3.35f is due to the ambiguity of the phase retrieval code. During the iterative process, the reconstructions of each iteration switched between three configurations so that the geometry grid is sometimes at right bottom, sometimes at left top and sometimes at both positions. With more diffraction signals, the code is able to go beyond this problem, as presented in the better reconstruction. Note that both CDI reconstructions use high software binning (5x5 for f and 4x4 for e) to get higher SNR (associated to the photon noise), which means that the extraction of the diffraction signal is more difficult in CDI process.

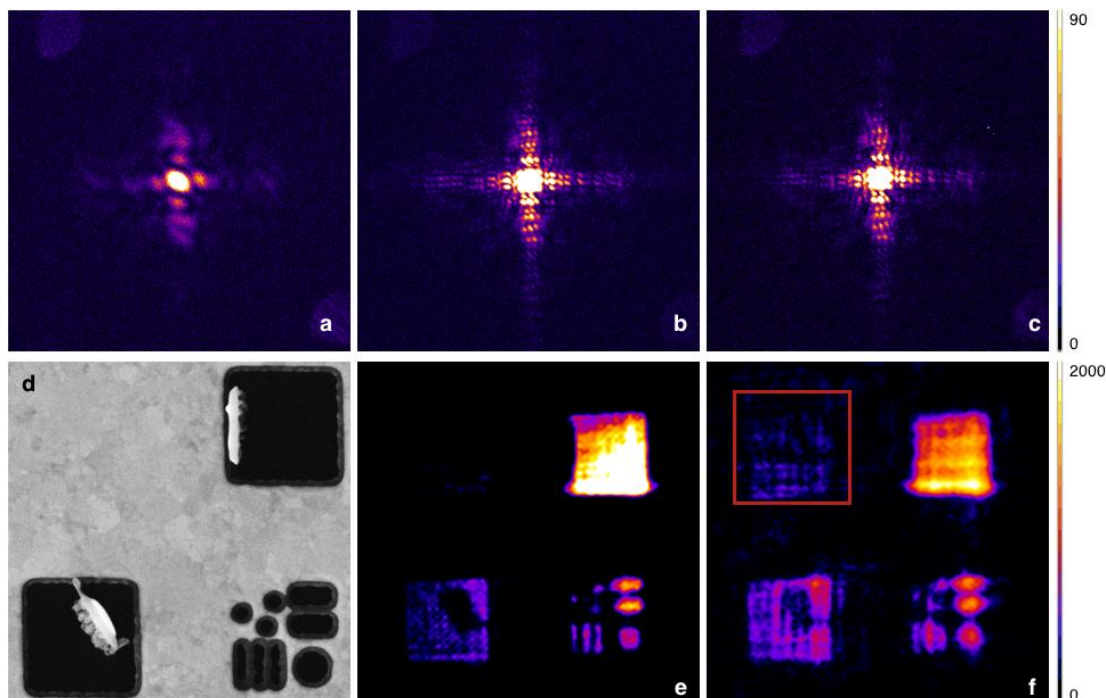


Fig. 3.35. (a) Single-shot diffraction pattern of CDI geometry grid. (b,c) Single-shot diffraction patterns of the HERALDO geometry grid. (d) SEM image of the sample. (e,f) reconstructions by phase retrieval code. The reconstruction (e) and (f) are respectively coherent averages of 37 and 50 reconstructions after 1000 iterations.

The following example is another demonstration of the CDI reconstruction of a HERALDO object. The test object (Fig. 3.36a) is “lambda” ($1.3 \mu\text{m} \times 1.8 \mu\text{m}$) with two slits slightly larger than the lambda. The slit width is 150 nm. The single-shot

diffraction pattern has $\sim 1.2 \times 10^7$ photons, recorded within a window size of 2048 x 2048 pixels without binning. The CDI reconstruction (Fig. 3.36b) shows equivalent quality as the HERALDO reconstructions (Fig. 3.36c,d). The former is made with 4x4 software binning and the latter is made with low-pass filter of 400 pixels diameter. Note that in the CDI reconstruction, the lambda looks like a superposition of a vertical slit and itself. This is also due to the ambiguity of the phase retrieval code. Indeed, the position of the vertical slit is difficult to identify during the iteration process, since the center part of the lambda has a similar geometry as the vertical slit. It has no problem to identify the horizontal slit because no similar structure presents in the "lambda" object. The resolution of the CDI reconstruction is estimated to be ~ 115 nm by the PRTE, which is equivalent to the HERALDO ones (10%-90% criterion). From these examples, we can conclude that extended references amplify the signals diffracted from the object that can help the convergence of the phase retrieval code. Moreover, the latter need higher SNR of the diffraction pattern to reconstruct the object than the HERALDO process. However, CDI does not require a reference, which is an advantage for certain applications.

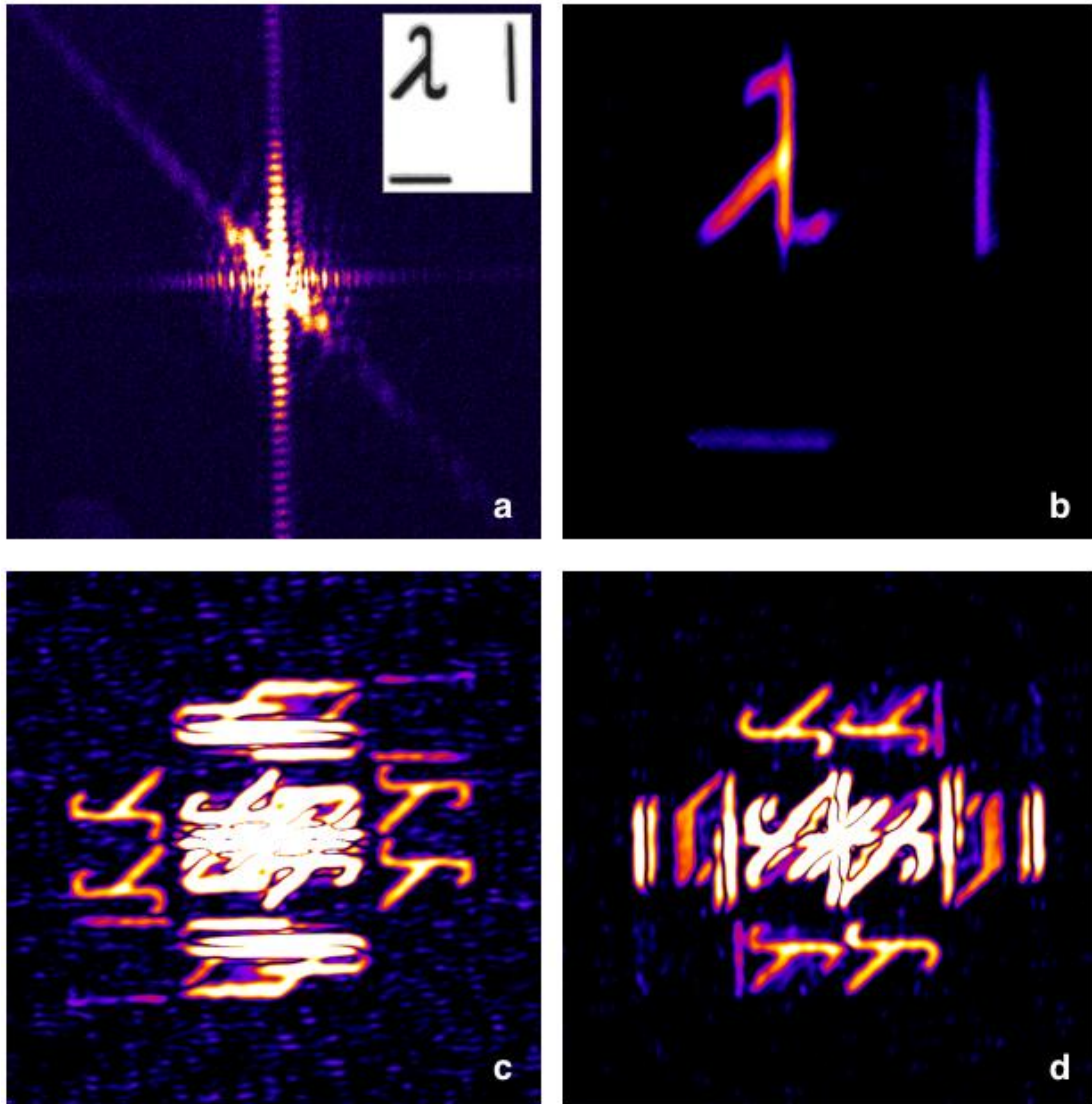


Fig. 3.36. (a) Single-shot diffraction pattern of the HERALDO object (inset). (b) CDI reconstruction result, which is the average of 50 reconstructions after 1000 iterations. (c,d) HERALDO reconstructions.

III.11 Conclusion

In this chapter, I have presented the experimental results of CDI, HERALDO and FTH techniques. In the CDI section, coherence requirement has been discussed and analyzed quantitatively using Young's double slits diagnostics. I showed that the reconstructions are not converging for a contrast of interference fringes lower than 0.5. In the second part, the HERALDO process has been investigated step-by-step. Our finding is that the readout noise is the main obstacle in our experiments. A low-pass filter is the solution for this problem, which compensate the amplification of the

readout noise by the multiplicative filter. Various demonstrations show that the reconstruction quality can be improved by the optimization of the detection stage and a carefully chosen low-pass filter diameter. The comparison between FTH, one-dimensional and two-dimensional HERALDO shows that the slit reference is the best holographic configuration for our harmonic beam, according to its photon energy and photon flux properties. Finally, application of phase retrieval code on the HERALDO samples demonstrate that the extended reference amplifies the signals diffracted from the object. It also shows the higher requirement of SNR for CDI reconstruction compared to HERALDO. In conclusion, both CDI and HERALDO have their own advantage and default depending on the experimental conditions. This careful analysis presented here will guide us in choosing the best imaging technique for the imaging application of magnetic nano-domains (Chapter IV).

Chapter IV- Towards single shot 3D Coherent Imaging

IV.1 Introduction

In nature, most of the materials are three dimensions objects. At a nanometer scale, the ability to visualize the 3D organization and the properties of artificial or biological systems is of high impact in science, medicine and technology. The field of coherent X-ray diffractive imaging is expected to realize high-resolution three-dimensional imaging because of it requires no optics. The imaging techniques presented in previous chapters are two-dimensional reconstruction of the object. For many scientific applications, especially in biology and medical imaging, 3D information of the object is necessary. The typical way to make 3D reconstruction of the object is the tomography method [1,2], in which object is scanned section by section. It requires multiple acquisitions at different observation angles of the object. For dynamic studies in pump probe experiment, if the object will irreversibly be transformed or be destroyed after being pumped, one should prepare enough quantity of identical samples for tomography experiment, which could be a problem for unique objects or processes that are not possible to be reproduced. To overcome this problem, retrieving 3D information from single acquisition is necessary.

A solution has been given by a novel imaging concept proposed by the research group of J. Miao, called ankylography, which “under certain circumstances enables complete 3D structure determination from a single exposure using a monochromatic incident beam” [3]. Ankylography is a coherent imaging technique based on the oversampling method. It shares a similar experimental arrangement as CDI. The difference is that ankylography requires one more oversampling condition corresponding to the third dimension, which is the beam’s propagation direction. The phase retrieval algorithm is processed in three dimensions. In principle, a finite object illuminated by a coherent beam scatters light on a sphere called the Ewald sphere (see the definition in next section). The measured 2D diffraction pattern recorded by the CCD camera is a projection of it in which the 3D structure information of the object is encoded. The 3D reconstruction is then possible by transforming the measured 2D diffraction pattern into a 3D spherical pattern. Fig. 4.1 shows a demonstration of the ankylography on experimental data obtained using an HHG source. The fabrication defaults observed in the SEM image of the object (Fig. 4.1e) are reconstructed by ankylography (Fig. 4.1b,c) using the spherical diffraction pattern (Fig. 4.1a) calculated from one acquisition.

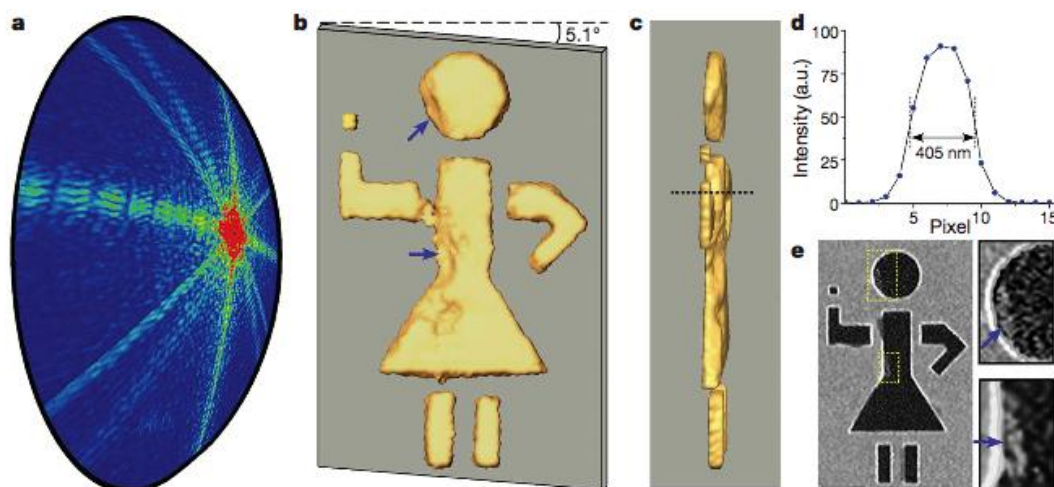


Fig. 4.1 Demonstration of Ankylography on experimental data from Ref. 9.

These results have been obtained in multishot acquisition (about 10^5 shots) Preliminary single shot studies of this technique has been launched using our harmonic beamline. The demonstrations of coherent diffraction imaging techniques (CDI and HERALDO) on simple test objects in the previous chapter have shown robust image reconstruction quality and the potential of resolving concrete problems in various scientific areas from physics to biology. The optimization and standardization of the high flux harmonic beamline (Chapter II) provide a reliable high soft X-ray flux with a stable beam quality (intensity, pulse duration, spatial profile, beam position, etc.) from shot to shot, all combined with a natural synchronization with the IR pump laser. The HHG beamline competes well with FEL facilities, which suffer from synchronization jitter and instabilities of the beam quality. We present here the progresses in 3D imaging using our harmonic beamline.

IV.2 Basics in three dimensional coherent imaging

In three-dimensional coherent diffraction imaging, a coherent beam of wavelength λ illuminates a 3D periodic or non-periodic object. Here we describe the 3D structure of an object by its complex electronic density $\rho(x, y, z)$. The interaction between the beam and the object can be represented by the scattering potential of the object $o(x, y, z)$:

$$o(x, y, z) = r_e \rho(x, y, z) \text{ eq.1}$$

where r_e is the classical electron radius.

The scattering wave after its interaction by the object propagates freely. We will describe the light propagation under the Born approximation.

As shown in Fig. 2, k_{in} represents the incoming wave vector and k_{out} the scattered wave vector at an angle 2Θ and projected onto the detector plane. In the far field, the object scattering function may be decomposed into a Fourier representation of 3D volume spatial frequencies: $\mathbf{k} = (k_x, k_y, k_z)$, with complex amplitudes.

$$C(\mathbf{k}) = \mathcal{F}\{o(x, y, z)\} = \iiint_{\mathbb{R}^3} o(\mathbf{x}, \mathbf{y}, \mathbf{z}) e^{-2\pi i(k_x x + k_y y + k_z z)} d\mathbf{x} d\mathbf{y} d\mathbf{z} \quad \text{eq.2}$$

In the experiment, this continuous far field scattering function is detected in intensity $I(\mathbf{k})$ by a 2D pixelated detector such as a CCD (charge-coupled device) camera. Thus this measured intensity is sampled numerically on the detector pixels $\mathbf{p}=(p_i, p_j)$ (see Fig. 2).

$$I(\mathbf{k}) = C(\mathbf{k}) * C(\mathbf{k})^* = |\mathbf{F}(\mathbf{k})|^2 \quad \text{eq.3}$$

Where $\mathbf{F}(\mathbf{k})$ represents the numerical magnitude of the Fourier transform :

$$F(k_i, k_j, k_z) = |\mathcal{F}\{o(x, y, z)\}| = \left| \sum_{x=0}^{l-1} \sum_{y=0}^{m-1} \sum_{z=0}^{n-1} o(x, y, z) e^{2\pi i(k_x \frac{x}{l} + k_y \frac{y}{m} + k_z \frac{z}{n})} \right| \quad \text{eq.4}$$

$k_i=0, \dots, l-1; k_j=0, \dots, m-1; k_z=0, \dots, n-1$

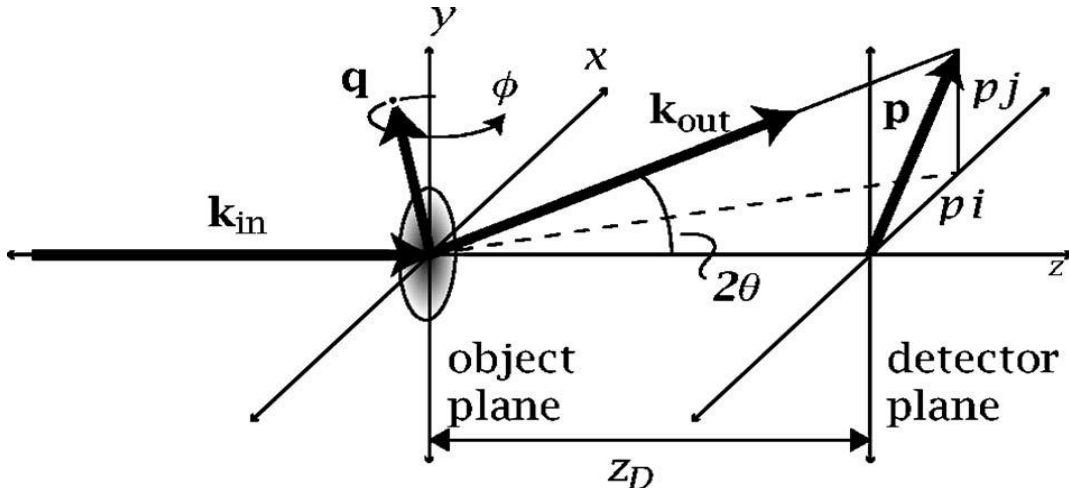


Fig. 4.2: Scattering geometry for coherent x-ray diffraction imaging. The sample is rotated about the y axis by an angle.

From Bragg's law, we know that the light scatters at an angle 2Θ from the incident beam direction along the forward direction (the z axis). The volume grating is tilted by an angle Θ from perpendicular to the forward direction [4,5]. Then, to have constructive interference, the magnitude of the wave-vector transfer difference should be equal to: $|q| = 2 \sin \frac{\Theta}{\lambda} = \frac{1}{d}$ where d is the increment size (or the smallest object detail) for periodic object. Since the grating spatial frequency can be expressed with k with magnitude $|k| = \frac{1}{d}$, for elastics scattering, the wave-vector transfer is equal to the grating spatial frequency, that means only the volume gratings that satisfy Bragg's law will scatter, that is $q = k$.

In order to get information from all different plane spacings in which the object can be decomposed, one has to change the angle Θ . One therefore has to rotate the specimen and record holograms at each rotation angle. In this context, a sphere called Ewald is constructed as shown below in fig. 4.3:

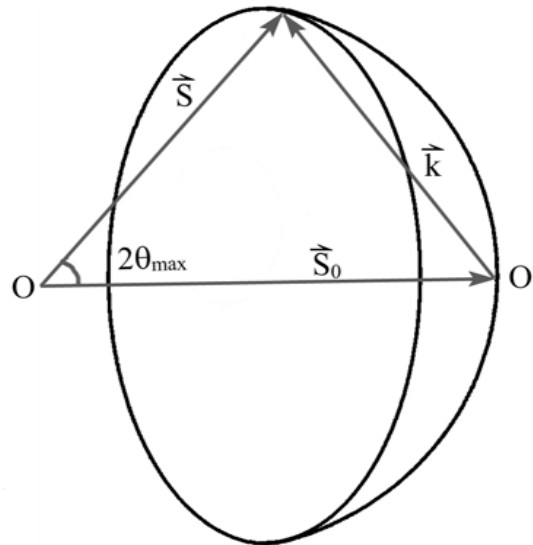


Fig.4.3: Geometrical construction of the wave vectors and the Ewald sphere.

where the S_0 and S are the incident and scattered wave vectors with magnitudes equal to $1/\lambda$, and these spatial frequencies k lie on the Ewald sphere of radius $1/\lambda$, [22,23] where λ is the incident coherent radiation wavelength.

Here we note that one Ewald sphere is constructed for one direction of the beam towards a 3D object at a fixed angle and position. If either the beam rotation (ex: in crystallography) or the object rotation (tomography) is changed, the Ewald sphere is no longer the same. In this case, a new Ewald sphere is constructed. This notion is extremely important when choosing an appropriate 3D imaging technique. In general 3D imaging method, we rotate the sample to the beam axis to accomplish all

the full 3D Fourier reciprocal space of object. For each angle, the Ewald sphere has to be constructed. This is well explained by the scheme in Fig. 4.4:

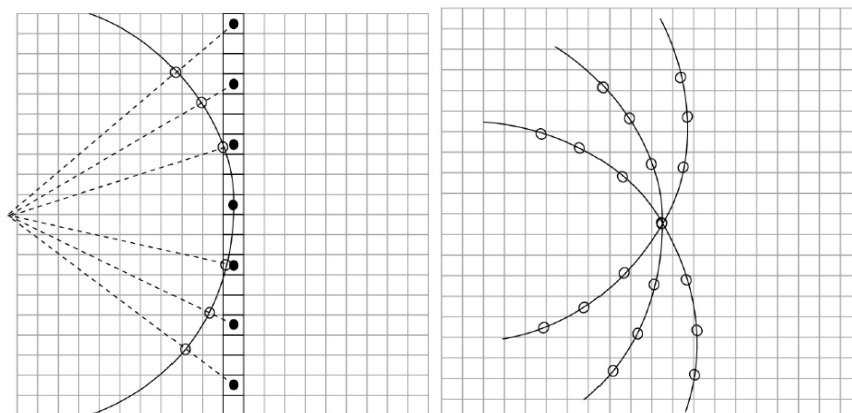


Fig.4.4: Scheme of the 3D data assembly: Left: we present the projection of the Ewald sphere fields in reciprocal space (closed dots) on a regular grid that simulate a pixelated detector (a CCD camera for example). Right: we show different Ewald sphere sections from three different sample orientations.

From fig.4.4.a, we see that the diffraction data can only be recorded in two-dimensional slices which are the closed dots. First, we need to realize an inverse gnomonic projection for this two dimensional plane to one Ewald sphere: that means each magnitude, recorded on a plane, has a correct location in the reciprocal space. However, the set of correct locations embedded in the regular array of recorded magnitudes is not itself a regular array but rather a series of points on a sphere. Thus the irregular series of points on the Ewald sphere sections should be interpolated to the regular grid points (this step will be crucial for further Fourier transform computation). We repeat this operation for each sphere with different orientations. So the calculation of the correct locations for the measured magnitudes in the three dimensional reciprocal space (3D cube data) is well realized and accomplished. Finally, from this 3D Fourier reciprocal data, we can see that the level of sampling of the diffraction pattern is a sharp function of frequencies. This results from the overlap of slices near the origin. At higher spatial frequencies there will be regions between the slices which are completely unsampled (or unmatched).

We note that in 3D tomography, there is no limit on the focal depth. This means that the focal depth is much longer than the thickness of 3D object. Thus we can image a thick 3D object without limits in depth which are requested in other 3D imaging domains such as confocal microscopy and scanning electron microscopy.

IV.3 CDI reconstruction algorithm in 2D and 3D

Until now, I have discussed the Fourier space data assembly both in 2D and 3D case. We can see that 2D is the basic stone to go to 3D, since 3D is just doing sometimes the repeated step over several 2D cases. Before presenting the 3D image reconstruction, 2D reconstruction from 2D plane diffraction pattern is reviewed. Here I explain the basic notions since there is a very close relationship between the ideas of reconstruction algorithm development in 2D and 3D. We will see that in the phase retrieval approach, the notion of oversampling ratio is crucial both in 2D and 3D images reconstruction [6-9].

- *The phase problem: phase retrieval using the oversampling method*

The examples shown in section IV.2, shows that only the diffracted intensity is recorded by plane detector. Obviously, the phase in each pixel (2D) or voxel (3D) in Fourier space measurement is lost. Thus we cannot inverse directly these values (Fourier magnitudes) in Fourier space either 2D plane or 3D cube to recover the complex-valued object in real space. Phase retrieval algorithms are then used to retrieve the lost phase.

We know that reconstructing the object consists essentially in solving a set of equations at each point [6]. This means that the magnitude value (square root of measured intensity by detector such as CCD) located at each point (pixel in 2D and voxel in 3D) is a function of all the points of the object in real space. If there are N points in each dimension of the object in real space, then a 2D object has N^2 points and a 3D object have N^3 points. This function is non-linear. If the number of the points in Fourier space is equal to that in real space, thus we have N , N^2 , N^3 equations corresponding respectively to 1D, 2D, 3D objects.

If the electron density of an object is a complex-valued, each point in real space has two unknown variables: the real part and the imaginary part. Thus for a 2D and 3D complex-valued object, we need to resolve $2N^2$ and $2N^3$ unknown variables respectively with a total number of equations equal to N^2 and N^3 respectively.

If the electron density of an object is real, thanks to the Friedel's law, the magnitude of its Fourier transform as $F(k)$ in eq.4 has a central symmetry. Therefore the equation number for a 2D and 3D real object drops to $N^2/2$ and $N^3/2$ respectively, and the number of unknown variables is N^2 and N^3 , respectively. [6,7]

If the object is infinite with a period size of a (as for example in crystallography), by the convolution theorem of Fourier theory, we know that its Fourier distribution (or diffraction intensity or magnitude) is given by an array of delta functions with a period $1/a$:

$$F(u) = F_0(u) \frac{1}{a} \sum_{m=-\infty}^{m=+\infty} \delta(u - m/a) \quad |F(\mathbf{u})| = \left| \sum_{\mathbf{r}=0}^{N-1} \rho(\mathbf{r}) e^{2\pi i \mathbf{u} \cdot \mathbf{r} / N} \right|, \quad \mathbf{u} = 0, 1, 2, \dots, N-1$$

This period is also called Bragg sampling interval. Bragg peaks correspond to the discrete position of this period. Therefore the detector need to sample at least with a frequency equal to Bragg sampling, that means sampling the diffraction pattern over N pixels each having a width $1/a$. In this context, the phase problem is however underdetermined by a factor of 2 for all the 1D, 2D, 3D objects. Thus a priori information about the object needs to be known to have a unique solution for the phase problem in eq.4. For this, The first strategy is to decrease the number of unknown variables by using objects with some known scattering density (i.e., some known valued pixels) inside them. The ratio σ is defined as the threshold to determine how many valued pixels in real space are necessary to solve eq.4:

$$\sigma = \frac{\text{total pixel number}}{\text{unknown - valued pixel number}}$$

The set of equations (eq.4) should be solvable, at least in principle, as long as the ratio $\sigma > 2$. Since each equations of eq.4 is nonlinear, having two solutions because of the modulus sign, an application of positivity constraints can be used to eliminate one the two.

$$\sigma = \frac{(\text{electron density region}) + (\text{no - density region})}{(\text{electron density region})}$$

The second strategy to increase the number of known quantities (point values in object real space) is to use the oversampling method. The idea of oversampling is to sample the magnitude of a Fourier transform (diffraction pattern) more densely than the Bragg frequency to generate a no-density region surrounding the electron density of the object. Practically, that means a finite support for the object in which the pixel value outside the finite support is zero. σ is also called oversampling ratio [6]:

If the object is a single, isolated object of width a , the Fourier pattern results in a continuous distribution. To recover the phase for this case, we can extend the method of oversampling in crystallography as presented above since isolated object can be expressed by an object surrounded by zero values outside the object electron density region. Therefore, if the diffraction pattern is sampled on a finer scale than $1/2a$, the unique phase can be retrieved. Furthermore, it is demonstrated in [6] that the requirement to recover the complex-valued object is that $2^{1/2}$ in each dimension for a 2D square object, and $2^{1/3}$ in each dimension for a 3D square object are enough in principle.

- *Phase retrieval iterative algorithms*

To find the unique solution of the set of equations from eq. (4) one can use a phase retrieval algorithm. It starts from an initial guess with a random phase $\phi(k)$ applied to the Fourier measured magnitude $|F(k)|$. This gives a complex Fourier transformation value $F'_n(k) = |F(k)|\phi_n(k)$. An inverse Fourier transformation is applied to enter in the real object domain $\rho'_n(r)$, where another real-space object constraint (outside support region set to zero) is used to create a new object estimation as a current object $\rho_{n+1}(r)$. A direct Fourier transform restitute a new diffraction pattern $F_{n+1}(k)$. However, the magnitude of $F_{n+1}(k)$ will not be conform to the measured one $|F(k)|$. Therefore a Fourier constraint is employed so that $F'_{n+1}(k) = |F(k)|\phi_{n+1}(k)$, which is then inverse Fourier transformed to form $\rho'_{n+1}(r)$. The solution is obtained when $\rho'_{n+1}(r) = \rho_n(r)$ that means here $\rho'_{n+1}(r) = P_M P_S \rho_n(r)$, where P_S (the support constraint) is applied during the first set of iteration and P_M (the Fourier modulus support) the second.

Normally this requires a lot of repeated iterations between Fourier domain and real domain projections with 'Fourier modulus constraint' and 'support constraint' respectively.

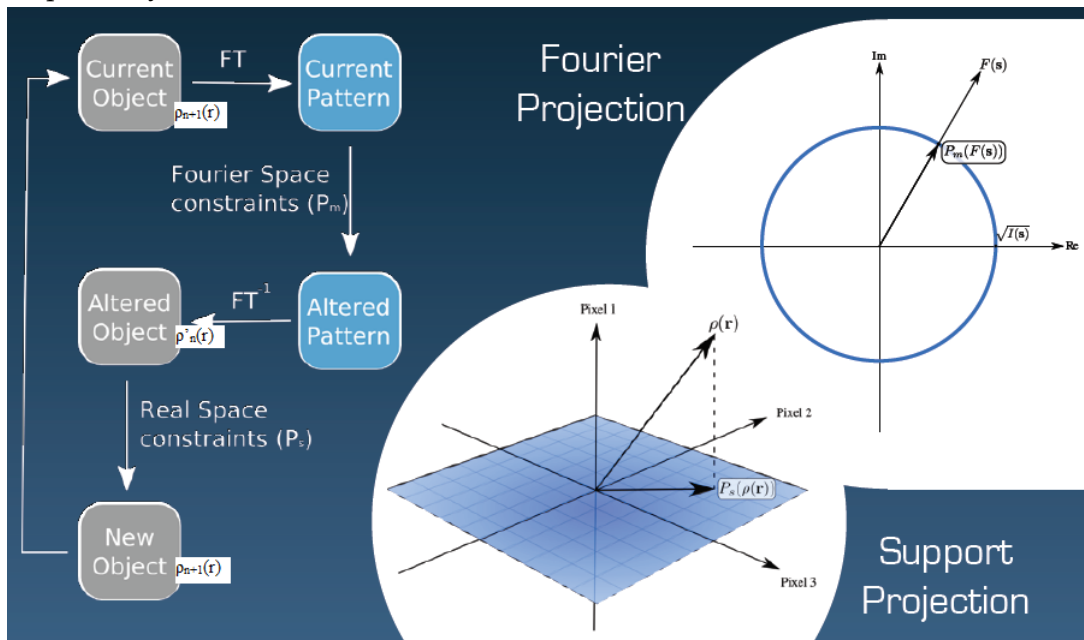


Fig.4.4: scheme of basic phase retrieval algorithms

- *Coherence requirement of the oversampling method*

The oversampling method described in section 2.3.1 is ruled by the oversampling parameter:

$$O = \begin{cases} \sqrt{\sigma} & \text{for a 2D sample} \\ \sqrt[3]{\sigma} & \text{for a 3D sample} \end{cases}$$

σ : total oversampling ratio

The transverse spatial coherence length of the source is defined:

$$\xi_t = \frac{\lambda}{\Delta\theta}$$

where $\Delta\theta$ is the beam divergence.

In the object plane, this needs to be at least larger than the overall object with a largest size of a : $\xi_t \geq O a$, therefore we have the following requirement :

$$\Delta\theta \leq \frac{\lambda}{O a}$$

The temporal coherence length of source is defined: $\frac{\Delta\lambda}{\lambda}$

With a desired resolution of d , the requirement about the temporal coherence can be then expressed as:

$$\frac{\Delta\lambda}{\lambda} \leq \frac{d}{O a}$$

IV.4 The ankylography : a 3D single view imaging technique

Usually, multiple views are requested for full 3D structure identification or image formation. However, under certain circumstances, 3D information from a single view is enough and available in the diffraction pattern.

IV.4.1 Principle of the effect of the Ewald sphere curvature on the 2D projection reconstruction

In a real physical case, a 3D object in a single view produces one 3D Ewald sphere. This sphere is projected (inverse gnomonic projection) onto the 2D planar detector (a CCD camera in our case). How to reconstruct 3D object using this measured 2D diffraction pattern?

First, the capability of retrieving 3D information will depend on the depth of the 3D object. If the depth is small, the information will be available below a limited zone in the detector plane. This limited zone can be surrounded by highest spatial frequency.

Out of this zone, there is a large artifact in high frequency accuracy between the recorded data and the true value located on the Ewald sphere shell. This limit is given by the following formula [1]:

$$D < \frac{\lambda}{2NA^2},$$

Where D is the maximum thickness of object, which should be less than a depth of focus DOF (analogy to a lenses based imaging system) and $DOF = \lambda / 2NA^2$. And here the numerical aperture NA identifies the highest scattering signal that the detector can collect, $NA = k_{x,max} \lambda$. Its calculation is based on the half-width of the square rather than the diagonal.

According to the oversampling ratio principle, an object of finite thickness D will have a coherent diffraction pattern with a speckle width of $1/(2D)$ in the longitudinal direction (along the normal view of the object). If the Ewald sphere surface substantially cuts through a speckle centered at $k_z = 0$ (also called Ewald departure) at the highest transverse frequencies, the value on the Ewald sphere shell will be equivalent to the two dimensional planar diffraction intensity at the $k_z = 0$ plane. We can consider an object to be thin or $2D$ if the Ewald departure is no more than half the longitudinal speckle $1/(4D)$. (see Fig. 4.5): $k_z < 1/2(1/(2D))$. This means that a two dimensional image projection reconstruction of a 3D object is valid only when the object thickness is less than the depth of focus of the imaging system. This is one restriction of the ankylography imaging technique.

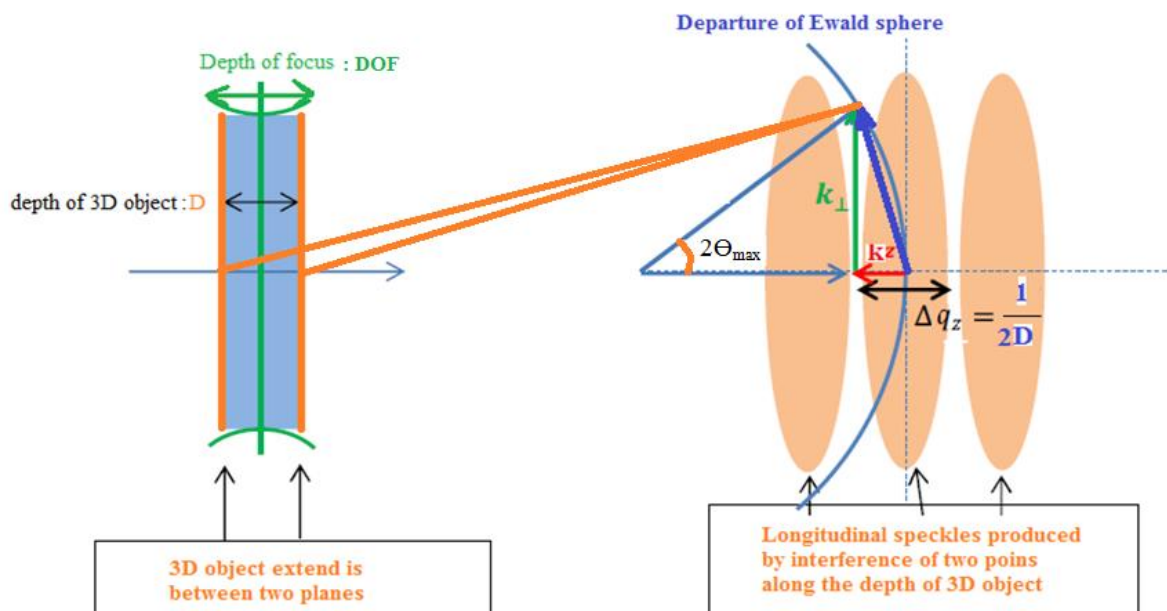


Fig.4.5: Available 2D projection image reconstruction of a 3D object by a single Ewald sphere, and the data on the Ewald sphere shell is equivalent to the 2D plane at $k_z=0$ in reciprocal space.

In addition, when the projection reconstruction of a 3D object by a planar detector is valid, a low pass filter applied to the planar diffraction pattern gives the lowest reconstructible theoretical resolution d_x . This resolution will limit the depth of view of an object of thickness e according the following relation: $e < 2d_x^2\lambda$.

However if the thickness is too large so that the near center speckle is too thin, the Ewald sphere curvature cuts no longer one single speckle along z (beam direction) axis. In this condition, the 2D projection reconstruction from the direct 2D detector measured data is no longer valid. Several rotations of the object or the beam are requested to accomplish all the 3D diffraction pattern assembly. The 3D image is then reconstructed from the whole 3D Fourier assembly of the projected 2D images [1].

IV.4.2 Ankylographic reconstruction

Before investigating ankylography, we need to check its feasibility. Compared to 2D CDI, ankylography has more restrictions. To perform an ankylographic 3D reconstruction, the planar diffraction pattern needs to be projected onto the Ewald sphere. As analyzed above, the departure of Ewald sphere has to fit close to the 2D planar plane at $k_z=0$ in the reciprocal space to ensure a 3D reconstruction. From fig.4.6, one can see that with different distances between the object and the detector plane, the Ewald spheres evolve with different circles radius centered at the position of the object. Therefore, each experimental configuration will have a given oversampling ratio and Ewald sphere geometry.

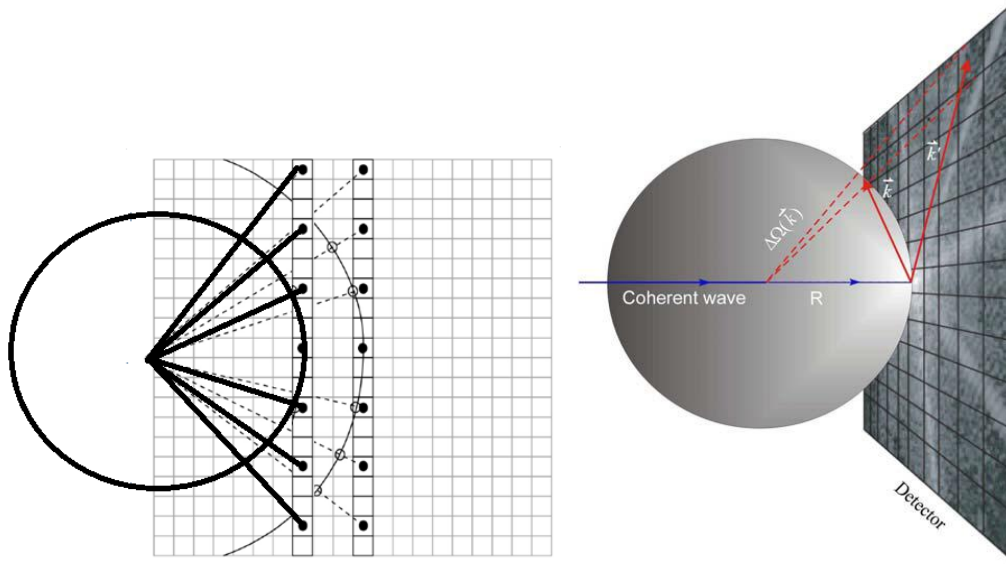


Fig.4.6: Gnomonic projection: from two dimensional planar detectors onto the Ewald sphere. Left: evolution of Ewald spheres with different distance between object (situated in the center of sphere) and detector. Right: side view of the projection of an oversampled 2D diffraction pattern from a planar detector onto the Ewald sphere.

Each pixel of the planar detector integrates the diffracted photons within a solid angle $\Delta\Omega(\vec{k})$, and this solid angle decreases with the spatial frequency. Before doing the projection on the Ewald sphere, the diffraction intensities have to be normalized as follow:

$$I(\vec{k}) = \frac{I(k)}{\Delta\Omega(\vec{k})}$$

After the normalization, the relationship between vectors on the Ewald sphere and the vectors on the detector plane is given by:

$$k_x = \frac{Rk'_x}{\sqrt{R^2 + k_x'^2 + k_y'^2}}$$

$$k_y = \frac{Rk'_y}{\sqrt{R^2 + k_x'^2 + k_y'^2}}$$

$$k_z = R \left(1 - \frac{R}{\sqrt{R^2 + k_x'^2 + k_y'^2}} \right)$$

where $\vec{k}=(k_x, k_y, k_z)$ is a vector on the Ewald sphere, $\vec{k}'=(k'_x, k'_y)$ is a vector on the 2D planar detector, and R the distance from the sample to the detector.

From the analysis in section 2.2, the points related to vector \vec{k} are located on an irregular 3D grid. Since a regular 3D grid in Fourier space is mandatory for the phase retrieval algorithm processing due to the use of the FFT, we need to interpolate $I(k)$ onto a regular 3D Cartesian grid by using a linear interpolation method.

Details of the interpolation:

When doing the interpolation, there are two steps involved in the process before doing the phase retrieval iterations:

1) **The projection:** each point from 2D plane has to be projected onto the 3D Ewald sphere. Each measured data point in 2D plane detector is a planar pixel, when projecting onto the Ewald sphere, the data is located on a spherical pixel. The solid angle comprising each spherical pixel is equal to the corresponding planar one (shown in fig. 6.b). The spherical shell pixel is smaller than that from the planar detector pixel. Furthermore, at higher spatial frequencies, the surface of the spherical pixels decreases less since the corresponding solid angle is smaller. The sampling on the 2D planar detector is linear with a stable increment in size of detector pixel. However, the sampling on the Ewald sphere shell is non-linear.

2) **The interpolation:** the spherical shell is interpolated to 3D Cartesian grids. Each spherical shell volume pixel (called voxel) is curved in spherical surface with a thickness of one voxel size, which is equal to the pixel size along one dimension. Thus, the spherical voxel is smaller than one grid in Cartesian geometry. When being interpolated into a 3D Cartesian geometry, each spherical voxel of Ewald sphere shell can occupy several parts of different grids or can be just comprised in each grid. Therefore, the value on the position of the 3D Cartesian grid is a function of different spherical voxel values. This interpolation method is similar to [2].

Here we call $w(i,j,\Theta_{m,n})$ the volume overlap factor (or coefficient). The Cartesian voxel (i,j,z) (z is a given coordinate in Fig. 4.7) overlaps with two pixels in which the overlapped regions are in yellow and orange. The volume overlap factor $w(i,j,\Theta_{m,n})$ is equal to 1 when voxel (i,j,z) and spherical shell pixel (Θ,n) are completely overlapped, and 0 when they do not overlap. Therefore, the value on the voxel (i,j,z) can be expressed by $G(i,j)$ (z is a given coordinate):

$$G(i, j) = \begin{cases} \frac{\sum_{\theta_m, n} w(i, j, \theta_m, n) F(\theta_m, n)}{\sum_{\theta_m, n} w(i, j, \theta_m, n)} & \text{when } \sum_{\theta_m, n} w(i, j, \theta_m, n) \geq 0.5 \\ -1 & \text{when } \sum_{\theta_m, n} w(i, j, \theta_m, n) < 0.5, \end{cases}$$

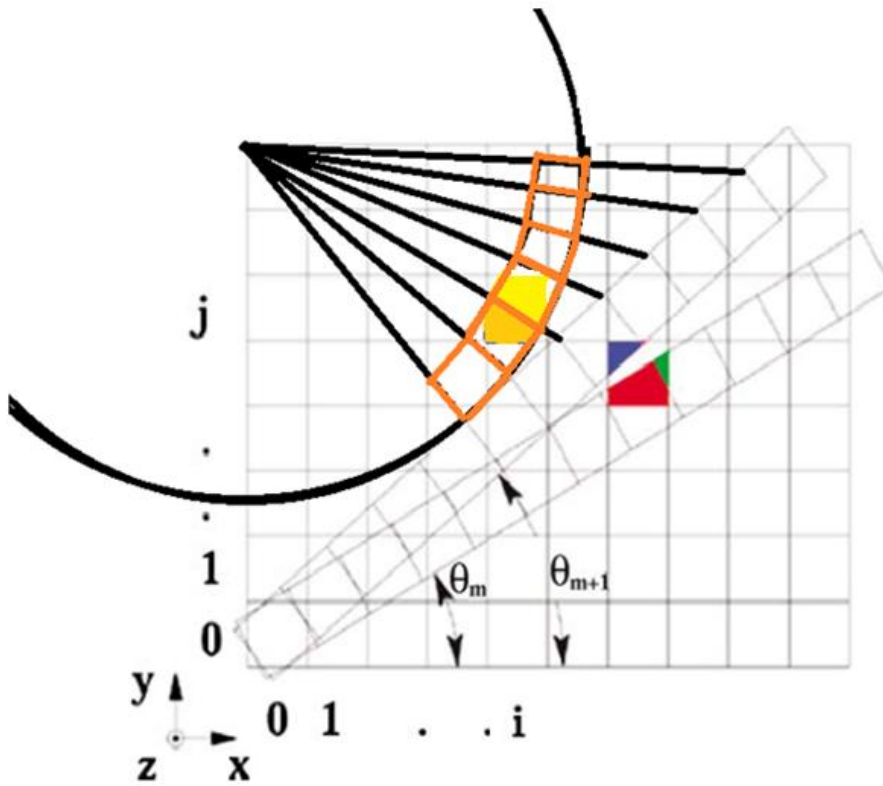


Fig.4.7. Schematic layout of the mapping of a 3D array from a series of diffraction pattern projections, the value on the 3D Cartesian voxel (i,j,z) is calculated from the values of 2 pixels part of which are shown in orange and yellow.

IV.5 First experimental data at the CEA HHG beamline

We have tried some sequences of ankylography measurements with our harmonic beamline at both 32 nm and 20 nm wavelengths (generated in argon and neon respectively). The photon flux and the coherence at 32nm are higher than that at 20nm, however the later presents a better spatial resolution since the wavelength is shorter. Harmonic orders 25 ($\lambda = 32$ nm) or 39 ($\lambda = 20$ nm) are selected by a multilayer coating on the parabola. The alignment of the off axis parabola and the position of its focus are also optimized by the wave front sensor (optimized RMS, highest photon energy in the diffraction limited portion). The focus spot size of the soft X-ray beam on the sample is then equal to $5\mu\text{m}$ in diameter, with 5×10^8 photons per laser shot at $\lambda = 32$ nm. This is a critical parameter in SNR analysis in which it shows the linear relation between the SNR and the incident photon intensity. The focal spot at $\lambda = 20$ nm has a diameter of 3-4 μm and a total photon number of 10^6 .

IV.5.1 The double grid sample.

The 3D sample is composed of two membranes (each one having the same type as the one used for CDI and HERALDO in chapter III). Each membrane has a “grid pattern” realized using the FIB facility CSNSM laboratory (Orsay) after assembling the two membranes at a distance of about $2\mu\text{m}$ (see Fig. 4.8).

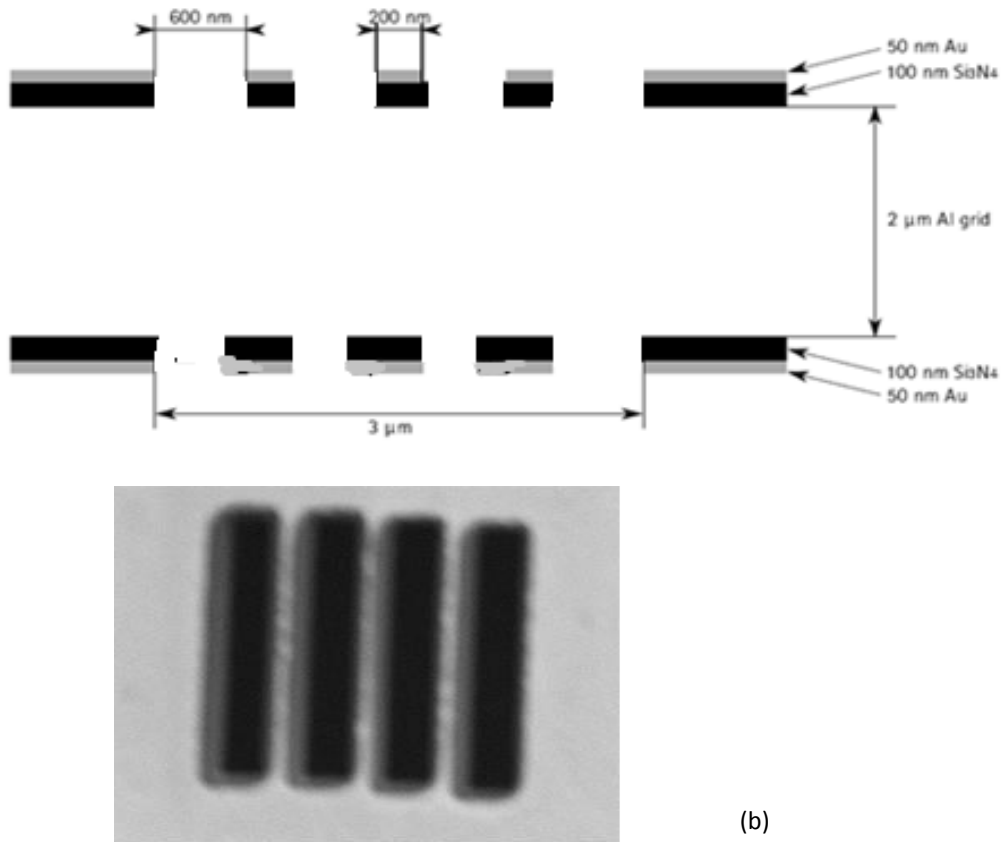


Fig. 4.8.Up: Double grid sample geometry. Each grid plane is composed of 100 nm Si_3N_4 layer with a 50 nm gold layer. The transmission is in the order of 10^{-3} . Down: MEB image of the sample.

Simulations of the 3D reconstruction:

The phase retrieval code that we have used has been developed by the group of Prof. J. Miao at UCLA. I did most of the calculation during a 1 month stay in their group. The first idea was to validate the 3D image reconstruction from our sample using a single 2D planar diffraction pattern image.

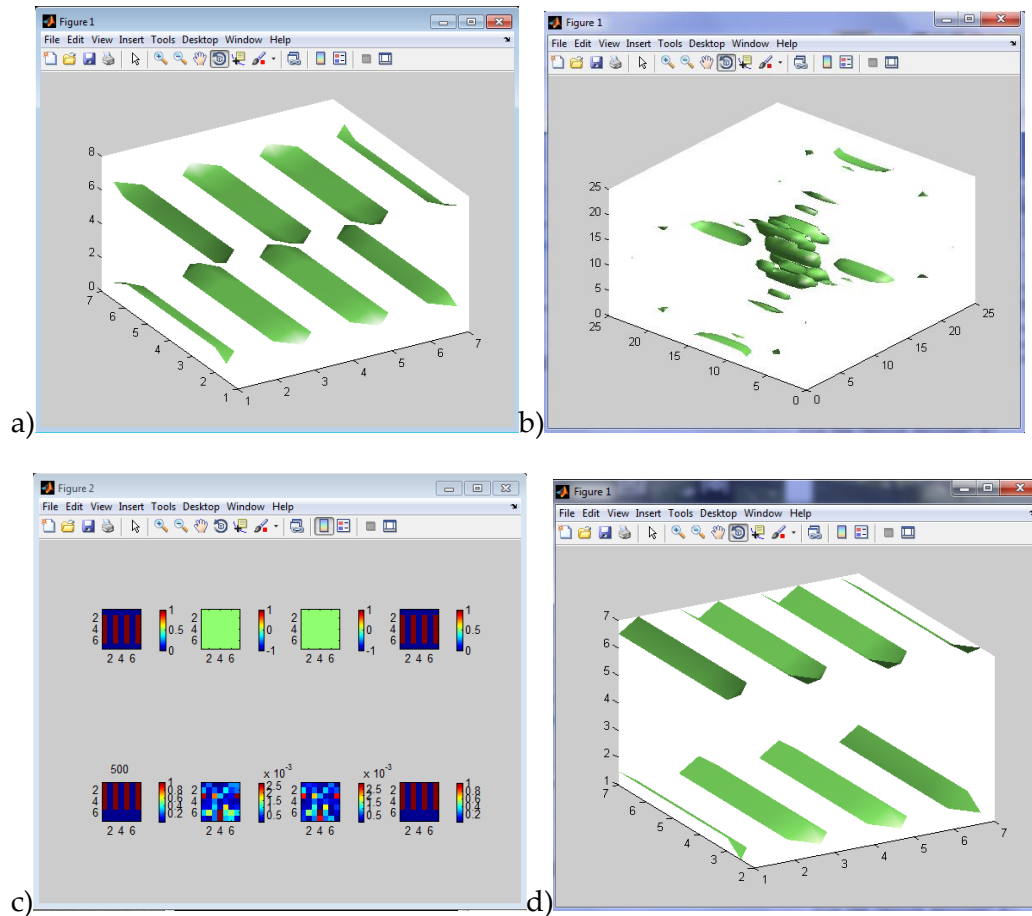


Fig 4.9. Simulation of the double grid sample (two membranes). a) 3D object representation b) Simulated 3D diffraction pattern from the object in (a). c) Reconstruction result panel extracted from the code using the diffraction data in (b) d) 3D ankylographic image reconstruction showing a very good accuracy compared to image shown in (a).

The object is an odd cubic 3D object of which the width, the length and the depth are the same ($7 \times 7 \times 7$). The figure above shows the simulation with the object which has two membranes. In fig.4.9.a top and bottom green color part presents the vacuum part of the object where the incident X-UV harmonic beam light can go through. The transparent part (white area) represents the membranes that block the incident light). The 3D diffraction from the object has been simulated and is represented in Fig. 4.9.b. In fig.4.9.d, the top line review the top layer of the 3D two-membrane composed object, the bottom line shows the reconstruction after 500 iterations by HIO algorithm for the 3D reconstruction. At the same time, we can see that the space between the two membranes has no reconstruction since the value is obviously below 10^{-3} . Therefore the depth information is well retrieved. This proves the great ability of ankylography to reconstruction the depth information of 3D object. From this simulation, we obtain the successful 3D ankylographic reconstruction with just 500

iterations. This is a good proof for the design of our test 3D object and it also gives confidence in the 3D ankylographic reconstruction.

First measurements and reconstruction

Fig. 4.10 presents the first test configuration that I have used at the HHG beamline. The data are collected at a wavelength of 32 nm in 5 shots. The samples are placed on a rotation stage to obtain different observation angles since the incident beam's direction is fixed.

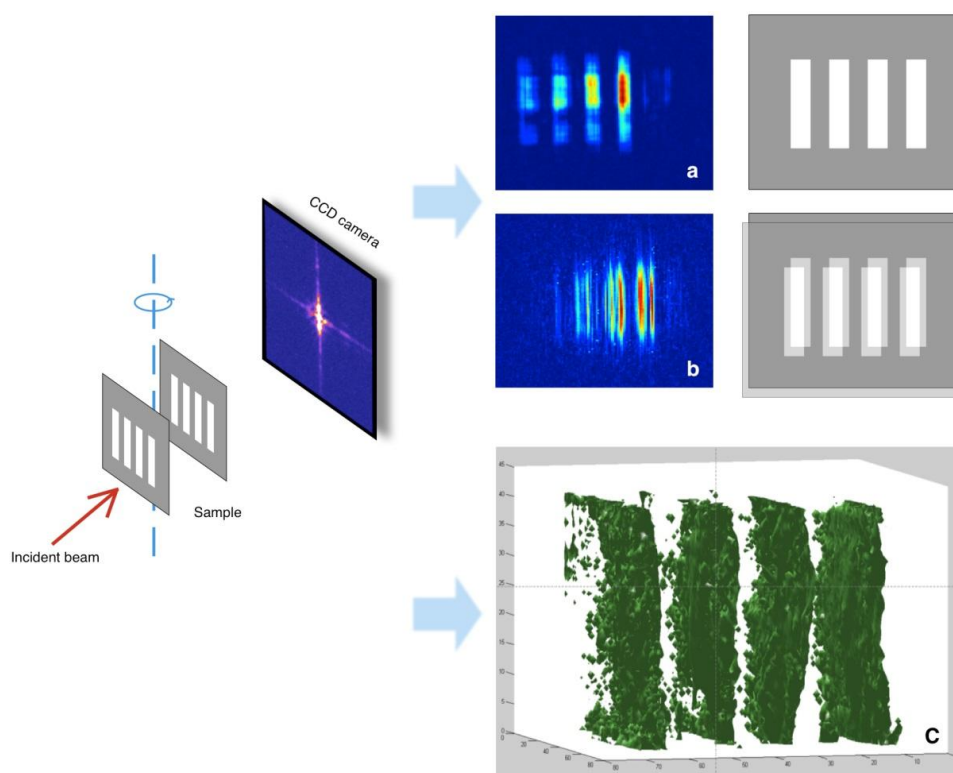


Fig. 4.10. Experimental scheme for ankylography imaging. a) 2D CDI image reconstruction for 0° angle (sample normal to the incident beam). The grey grid shows to the effective position of the double grid. b) 2D CDI image reconstruction for 7° angle (with the normal to the sample). c) 3D image reconstruction. We show in green the photon flux.

Single shot was not possible as the signal was too low. To increase the signal to noise ratio in diffraction pattern acquisition in single shot, we configured in detector parameters with a readout frequency of 100 kHz (minimum of readout detector noise) and within a window size of 600×600 pixels of 2×2 binning ratio (corresponding to 1200×1200 non binned pixels). The hardware binning used here can increase the detected scattering signal without sacrificing the oversampling ratio requested in ankylography and the spatial resolution. Fig. 4.10 (a,b) are CDI

reconstructions of two diffraction patterns taken at observation angles of 0° and 7° respectively. The first one indicates well-aligned grids, while the second one is totally different. Indeed, at 7° the slits of the forward membrane are partially covered by the backward membrane. Fig. 4.10.c is the ankylography reconstruction of the diffraction pattern taken at an incident beam angle of 0° . The green part of the reconstruction indicates the double grid volume where photons went through the membrane, which reconstruct the shape of the slits on two membranes. The ankylography reconstruction was performed by the group of J. Miao at UCLA. Fig. 4.11 presents different views of the reconstructed image. The spatial resolution along the z axis (depth) is of 200nm and 70nm in the lateral direction. Since our signal to noise is low at high frequencies, the reconstruction of the object cannot achieve a very high spatial resolution. The phase retrieval requires a powerful computer cluster for 3D phase retrieving calculations. The algorithm processing takes several hours. This is one major disadvantage of ankylography: it is not possible to run a reconstruction process on a standard PC. The convergence of the phase retrieval has not been straightforward. The initial parameters have to be set carefully. In particular one has to set to the order of magnitude of the object thickness so that the voxel size is correctly matched. This is another constraint.

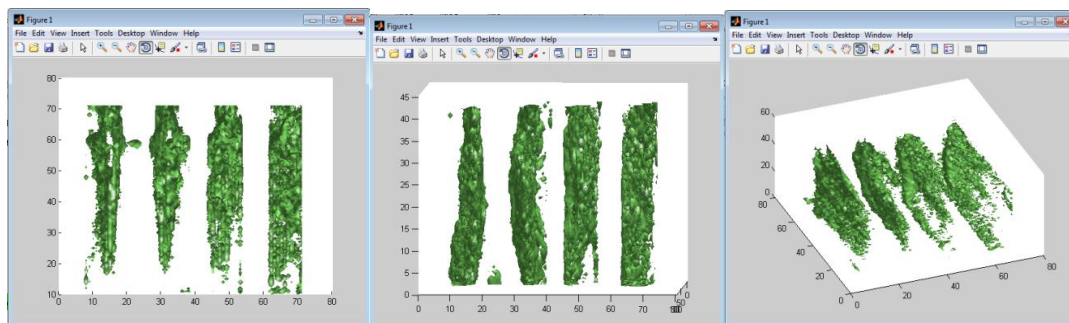


Fig.4.11: Different views of the 3D reconstruction from left to right:Top, lateral and side angle views.

IV.5.2 The “light” sample.

I have tested another 3D sample which is shown on Fig 4.12. To design this object we incline a 2D object in X-Y plane from the membrane plane. We open the 2D plane by a controlled angle to produce different kinds of 3D object with different depth information along optical axis. The Chinese character “light” has been patterned using a focused ion beam (FIB). The silicon nitride membranes are supported by silicon substrate on one side, which defines the membranes aperture varying from $150 \times 150 \mu\text{m}^2$ to $500 \times 500 \mu\text{m}^2$ with a thickness of $100 \mu\text{m}$. On such large window, we can fabricate more than 100 test objects in one membrane. Before etching, the

membranes are covered by a gold layer (around 50 nm thick). The membrane transmission efficiency is less than 1.5×10^{-3} (CXRO database) for the 25th harmonic (wavelength of 32 nm). This layer removes the direct beam and ensures that we have a pure amplitude object for our imaging tests. The 3D test objects are etched from a 2D object by generating a nano-door around the pattern as shown in Fig. 4.12.

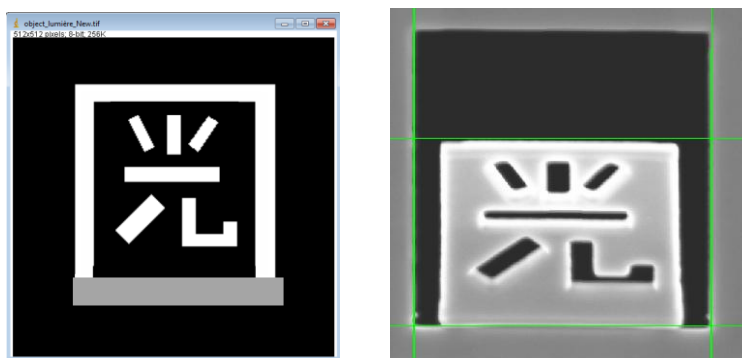


Fig 4.12: Left: picture of the JPG image used as an input for the FIB patterning. The white area corresponds to a high ion dose irradiation zone creating a total hole on the membrane. The grey area: partial ion dose, few 10nm layers are removed allowing the door to be opened. The control of this dose allows opening more or less the door. The black area: zero dose. Right: SEM image of the 3D sample created from opening a 2D object to 3D by controlling the dose in the grey area seen on left side picture. The Chinese character means 'light' in English.

Simulations:

The object size in the X-Y plane is chosen in such a way that it respects the oversampling ratio requested for 3D coherent diffractive imaging. We insert this 3D object into a cubic volume to simulate the diffraction pattern by a simple 3D Fourier transformation. We have to pay attention to the impact of the thickness of the layer (thickness of the membrane). For example, we generate a 3D object with a total width and length of 80x80 pixels in the X-Y plane (513x513 pixels) and with a layer thickness of 1 pixel. After rotating the X-Y plane with respect to the membrane plane by an angle of 15 degree, the object occupies around 20 pixels along the Z axis. Thus, a cubic volume is generated (513x513x513), the center of which is the center of this 3D object with a size of 80x80x20.

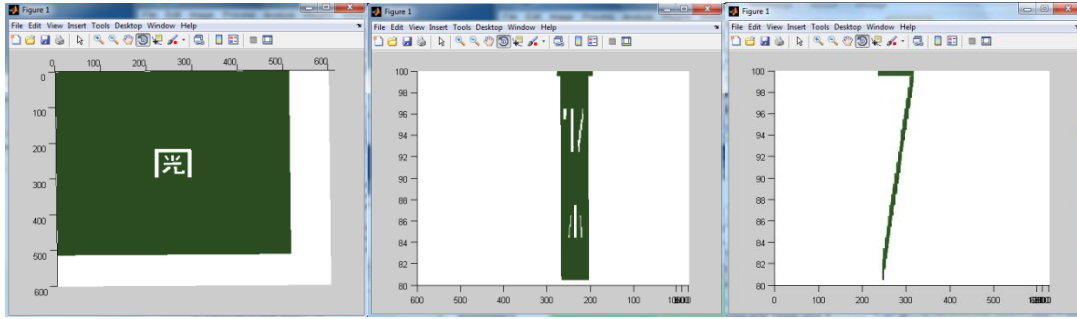


Fig. 4.13. Different views of the simulation object, from left to right: View in X-Y plane (one pixel of layer thickness), view in X-Z plane, and view in Y-Z plane. From Y-Z plane, we see here that the rotation angle is around 15° .

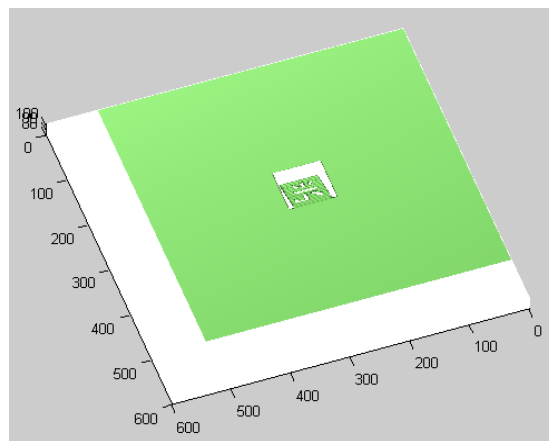


Fig. 4.14 3D view the data used as an input in the Matlab code. The object is an amplitude object. The color in green represents the membrane that blocks the beam, thus this value is equal to 0. The white part is equal to 1 with a transmission of 100%..

Fig. 4.15 shows the 2D planar diffraction pattern evolution as a function the out of plane rotation angle. They are shown in the same contrast and color code. From the 2D planar projection, we can see that the central part signal is smaller when the rotation angle increases. More interestingly, we see that the sphere projection onto the 2D plane is more and more obvious since the depth increases when the rotation angle increases. The diffraction lines are not anymore straight in some areas of the diffraction pattern. This illustrates the effect of the projection of the 3D Ewald sphere on a 2D detector plane.

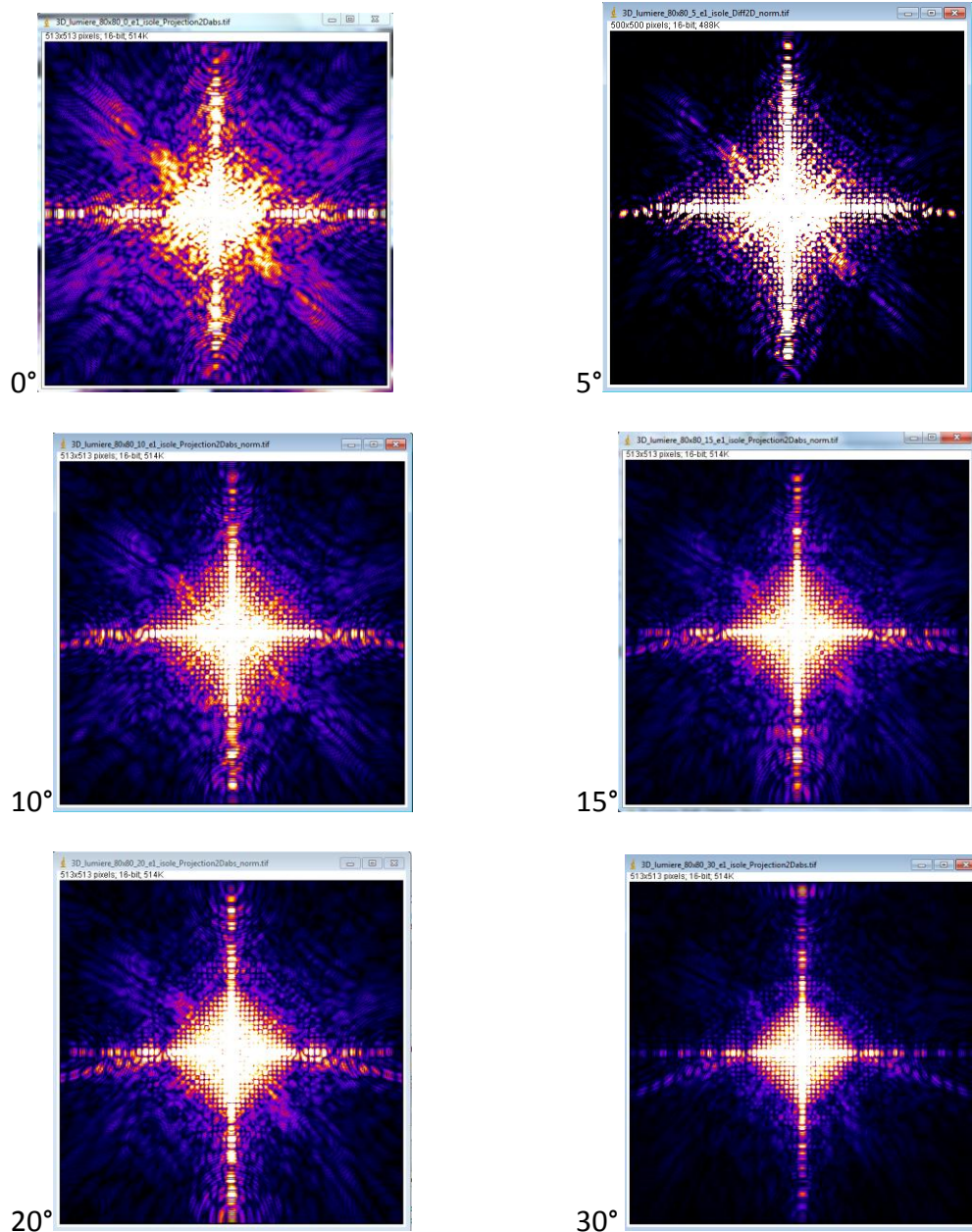
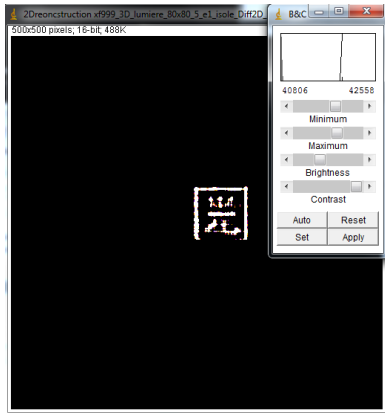
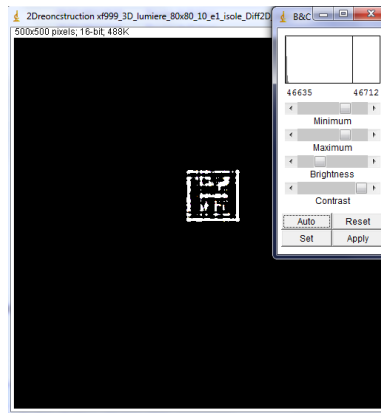


Fig. 4.15: 2D diffraction pattern for different rotation angles varying from 0° 5° 10° 15° 20° 30°.

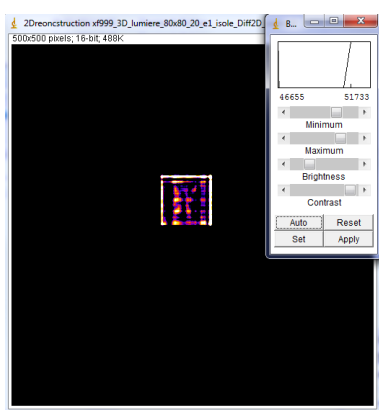
3D Ewald spheres can be then generated from the 2D projection with a thickness of 1 pixel. The result for different rotation angles of the 3D object are presented in Fig. 4.16.



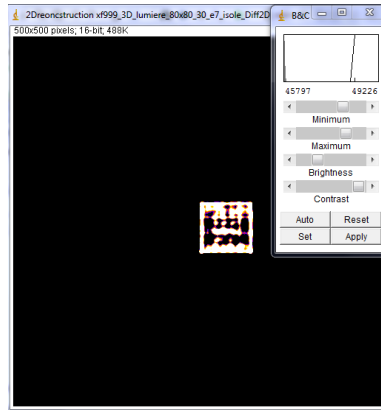
5 degree



10 degree



20 degree



30 degree

Fig. 4.17: 2D image reconstructions using the “Pierre Thibault” phase retrieval code for different rotation angles varying from 5° , 10° , 20° and 30° . The input data are the 2D diffraction data presented in Fig. 4.15.

We see in the images presented in Fig. 4.17 that the 5 degree case fits with the planar approximation. We obtain almost the same quality of image reconstruction as for the pure 2D case. At 10 degree, we can still identify the reconstructed 2D pattern but with already a strong loss of information. When the rotation angle gets larger, the 2D projection reconstruction is not correct as the Born approximation fails and the image is altered.

From these simulations we conclude that the connection between 2D and 3D space is restricted to low angles. This will limit the 2D reconstruction when the object has a too extended 3D structure. Additionally, the 2D data projection on the Ewald sphere will lose some 3D information if the sample is too extended in 3D (wide open angle in the case of the “opened door” sample).

Experimental results:

The simulations have discussed the validity of the projection from a 2D diffraction pattern to the Ewald sphere but also the limitation of a 2D reconstruction when the object stays out of the Born approximation (object too thick). We present in this section the first results of the single shot ankylography campaign. The data have been collected at the LUCA high energy beamline at 32nm (25th harmonic generated in argon) and at 20nm (39th harmonic generated in neon).

a) $\lambda = 32\text{nm}$ data:

Fig. 4.17.a shows a SEM image of the sample. The total size of the square is $3 \times 3 \mu\text{m}^2$. The Chinese pattern “light” is included in a plane tilted by 5° with respect to the membrane plane.

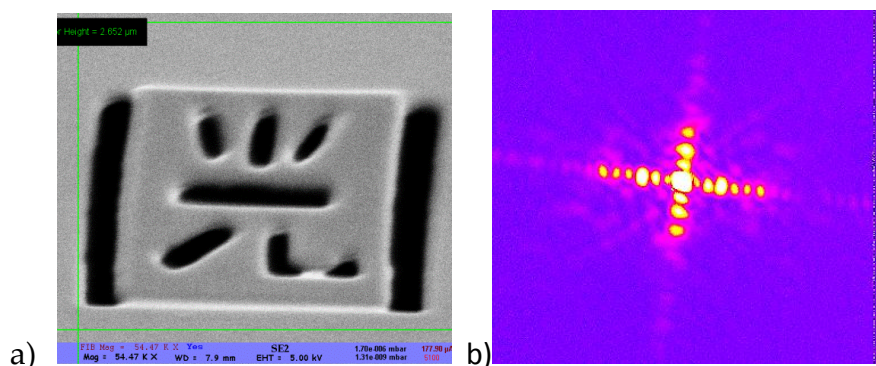


Fig. 4.17: a) SEM image of the sample. b) Single shot diffraction pattern.

The sample is illuminated at a wavelength of 32 nm using the same experimental setup reported in the CDI chapter. The diffraction pattern measured in single shot is shown in Fig. 4.17.b. It is well contrasted and presents many features related to the geometry of the object. A clear one is the two main directions corresponding to the diffraction by the edges of the gate surrounding the object. We then compute from the measured diffraction pattern the autocorrelation (see Fig. 4.18) which will create the object support used in the CDI reconstruction code.

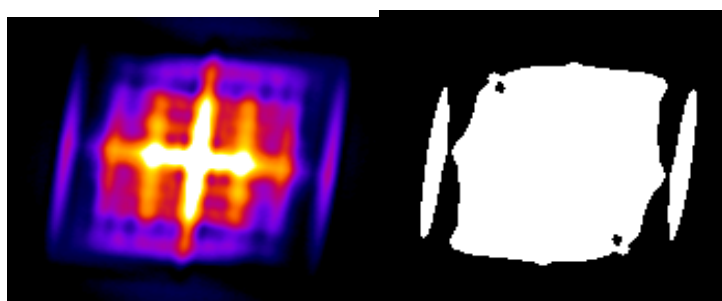


Fig. 4.18: Left: Autocorrelation of the measured diffraction pattern. Right: Effective support used as an input in the phase retrieval code.

As show in Fig. 4.19, the phase retrieval converges quite fast. We obtain an image after about 50 iterations. The final reconstruction is shows in Fig. 4.20.

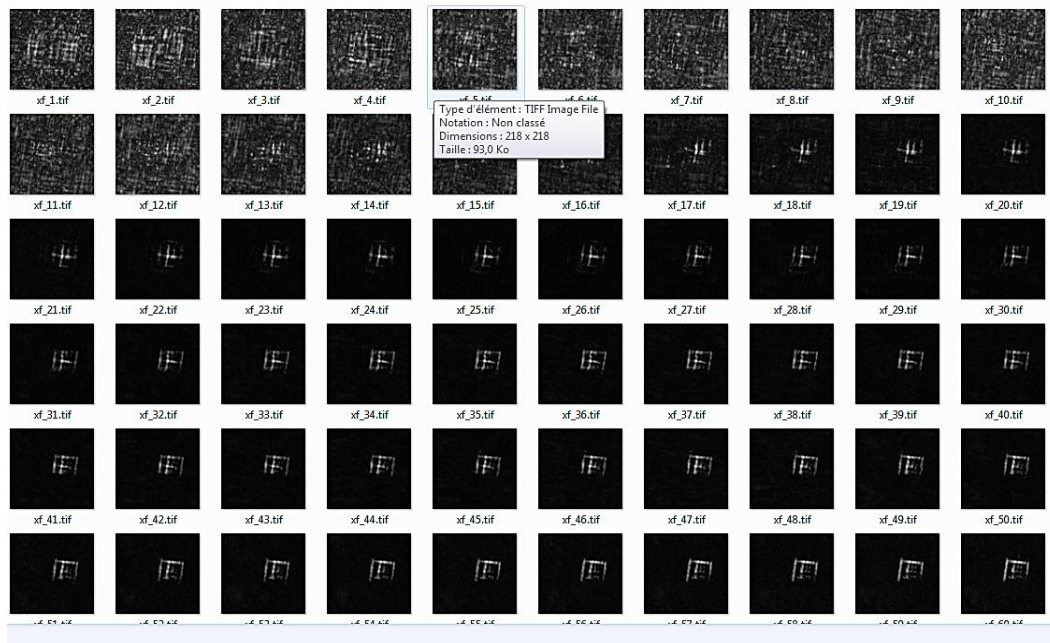


Fig. 4.19: Iterative process from the first iteration (up, left) to the 60th. The convergence is obtained after 50 iterations (down, right).

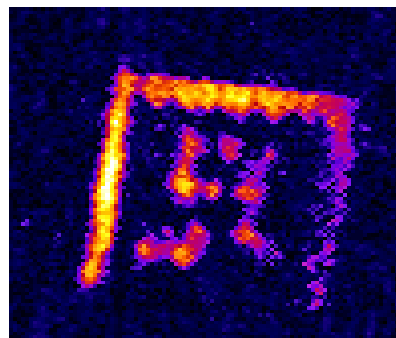


Fig. 4.20: Reconstructed image from the measured diffraction pattern.

The second step is to start a 3D reconstruction from this data. The spatial resolution along XY is about 200nm and 600 nm along the depth direct (Z axis). This is not enough to run an ankylography reconstruction as the object is not resolve in depth. Indeed, the large diffraction angle do not respect the born approximation and will not be correctly projected onto, the Ewald sphere. To circumvent this issue we have several options, either changing the sample geometry or the soft X-ray wavelength.

b) $\lambda=20\text{nm}$ data:

We have performed the same experiment using the 39th harmonic, at a wavelength of 20nm. The signal being lower, we had to accumulate over 20 shots. The object has almost a 30 degrees opening angle (Fig. 4.21.a). The diffraction pattern is shown in Fig. 4.21.b. We see a curved diffraction line arising from the interference between in and out of plane diffracted light. This is a clear signature of the 3D geometry of the sample. The 2D reconstruction is shown in Fig. 4.21.c. We can identify the square shape of the gate but the details of the object cannot be really resolved. This is clearly due to the failure of the Born approximation because of the large opening angle in the Z direction.

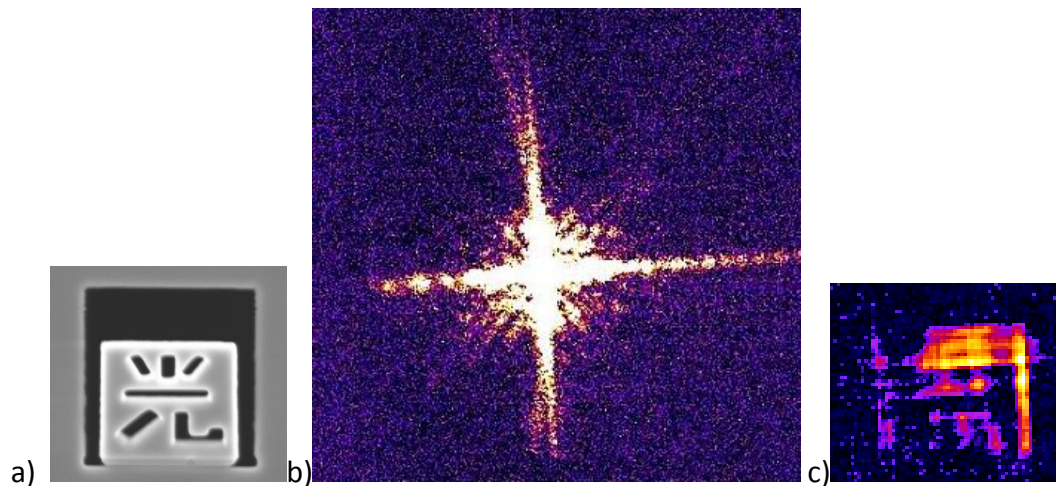


Fig. 4.21: a): SEM image of the sample showing the 30° opening of the gate. b): measured diffraction pattern. c): Reconstructed image.

We have then processed the data for a 3D reconstruction. The projection onto the Ewald sphere is shown in Fig. 4.22 with different views. The data are then processed for the 3D ankylographic reconstruction. However, after many attempts with various parameters, we have not obtained a satisfying image. A partial result is shown in Fig. 4.23. One of the problems is that three dimensional structure determination using single view diffraction imaging data has restriction. In particular a dimensional deficiency limits the applicability of ankylography to objects that are small-sized in at least one dimension or that are approximately two-dimensional in some other way. This was already observed in the simulations presented in the first section. In our case, the 30° opening of the gate make the sample a full 3D sample in 3 directions. The rate of reliable information transfer is limited by the degrees of freedom available and by the signal to noise ratio. In our case, increasing the signal would not improve the reconstruction capability. The restriction is imposed by the large angles involved in the sample geometry. Through oversampling the spherical diffraction

intensities, ankylography can reconstruct the 3D structure from a single view only if the physical constraints are strong enough. Compared to coherent diffraction microscopy (or coherent diffractive imaging), the phase retrieval problem in ankylography is in principle more difficult to deal with. The reason is related to the facts that the distribution of singular values decays fast. This has also been seen the simulation. The conclusion of this very preliminary experimental campaign is that ankylography has strong applicability restriction. It cannot be applied to a full range of sample geometry. In particular, ankylography works well if the 3D object is restricted in the depth dimension.

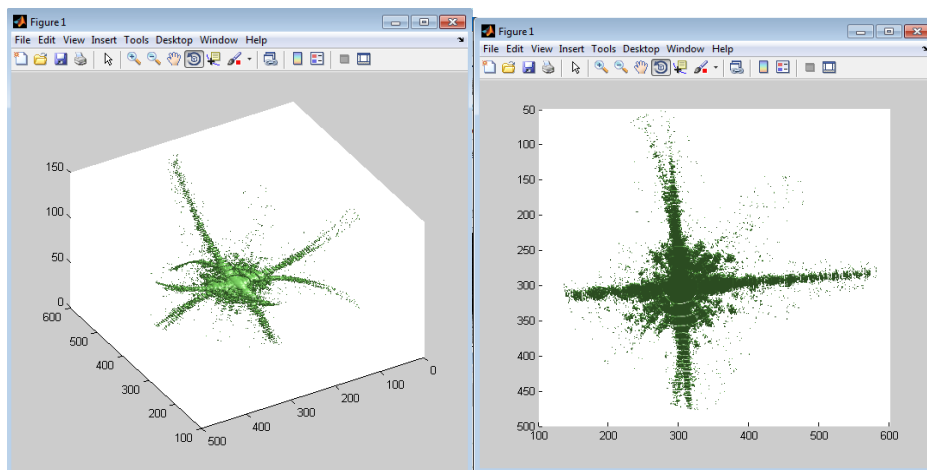


Fig. 4.22 : Projection onto the Ewald sphere from an up-oblique view (left) and lateral view (right).

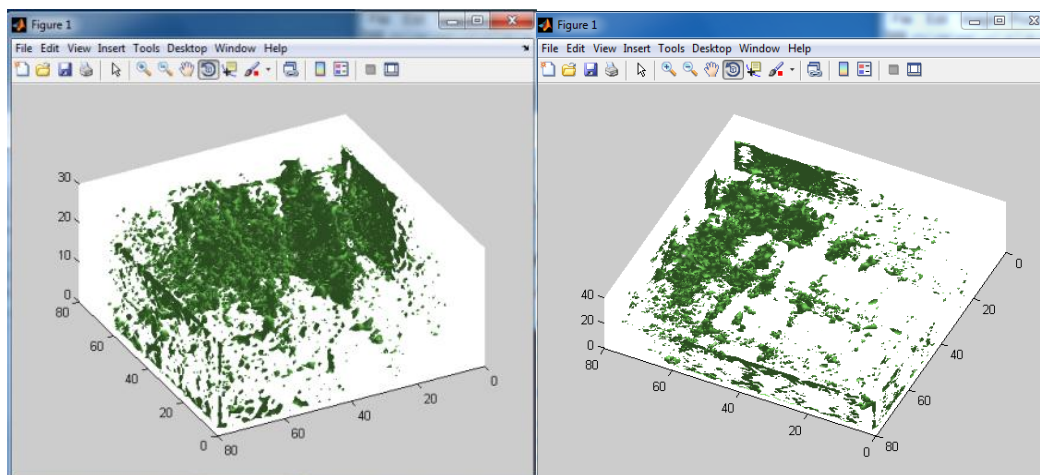


Fig. 4.23: Ankylography image reconstruction from projection data shown in Fig. 4.22.

IV.6 Conclusion

A single view named 'ankylography' has demonstrated a good potential for future single shot 3D coherent imaging [3; 10-16]. Based on the analysis above, I've pushed our 2D imaging towards 3D coherent imaging. At the same time, the optimization of harmonic beamline in our group allows to achieve a high coherent beamline down to 20nm. Our numerical simulations suggest that ankylography works well for small 3D objects in 7x7x7 voxels. However, the signal to noise in the experiment is not good to obtain a correct ankylographic reconstruction as shown in the simulations. As ankylography is such a new complicated idea, it is certainly impossible for us to envision and address all the problems. In order to fully understand the potential and limits of ankylography, follow-up studies are still needed in theory, experiment and algorithm development. Ankylography, which recovers 3D structure information from oversampled diffraction intensities on the spherical shell, can detect the depth information signals from the very high spatial frequency zone compared to CDI. The projection from 2D planar CCD to 3D spherical shell needs more complicated applied mathematical knowledge. Different algorithms for this projection lead to almost different 3D sphere volumes before entering iterative into the 3D full reconstruction process. From some numerical simulation and experimental data, we can see that increasing the shell thickness can improve both the ankylographic reconstruction and 2D projection image reconstruction for larger 3D object (it means larger opening angle for pseudo-3D object). However, the photon flux in 20nm is less than 32nm, the signal to noise is worse, thus this decreases the quality of the reconstruction. Even though our harmonic beamline optimized until 20nm shows good coherence for coherent imaging.

Chapter V -General Conclusion and Perspectives

The objective of this thesis work is to develop and analyze the coherent imaging techniques using XUV high-order harmonic beam. SNR implication in image reconstruction has been deeply studied as well as perspectives in 3D imaging.

The theoretical background of the coherent imaging (or lens-less imaging) is presented in the first chapter from the image formation in the Fraunhofer diffraction regime to the different reconstruction processes of CDI, FTH and HERALDO. The two main branches of lens-less imaging, CDI and holographic techniques, have their own advantage. The latter provides quick, direct and non-ambiguous reconstruction

of the object, while the iterative algorithms usually converge to reliable solutions after thousands of iterations. However, the need of a proper reference in holographic techniques limits the application in cases that reference fabrication is technically difficult or not possible. In both reconstructions, the coherence of the light source is the key factor, deciding whether the phase information can be retrieved or not from the measured diffraction pattern. Since different kinds of noise are introduced during the detection, the signal-to-noise ratio of the diffraction pattern is another key factor, deciding whether reconstruction algorithms can extract or not the effective signal from the noise. High-order harmonic source, which I used during the thesis work, is intrinsically qualified for the coherent requirement and is able to deliver high flux beam thanks to the recent development of the HHG scheme. Compared to free electron laser facilities, HH sources are compact and inexpensive, and offer easier access and more beam time for users.

Chapter II introduces the historical research work and progress of the beamline, which provided a 25th harmonic beam (wavelength of 32 nm) and achieved 120 nm spatial resolution in CDI reconstruction of a test object from single-shot acquisition in 2009. This encouraging first lens-less imaging demonstration led to open questions about the CDI and the harmonic beamline, which has been one of the starting point of this thesis work. A complete discovery of the harmonic generation quality has been carried out to understand the harmonic beam behavior under different generation conditions. This resulted in optimization at each stage of the beamline, and standardized the harmonic generation for future experiments to avoid the large instability of the beam quality. The two beam characterization methods (XUV wave front sensor and Young's double slits) provide various information such as the wave front quality, the beam flux, the spatial coherence and the reconstructed harmonic focal spot profile. HHG parameters are optimized for a good compromise between the triple key factors: the coherence, the beam flux and the wave front quality. CDI reconstruction analysis of the interferogram of the Young's double slits confirmed the coupled influence of these beam properties. The optimization of the IR pump laser is realized by a laser modal filtering system. The IR laser presents a quasi-Gaussian beam after the propagation in hollow core fiber, which improved the HHG efficiency by a factor of 2.5 in Argon and 6 in Neon. In addition, the filtered laser beam position is stable that ensures a continuous high HHG quality during long time experiment.

The harmonic beamline enhancement has improved the reconstruction ability of the imaging techniques. Chapter III presents the demonstrations of CDI and holographic imaging techniques, followed by quantitative analysis. In the CDI section, reconstructions have achieved sub-80 nm spatial resolution from single-shot acquisition, which is $\sim 2.5\lambda$ ($\lambda=32$ nm). Coherence requirement for CDI has been

discussed using Young's double slits that the phase retrieval algorithms are not converging for a contrast of interference fringes lower than 0.5. The importance of the coherence has been again demonstrated in the FTH reconstructions of a geometry grid test sample, in which different components of the grid are respectively missed in two independent reconstructions associated to two pinhole references. However, another diffraction pattern of the same sample with lower diffractive signals provided well-resolved reconstructions. The compromise between the beam coherence and the beam flux is the main issue for lens-less imaging. HERALDO configuration can amplify the diffractive signal of the object by extended references and uses "mathematical tricks" to overcome the resolution limitation imposed by the reference size. Step-by-step analysis of the reconstruction process shows the significant influence of the readout noise, which is amplified by the HERALDO operator in Fourier space. A low-pass filter is the solution to overcome this main obstacle in our reconstructions. Meanwhile, detection stage optimization has been discussed, which is valid for all the coherent imaging techniques. The comparison between FTH and HERALDO showed that HERALDO with a slit reference is the best holographic configuration for our harmonic beam, since we are mainly limited by the beam flux in single-shot regime. The comparison between CDI and HERALDO confirmed the effectiveness of the signal amplification by extended reference. It is not possible to say one is better than the other without a given experimental condition. CDI and HERALDO are not only alternative but also complementary to each other. Choice of the imaging technique for a concrete application should base on careful analysis of the experimental conditions.

The development of a versatile harmonic beamline, which is now a standardized, stable and powerful beamline providing harmonic beams of high coherent, photon flux and wave front quality, with tunable harmonic wavelength. Combining with the CDI, HERALDO, our high flux harmonic beamline is suitable and ideal for a wide range of applications from physics to biology. We foresee a bright future for ultrafast dynamic studies with real space reconstructions of nanometric spatial resolution.

The last part of my thesis work has been dedicated to extending 2D to 3D imaging. Ankylography has shown a remarkable performance and is a promising imaging method for 3D single shot coherent imaging by single view in some circumstances. This can prevent the sophisticated request for precise tilting of sample holder which is requested in most traditional 3D tomographic imaging. Using numerical simulations, we have reviewed the limitation of ankylography. The technique can be well applied to thin 3D object. When object are too large we observe that the projections onto the 3D EWALD sphere deviates largely from the Born approximation which leads to systematic errors. The convergence, as shown by the simulation, is then ensured only in restricted conditions. In this case, the algorithm

converges well but still with large CPU computing time which is one drawback of the technique. Indeed, during the ankylographic reconstruction, the 3D HIO iterative process operates along many constraints which prevent from a fast convergence. Even good initial parameters have to be chosen and controlled. The large data volumes request a super-PC to handle the process. In this context, even some preliminary results are shown in my thesis, there is still more space to improve the final 3D reconstruction.

Perspectives in 3D stereo imaging

We propose here to **extend our actual 2D ultrafast nanoscale microscope to obtain 3D images**. Indeed, most samples of physical interest require 3D perception. However, the usual method based on many orientation projections of the specimen suffers from extended exposure time to X-rays which could induce damages. Ultrafast *Single shot 3D stereo imaging* would allow lowering the impact of X-ray exposure in image reconstruction. Moreover, when dynamics are studied, the single shot regime is mandatory: some phenomena are not reversible and solid state samples are often not perfectly reproducible.

Stereo imaging is based on the human eye vision. Our right and left eyes take two 2D images at different observation angles of the object and the brain combines these images to give the perception of 3D depth. It is not a real 3D imaging but already provides much more interesting information about the object than 2D image. Fig. 5.3 presents stereo imaging examples of nanoplankton samples realized by a scanning electron microscope [1]. After taken an image (photos in gray scale), the biological samples are tilted about 5 degrees to take the second image. These two images are then turned into red and green, and combined by the red-green anaglyph method [2]. With red-green glasses, one can see 3D planktons from the combined image. In principle, the stereo imaging is compatible with the coherent diffractive imaging that two CDI or holographic reconstructions at different observation angles are sufficient to make 3D perception.

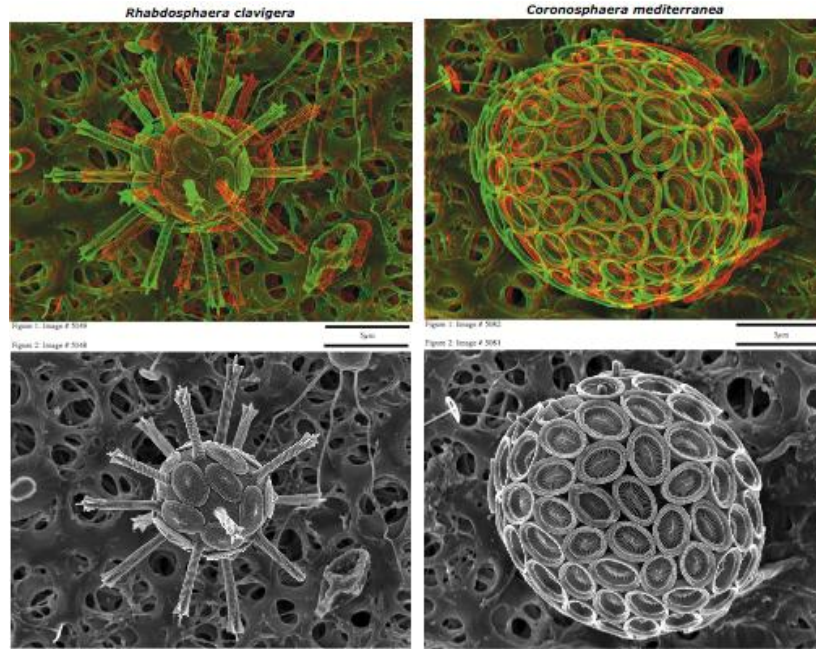


Fig. 5.1 Stereo image (red-green photos) of plankton samples made by digital combination of SEM images (gray scale) taken at different observation angles. Picture extracted from Ref. 1.

I have been working in the implementation of the first single shot stereo imaging using high harmonic generation. The idea is to realize two parallel beams before focusing using off-axis parabola. The separation of the main beam is realized with two grazing incidence silicon mirrors (mirror 1 in Fig. 5.4) before the parabolic mirror. Half of the harmonic beam is reflected and the other half go straight to the parabola. The reflected half-beam is then reflected by a second multilayer mirror (mirror 2) toward the parabola. The two half-beams are focused by the parabola onto the sample. The distance between the two beams is about 20 mm which acceptable for the numerical aperture of the parabola. As the two beams are parallel they are focus at the same point with an angle of $\sim 6^\circ$. Note that in this geometry the two beams are not synchronized. A new setup with a femtosecond synchronization of the two beams is currently under design.

After interaction with a sample the two beams generate two diffraction patterns that are collected by our CCD camera in a single acquisition (Fig. 5.5a and b). The first test object is a 3D HERALDO samples with slit references. We use an up-warped etching process to have 3D depth, with different motif, such as a grid presented in Fig. 5.5c. Since the half-beams have lower flux due to the beam separation and additional mirror reflection, we use the slit references to increase the reconstruction ability. Fig. 5.5b presents a preliminary result of HERALDO reconstructions associated to the diffraction pattern at the top of the acquisition image. Slit references and the borders of the up-warped pattern are well resolved, but the grid motif is not clear. Further

work on the reconstruction is under progress. Further work on biological samples will also be realized.

Time-resolved three dimensional imaging studies that are currently limited by the need for multiple views of the same sample will be then possible. It is expected to get single shot images with 3D perception down to sub-100 nm spatial resolution.

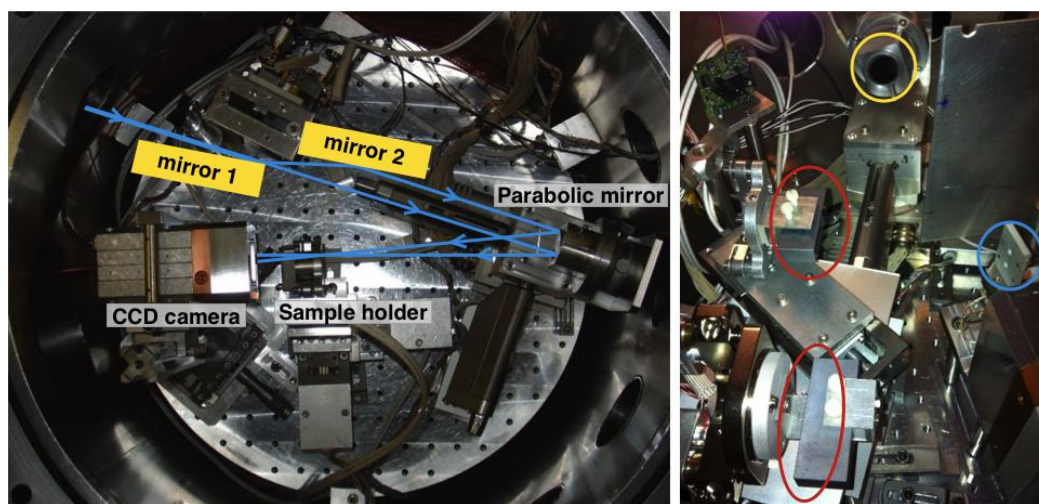


Fig. 5.2 Picture of the experimental setup for stereo imaging. In the left one, blue lines indicate the beam propagation and yellow squares are the silicon mirrors installed for beam separation. The two-mirror system is also shown in the picture at right (red circles) as well as the parabola (yellow circle) and the sample (blue circle).

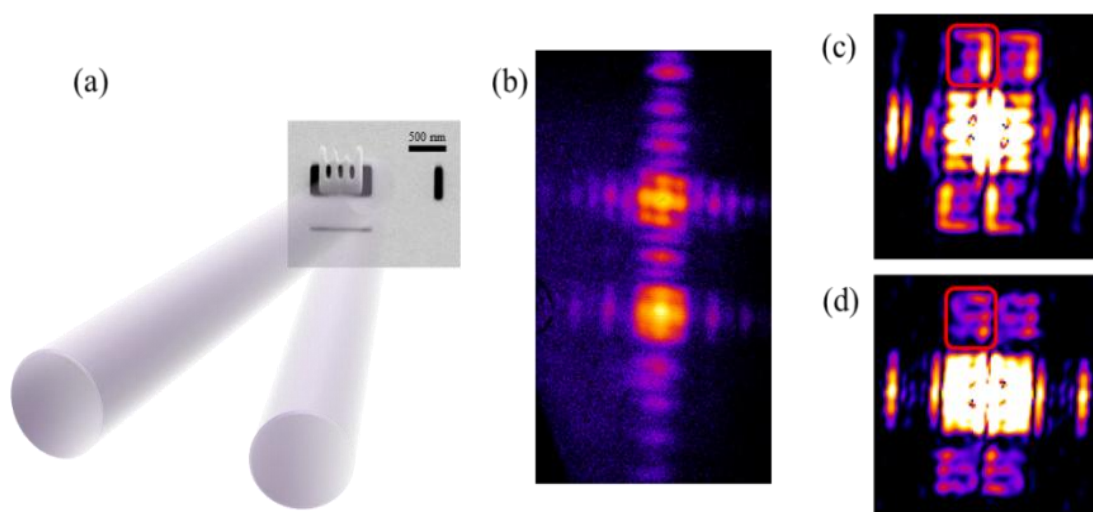


Figure 1.3 : Stereo-imaging. (a) MEB image of a test sample with two schematized incident XUV beams. The two black lines are HERALDO references. (b) First experimental diffraction pattern (September 2012). (c) and (d): Inversion of the

holograms taken at observation angles of 0° and 7° respectively. The red squares delimit one reconstruction.

Application in biology:

My thesis work has been based a strong expertise in higher harmonic generation (HHG) sources and in coherent soft X-ray imaging on test samples. However, no application in biology has been performed. I have started to collect and isolate nanoplanktons fished in the Indian Ocean (collaboration with Hannover University). We have already set a protocol to isolate these species on few nanometers thick carbon membranes which facilitates their transport into the vacuum chamber. Nanoplankton skeletons, similar to the ones in the figure below, will be studied.

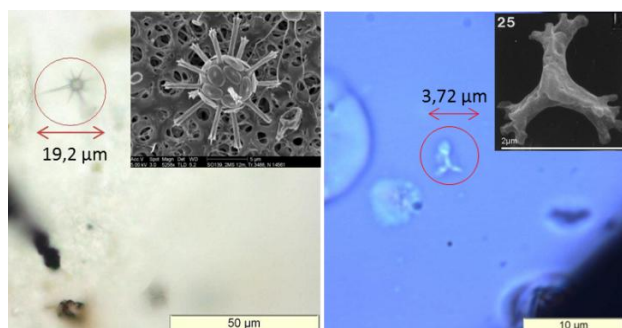


Fig. 5: Images of nanoplankton samples.

These biological species are of interest as their shape, structure and abundance monitor the climate change. The focal spot will be around few μm for these studies. The CEA HHG source can be tuned from 40 to 10 nm to increase the spatial resolution. We will collect data from nanoplanktons of few μm size. Our aim will be to collect 3D data sets at resolutions beyond conventional damage limits to get image of isolated nanoplanktons with 20 nm spatial resolution.

Application in ultrafast nanoscale phase transition:

An application in magnetism domain has then been studied as the first physical application realized on the harmonic beamline using coherent imaging techniques. I have been involved in this experiment. The results are reported on the two papers attached at the end of the manuscript. This has not been a central work for my Phd. Briefly, these articles report the magnetic scattering studies of the nanodomain structures on ferromagnetic (Co/Pd) multilayers. The HHG spectral studies with Ar and Ne gases was in purpose to adapt our harmonic beam to the cobalt absorption M-edge, followed by the HHG optimization of the selected 39th harmonic beam. A

comparison between HHG quality using filtered and non-filtered IR beam has been carried out in the meantime. The HHG optimization procedure and conclusions presented in Chapter II have been applied (except the wave front sensor) on these studies. Measurements of magnetic scattering from nanodomain structures have been realized over a large spectral bandwidth in both single-shot and multiple-shot acquisitions, from which magnetic properties of the nanodomain samples have been deduced. Spectral analysis showed an unexpected resonant peak, which corresponds to the palladium component of the sample instead of the cobalt. Scattering patterns are not made for real space reconstruction since the oversampling condition is not respected in the experiment, but promise the single-shot imaging of nanodomains structure, which may be performed in the parabola setup. It also paved the way for dynamic study of such magnetic samples in the under-construction pump probe experiment setup. The combination of dynamic and real space imaging in the near future will open the gate for understanding the spin-orbital and exchange interactions.

This magnetic application also resulted in the development of a versatile harmonic beamline, which is now a standardized, stable and powerful beamline providing harmonic beams of high coherent, photon flux and wave front quality, with tunable wavelength from 10 to 40 nm. Combining with the CDI, HERALDO and the under-developing 3D imaging techniques, our high flux harmonic beamline is suitable and ideal for a wide range of applications from physics to biology. We foresee a bright future for ultrafast dynamic studies with real space reconstructions of nanometric spatial resolution.

References

Introduction

1. J. W. Miao et al., “Extending the methodology of X-ray crystallography to allow imaging of micrometre-sized non-crystalline specimens”, *Nature* **400** 342-344 (1999).
2. H. Chapman *et al.*, “Femtosecond diffractive imaging with a soft-X-ray free-electron laser” *Nature Physics* **2** 839-843 (2006)
3. H. Chapman *et al.*, “High-resolution ab initio three-dimensional x-ray diffraction microscopy”, *J. Opt. Soc. Am. A* **23** 1179-1200 (2006)
4. A. Barty *et al.*, “Ultrafast single-shot diffraction imaging of nanoscale dynamics”, *Nature Photonics* **2** 415-419 (2008)
5. H. Jiang *et al.*, “Quantitative 3D imaging of whole, unstained cells by using X-ray diffraction microscopy”, *Proc. Natl. Acad. Sci. U.S.A.* **107** 11234-11239 (2010)
6. A.P. Mancuso *et al.*, “Coherent imaging of biological samples with femtosecond pulses at the free-electron laser FLASH”, *New J. Phys.* **12** 035003 (2010)
7. R.L. Sandberg *et al.*, “Lensless Diffractive Imaging Using Tabletop Coherent High-Harmonic Soft-X-Ray Beams”, *Phys. Rev. Lett.* **99** 098103 (2007)
8. A. Rivasio *et al.*, “Single-Shot Diffractive Imaging with a Table-Top Femtosecond Soft X-Ray Laser-Harmonics Source”, *Phys. Rev. Lett.* **103** 028104 (2009)
9. D. Sayre, “The squaring method: a new method for phase determination”, *Acta Cryst.* **5** 60-65 (1952)
10. J.R. Fienup, “Reconstruction of an object from the modulus of its Fourier transform”, *Optics Letters* **3** 27-29 (1978)
11. R.W. Gerchberg and W.O. Saxton, “A practical algorithm for the determination of phase from image and diffraction plane pictures”, *Optik* **35** 237-246 (1972)
12. H. Chapman and K. Nugent, “Coherent lensless X-ray imaging”, *Nature Photonics* **4** 833-839 (2012)
13. Seibert, M. M. *et al.*, *Nature* **470**, 78–81 (2011)
14. Chamard, V. *et al.*, *PhysRevLett* **104**, 165501 (2010)
15. Dierolf, M. *et al.*, *Nature* **467**, 436-439 (2010)

Chapter I

1. K. Burkhard, *et al.*, “Transmission and emission x-ray microscopy: operation modes, contrast mechanisms and applications”, *Journal of Physics: Condensed Matter* **23** 083002 (2011)
2. M.R. Howells, *et al.*, “An assessment of the resolution limitation due to radiation-damage in X-ray diffraction microscopy”, *Journal Of Electron Spectroscopy And Related Phenomena* **170** 4-12 (2009)
3. Q. Shen, *et al.*, “Diffractive imaging of nonperiodic materials with future coherent X-ray sources”, *Journal Of Synchrotron Radiation* **11** 432-438 (2004)
4. J.C.H. Spence, *et al.*, “Phase recovery and lensless imaging by iterative methods in optical, X-ray and electron diffraction”, *Phil. Trans. R. Soc. Lond. A* **360** 875 (2002)

5. I. McNulty, *et al.*, “High-Resolution Imaging by Fourier Transform X-ray Holography”, *Science***256** 1009-1012 (1992)
6. J.R.Fienup, “Phase retrieval algorithms: a comparison”, *Appl. Opt.***21** 2758 (1982)
7. J.R.Fienup, “Reconstruction of an object from the modulus of its Fourier transform”, *Opt. Lett.***3** (1) 27 (1978)
8. J.R.Fienup, “Reconstruction of a complex-valued object from the modulus of its Fourier transform using a support constraint”, *J. Opt. Soc. Am. A***4** (1) 118 (1987)
9. Y.M. Bruck and L.G. Sodin, “On the ambiguity of the image reconstruction problem”, *Opt. Commun.***30** 304–8 (1979)
10. R.H.T.Bates, “Fourier Phase Problems Are Uniquely Solvable In More Than One Dimension”, *Underlying Theory. Optik***61** (3) 247-262 (1982)
11. D. Gabor, “A New Microscopic Principle”, *Nature***161** (4098) 777-778 (1948)
12. J.W. Goodman, “Introduction to Fourier optics”, *Roberts & Co.* (2005)
13. M. Born and E. Wolf, “Principles of Optics: Electromagnetic Theory of Propagation, Interference and Diffraction of Light”, *Cambridge University Press* 7th edition (1999)
14. P. Thibault, “Algorithmic Methods In Diffraction Microscopy”, thesis work at *Faculty of the Graduate School, Cornell University* (2007)
15. M. Guizar-Sicairos, “Methods for Coherent Lensless Imaging and X-Ray Wavefront Measurement”, thesis work at *The Institute of Optics Arts, Sciences and Engineering, Edmund A. Hajim School of Engineering and Applied Sciences, University of Rochester, Rochester, New York* (2010)
16. D. Gauthier, “Imagerie nanométrique ultra-rapide par diffraction coh érente de rayonnement extr êne-UV produit par génération d’harmoniques d’ordre élevé”, thesiswork at *Universit é Paris Sud XI, Orsay, France*, (2012)
17. D. Attwood, “Soft X-Rays and Extreme Ultraviolet Radiation: Principles and Applications”, *Cambridge University Press* (2007)
18. P. P. Ewald, “Zur Theorie der Interferenzen der Röntgenstrahlen in Kristallen”, *Physikalische Zeitschrift***14** 465–472(1913)
19. D. Sayre, “Some implications of a theorem due to Shannon”, *Acta Crystallographica***5** 843 (1952)
20. J. Miao and D. Sayre, “On possible extensions of x-ray crystallography through diffraction-pattern oversampling”, *Acta Cryst. A***56** 596–506 (2000)
21. H. Nyquist, “Certain topics in telegraph transmission theory”, *Proceedings of the IEEE***90** (2) 280 (2002)
22. C.E. Shannon, “Communication in the Presence of Noise”, *Proceedings of the IRE***37** (1) 10 (1949)
23. E. Wolf, “Is a Complete Determination of the Energy Spectrum of Light Possible from Measurements of the Degree of Coherence?”, *Proceedings of the Physical Society***80**(6) 1269–1272 (1962)
24. A. Walther, “The Question of Phase Retrieval in Optics”, *Acta Optica***10** (1) 41–49 (1963)
25. R.W. Gerchberg and W.O. Saxton, “Practical Algorithm For Determination Of Phase From Image And Diffraction Plane Pictures”, *Optik***35** (2) 237 (1972)
26. V. Elser, “Phase retrieval by iterated projections”, *J. Opt. Soc. Am. A***20** (1) 40 (2003)
27. R. Luke, “Relaxed averaged alternating reflections for diffraction imaging”, *Inverse Problems***21** (1) 37–50 (2005)
28. S. Marchesini, “Benchmarking iterative projection algorithms for phase retrieval”, *arXiv:physics/0404091* (2004)

29. G.J. Williams, "Effectiveness of iterative algorithms in recovering phase in the presence of noise", *Acta Cryst. A* **63** 36-42(2007)
30. F.R.N.C. Maia, *et al.*, "Hawk: the image reconstruction package for coherent X-ray diffractive imaging", *Journal of Applied Crystallography* **43** (6) 1535-1539 (2010)
31. W.F. Schlotter, "Multiple reference Fourier transform holography with soft x rays", *Appl. Phys. Lett.* **89** (16) 163112 (2006)
32. H. He, *et al.*, "Use of extended and prepared reference objects in experimental Fourier transform x-ray holography", *Applied Physics Letters* **85** (13) 2454 (2004)
33. S.G. Podorov, *et al.*, "A non-iterative reconstruction method for direct and unambiguous coherent diffractive imaging", *Opt. Express* **15**(16) 9954 (2007)
34. M. Guizar-Sicairos and J.R. Fienup, "Holography with extended reference by autocorrelation linear differential operation", *Opt. Express* **15** (26) 17592 (2007)
35. S. Marchesini, *et al.*, "Massively parallel X-ray holography", *Nat. Photon.* **2** (9) 560 (2008)

Chapter II

1. A. McPherson, *et al.*, "Studies of multiphoton production of vacuum-ultraviolet radiation in the rare gases", *J. Opt. Soc. Am. B* **4** (4) 595 (1987)
2. M. Ferray, "Multiple-harmonic conversion of 1064nm radiation in rare gases", *J. Phys. B* **21** L31 (1988)
3. T. Brabec and F. Krausz, "Intense few-cycle laser fields: Frontiers of nonlinear optics", *Rev. Mod. Phys.* **72** 545 (2000)
4. J.L. Krause, *et al.*, "High-order harmonic generation from atoms and ions in the high intensity regime", *Physical Review Letters* **68** (24) 3535 (1992)
5. P.B. Corkum, "Plasma perspective on strong field multiphoton ionization", *Phys. Rev. Lett.* **71** 1994 (1993)
6. K.J. Schafer, *et al.*, "Above threshold ionization beyond the high harmonic cutoff", *Phys. Rev. Lett.* **70** 1599-1602 (1993)
7. M. Lewenstein, *et al.*, "Theory of high-harmonic generation by low-frequency laser fields", *Physical Review A* **49** (3) 2117 (1994)
8. P.M. Paul, *et al.*, "Observation of a train of attosecond pulses from high harmonic generation", *Science* **292** 1689-1692 (2001)
9. G. Lambert, *et al.*, "Injection of harmonics generated in gas in a free-electron laser providing intense and coherent extreme-ultraviolet light", *Nature Physics* **4** 296-300 (2008)
10. J. Gautier, *et al.*, "Optimization of the wave front of high order harmonics", *Eur. Phys. J. D* **48** 459-463 (2008)
11. C. Valentin, *et al.*, "High-order harmonic wave fronts generated with controlled astigmatic infrared laser", *J. Opt. Soc. Am. B* **25** (7) B161 (2008)
12. S. Kazamias, *et al.*, "High order harmonic generation optimization with an apertured laser beam", *The European Physical Journal* **21** (3) 353 (2002)

13. W. Boutu, *et al.*, “High-order-harmonic generation in gas with a flat-top laser beam”, *Physical Review A* **84** (6) 063406 (2011)
14. M. Nisoli, *et al.*, “High-Brightness High-Order Harmonic Generation by Truncated Bessel Beams in the sub-10-fs Regime”, *Phys. Rev. Lett.* **88** 033902 (2002)
15. P. Villoresi, *et al.*, “Optimization of high-order harmonic generation by adaptive control of a sub-10-fs pulse wave front”, *Opt. Lett.* **29** 207 (2004)
16. M. Nisoli, *et al.*, “Generation of high energy 10 fs pulses by a new pulse compression technique”, *Appl. Phys. Lett.* **68** 2793 (1996)
17. E. Marcatili and R. Schmeltzer, “Hollow metallic and dielectric waveguides for long distance optical transmission and lasers”, *Bell Syst. Tech. J.* **43** 1783–1809 (1964)
18. E. Snitzer, “Cylindrical Dielectric Waveguide Modes”, *J. Opt. Soc. Am.* **51** 491–498 (1961)
19. C. Iaconis and I.A. Walmsley, “Spectral Phase Interferometry for Direct Electric-Field Reconstruction of Ultrashort Optical Pulses”, *Opt. Lett.* **23** 792–794 (1998)

Chapter III

1. “Introduction: Focused ion beam systems” <http://www.fibics.com/fib/tutorials/introduction-focused-ion-beam-systems/4/>
2. M. Born and E. Wolf, “Principles of Optics: Electromagnetic Theory of Propagation, Interference and Diffraction of Light”, *Cambridge University Press* 7th edition (1999)
3. D. Shapiro, *et al.*, “Biological imaging by soft x-ray diffraction microscopy”, *Proc. Natl. Acad. Sci. U.S.A.* **102** (43) 15343–15346 (2005)
4. A. Ravasio, *et al.*, “Single-Shot Diffractive Imaging with a Table-Top Femtosecond Soft X-Ray Laser-Harmonics Source”, *Phys. Rev. Lett.* **103** 028104 (2009)
5. S. Marchesini, *et al.*, “Coherent X-ray diffractive imaging: applications and limitations”, *Opt. Express* **11** (19) 2344 (2003)
6. M.R. Howells, *et al.*, “An assessment of the resolution limitation due to radiation-damage in X-ray diffraction microscopy”, *Journal Of Electron Spectroscopy And Related Phenomena* **170** (1-3) 4–12 (2009)
7. “Signal-to-noise ratio” [Http://www.princetoninstruments.com/cms/index.php/ccd-primer/172-signal-to-noise-ratio](http://www.princetoninstruments.com/cms/index.php/ccd-primer/172-signal-to-noise-ratio)
8. M. Guizar-Sicairos, “Methods for Coherent Lensless Imaging and X-Ray Wavefront Measurement”, thesis work at *The Institute of Optics Arts, Sciences and Engineering, Edmund A. Hajim School of Engineering and Applied Sciences, University of Rochester, Rochester, New York* (2010)

Chapter IV

1. H. Chapman, A. Barty, S. Marchesini *et al.* 2006. “High-resolution ab initio three-dimensional x-ray diffraction microscopy”, *J. Opt. Soc. Am. A* **23** (5) 1179
2. J. Miao, T. Ishikawa, B. Johnson *et al.* 2002. “High Resolution 3D X-Ray Diffraction Microscopy”, *Phy. Rev. Lett.* **89** (8) 088303

3. K.Raines, S.Salha, R.Sandberg et al. 2010. "Three-dimensional structure determination from a single view", *Nature* **463** (7278) 214-7
4. R. W. James, *The Optical Principles of the Diffraction of X-Rays* (Bell, 1962)
5. E. Wolf, "Three-dimensional structure determination of semi-transparent objects from holographic data," *Opt. Commun.* **1**, 153–156 (1969).
6. J.Miao, D. Sayre, H.N.Chapman et al. 1998. "Phase retrieval from the magnitude of the Fourier transforms of nonperiodic objects", *J. Opt. Soc. Am. A* **15** (6) 1662
7. J.Miao, K. Hodgson, D. Sayre. 2001. "An approach to three-dimensional structures of biomolecules by using single-molecule diffraction images", *P.N.A.S.* **98**(12)
8. I.Robinson, J.Miao. 2004. "Three-Dimensional Coherent X-Ray Diffraction Microscopy", *March*, 177-181
9. D.Shapiro, P.Thibault, T.Beetz et al. 2005. "Biological imaging by soft x-ray diffraction microscopy." *P.N.A.S.* **102** (43) 15343-6
10. Chen, C.-C., Jiang, H., Rong, L., Salha, S., Xu, R., Mason, T.G. and Miao, J. Threedimensional imaging of a phase object from a single sample orientation using an optical laser. *Phys. Rev. B*, **84**, 224104 (2011)..
11. M.Seaberg, D.Adams, E.Townsend et al. 2011. "Ultrahigh 22 nm resolution coherent diffractive imaging using a desktop 13 nm high harmonic source", *Opt. Exp.* **19**(23) 22470-9
12. J.Miao, R. Sandberg, C.Song. 2011. "Coherent X-ray Diffraction Imaging", *IEEE selected topics in quantum electronics*, page (1-12)
13. C.Chen, H.Jiang, L.Rong et al. 2011. "Three-dimensional imaging of a phase object from a single sample orientation using an optical laser", *Phy.Rev.B* **84** (22) 224104
14. J.Miao, C.Chen, Y.Mao et al. "Potential and Challenge of Ankylography"
15. Wei, H. 2011. Fundamental limits of "Ankylography" due to dimensional deficiency. *Nature* 480, E1 doi:10.1038/nature10634
16. Wang, G, Yu, H. & Cong, W. 2011. Non-uniqueness and instability of 'ankylography'. *Nature* 480, E2–E3 doi:10.1038/nature10635.

Chapter V

1. H. Andruleit, *et al.*, "Stereo-microscopy of coccolithophores - modern applications for imaging and morphological analysis", *J. Nanoplankton Res.* **28**(1) 1-16 (2006)
2. M. Geisen, *et al.*, "Three- dimensional imaging of coccoliths and coccospheres." Abstract for poster presented at the 8th Conference of the International Nanoplankton Association, 11th-15th September, 2000, Bremen, Germany, *Journal of Nanoplankton Research*, 22: 100. (2000)

Articles List

Article I

“Spatial quality improvement of a Ti:Sapphire laser beam by Modal Filtering”

Benoit Mahieu, David Gauthier, Michel Perdrix, Xunyou Ge, Willem Boutu, Fabien Lepetit, Fan Wang, Bertrand Carré, Thierry Auguste, Hamed Merdji, David Garzella, and Olivier Gobert

Abstract. We present a study on the improvement of the spatial quality of a laser beam, called modal filtering. The method is theoretically compared to the classical pinhole filtering technique in the case of an astigmatic Gaussian beam, illustrating, in this particular case, its efficiency for filtering low spatial frequencies. Experimental study of the modal filtering of a high energy, temporally-chirped beam from a Ti:Sapphire chirped-pulse-amplification system is presented. Beam profile, wavefront and pulse duration after compression were measured, showing a dramatic improvement of beam quality and no modifications of the temporal distribution. High-order harmonic generation in a rare gas, a highly nonlinear process which is phase matching dependent, was used to test the effect of the filter and showed a clear enhancement of the generation.

Applied Physics B: Lasers and Optics, **118**:47-60 (2015).

Article II

“Impact of wave front and coherence optimization in coherent diffractive imaging”

X. Ge, W. Boutu, D. Gauthier, F. Wang, A. Borta, B. Barbreil, M. Ducouso, A. Gonzalez, B. Carré, D. Guillaumet, M. Perdrix, O. Gobert, J. Gautier, G. Lambert, F. Maia, J. Hajdu, P. Zeitoun and H. Merdji, *Opt. Express* **21**, 11441–11447 (2013).

Article III

“Impact of the signal-to-noise ratio and noise processing in holographic and coherent diffractive imaging”

F. Wang, A.I. Gonzalez, I. Bianca, X. Ge, D. Gauthier, W. Boutu, M. Ducouso, M. GuizarSicairos, M. Kovacev and H. Merdji

Abstract. Signal-to-noise ratio is a key factor in lens-less imaging, particularly for low signal detection experiments. We present our recent study of the noise impact on

holography with extended reference and Fourier Transform Holography and coherent diffractive imaging. Experimental data have been measured either in single or multi-shot acquisition using an intense coherent soft X-ray high harmonic source. Hardware and software noise processing during and after the diffraction figure detection are discussed. The comparison of experimental results of the three imaging techniques concludes the advantages and inconvenient of each configuration.

Article in preparation, the core of the article is presented in Chapter III (holographic techniques section) of the thesis.

Article IV

“Single-shot studies of a Co/Pd thin film’s magnetic nano-domain structure using ultrafast x-ray scattering”

M Ducouso, X Ge, W Boutu, D Gauthier, B Barbrel, F Wang, A Borta, A-I Gonzalez, M Billon, B Vodungbo, J Gautier, R Hawaldar, B Tudu, R Delaunay, M Tortarolo, P Zeitoun, J Lüning and H Merdji

Laser Physics **24**,025301 (2014).

Article V

“Sub-100 nanometer lensless probing of Co/Pd magnetic nanodomains using a table-top femtosecond soft X-ray harmonic source”,

X. Ge, M. Ducouso, W. Boutu, B. Tudu, B. Barbrel, D. Gauthier, A. Borta, A. Gonzalez, F. Wang, B. Iwan, M. Billon, M. Perdrix, D. Guillaumet, F. Lepetit, B. Vodungbo, J. Gautier, R. Hawaldar, M. Tortarolo, R. Delaunay, P. Zeitoun, J. Lüning and H. Merdji,

Journal of Modern Optics **10**, 09500340 (2013).